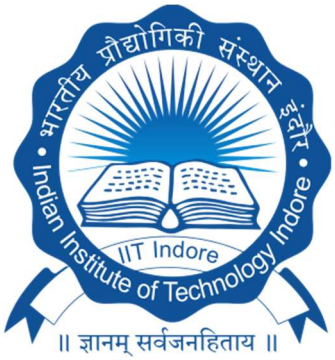
DEVELOPMENT OF VACUUM AND MAGNETICALLY ASSISTED μ-PLASMA POWDER ADDITIVE MANUFACTURING (VMA-μ-PPAM) PROCESS FOR BIOMEDICAL MATERIALS

M.Tech. Thesis

By
RAVI RANJAN



DEPARTMENT OF MECHANICAL ENGINERRING
INDIAN INSTITUTE OF TECHNOLOGY INDORE
MAY 2026

DEVELOPMENT OF VACUUM AND MAGNETICALLY ASSISTED μ-PLASMA POWDER ADDITIVE MANUFACTURING (VMA-μ-PPAM) PROCESS FOR BIOMEDICAL MATERIALS

A THESIS

Submitted in partial fulfillment of the
requirements for the award of the degree
of
Master of Technology

by

RAVI RANJAN



DEPARTMENT OF MECHANICAL ENGINERRING
INDIAN INSTITUTE OF TECHNOLOGY INDORE
MAY 2026

INDIAN INSTITUTE OF TECHNOLOGY INDORE

CANDIDATE'S DECLARATION

I hereby certify that the work which is being presented in the thesis entitled **DEVELOPMENT OF VACUUM AND MAGNETICALLY ASSISTED μ-PLASMA POWDER ADDITIVE MANUFAFACTURING (VMA-μ-PPAM) PROCESS FOR BIOMEDICAL MATERIALS** in the partial fulfillment of the requirements for the award of the degree of **MASTER OF TECHNOLOGY** and submitted in the **DEPARTMENT OF MECHANICAL ENGINEERING, Indian Institute of Technology Indore**, is an authentic record of my own work carried out during the time period from July 2024 to July 2026 under the supervision of Prof. Neelesh Kumar Jain, Professor, Dept. of Mechanical Engineering, IIT Indore and Dr. Mayur S. Sawant, Assistant Professor, MIT University, Pune.

The matter presented in this thesis has not been submitted by me for the award of any other degree of this or any other institute.

Ravi Ranjan
26/05/26

Signature of the student with date
(RAVI RANJAN)

This is to certify that the above statement made by the candidate is correct to the best of our knowledge.

26th May 2026

Signature of the Supervisor of M.Tech. thesis #1 (with date)

(PROF. NEELESH KUMAR JAIN)

Signature of the Supervisor of M.Tech. thesis #2 (with date)

(DR. MAYUR S. SAWANT)

MR. RAVI RANJAN has successfully given his M.Tech. Oral Examination held on **26 May 2026**.

Signature(s) of Supervisor(s) of M.Tech. thesis
Date: 26th May 2026

Convener, DPGC
Date: 28-05-2026

ACKNOWLEDGEMENTS

I would like to express my sincere gratitude to my M.Tech supervisor **Prof. Neelesh Kumar Jain** for his constant guidance, encouragement, and invaluable support throughout my research work. His motivation, insightful suggestions, and immense knowledge in the field of advanced manufacturing and additive manufacturing have greatly helped me in completing this work successfully.

I would also like to extend my heartfelt thanks to my co-supervisor **Dr. Mayur S. Sawant** for his continuous support, technical guidance, and encouragement during my research journey. His valuable suggestions and cooperative nature helped me overcome many challenges during this work.

I would especially like to express my deep gratitude to PhD scholar **Mr. Balbir Singh Negi** for his continuous guidance, motivation, and support throughout my research work. His technical expertise, valuable discussions, and willingness to help at every stage of the project greatly contributed to the successful completion of this work. I am truly thankful for his patience, encouragement, and constant assistance during experimentation, analysis, and preparation of this work.

I am thankful to **the Sophisticated Instrumentation Center (SIC), Advanced Manufacturing Processes (AMP) Lab,** and **Central Workshop** for providing the required facilities and support to carry out my experimental work successfully.

I would also like to sincerely thank the lab staff members **Mr. Deepak Rathore, Mr. Santosh Sharma,** and **Mr. Vinay Mishra** for their valuable cooperation, technical assistance, and support during the fabrication and experimental work.

I would also like to express my heartfelt gratitude to my friends **Mr. Rohit Garg, Mr. Nirmalya Dana, Mr. Prateek Tumrali, Ms. Sangeetha A**. and **Mr. Vivekanand P**. for their constant support, encouragement, help, and memorable companionship throughout my research work. Their motivation and valuable discussions greatly helped me during difficult phases of the research journey.

Finally, I express my sincere gratitude to everyone who directly or indirectly contributed to the successful completion of this work.

DEDICATION

I dedicate this M.Tech. thesis to my beloved mother and father, whose unconditional love, sacrifices, and endless support have been the greatest strength in my life. From them, I learned kindness, honesty, hard work, and the courage to never give up. Their blessings, encouragement, and faith in me have guided me through every challenge and made this achievement possible.

This thesis is a small token of gratitude and respect for my parents for everything they have done for me and for being my greatest source of inspiration throughout my life.

Abstract

Vacuum- and magnetic field-assisted additive manufacturing technologies have recently gained significant attention for the fabrication of high-performance metallic components due to their ability to improve melt pool stability, reduce porosity, refine microstructure, and enhance mechanical properties. In the present work, a vacuum- and magnetic field-assisted micro-plasma powder additive manufacturing (μ-PPAM) system was developing by integrating a specially designed vacuum chamber, electromagnet setup, vacuum pump, suction filtration unit, and vaccum measuring devices. The vacuum environment was utilized to minimize oxidation, atmospheric contamination, and porosity during deposition, while the externally applied magnetic field was employed to improve molten pool convection, powder flow behavior, and microstructural refinement during fabrication. The magnetic flux density generated by the electromagnet was characterized under different applied voltages using a calibrated gaussmeter, and a nearly linear increase in magnetic flux density was observed with increasing voltage.

Titanium-based biomaterials are widely used in orthopaedic and dental implant applications because of their excellent biocompatibility, high specific strength, and superior corrosion resistance. However, conventional implant materials such as stainless steel, Co–Cr alloys, commercially pure titanium (CP-Ti), and Ti–6Al–4V possess several limitations including stress shielding effect, release of toxic ions, poor antibacterial behavior, allergic reactions, and implant-associated infections. Furthermore, the higher elastic modulus of conventional titanium alloys compared to human cortical bone often leads to improper load transfer and implant failure. Therefore, the development of advanced β-titanium alloys containing non-toxic alloying elements with superior mechanical and biological performance is essential for next-generation biomedical implants.

To overcome these limitations, Ti–9Mo–7Nb–xCu (x = 2, 4, and 6 wt.%) β-titanium alloys were developed using μ-PPAM process. Mo and Nb were selected as β-phase stabilizing elements to reduce elastic modulus and improve corrosion resistance and biocompatibility, while Cu was incorporated to provide antibacterial functionality and enhanced mechanical performance. The developed alloys were systematically investigated for density, porosity, microstructure, phase evolution, microhardness, tensile and compressive properties, abrasion resistance, fracture toughness, cell viability, cell adhesion, and antibacterial behavior.

Experimental results revealed that increasing Cu content significantly reduced porosity, and the Ti–9Mo–7Nb–6Cu alloy exhibited the lowest porosity among all the developed alloys. Microstructural and X-ray diffraction (XRD) analyses confirmed the formation of α-Ti, β-Ti, TiO_2, and Ti_2Cu intermetallic phases in all fabricated alloys. The addition of Cu refined the microstructure and improved densification, resulting in enhanced hardness and strength. The Ti–9Mo–7Nb–6Cu alloy exhibited the highest microhardness, yield strength, ultimate tensile strength, compressive strength, abrasion resistance, and fracture toughness compared to Ti–9Mo–7Nb–2Cu and Ti–9Mo–7Nb–4Cu alloys. Fractography analysis revealed mixed ductile–brittle fracture characteristics containing dimples, cleavage facets, and tear ridges. In-vitro biological investigations demonstrated improved cell viability and cell adhesion with increasing Cu content, which were further confirmed using scanning electron microscopy (SEM). Moreover, the Ti–9Mo–7Nb–6Cu alloy exhibited the highest antibacterial efficiency, indicating its strong potential for reducing implant-associated infections.

Therefore, the developed Ti–9Mo–7Nb–6Cu alloy fabricated through μ-PPAM can be considered a promising next-generation biomedical implant material with enhanced mechanical properties, superior antibacterial behavior, improved biocompatibility, and excellent potential for long-term orthopaedic and dental implant applications.

Keywords

Vacuum-assisted additive manufacturing; Magnetic field-assisted additive manufacturing; μ-PPAM; β-titanium alloys; Biomedical implants; Microstructure; Porosity; Mechanical properties; Fractography; Abrasion resistance; Fracture toughness; Cell viability; Cell adhesion; Antibacterial behavior.

LIST OF PUBLICATIONS

Journal Publications

I. Balbir Singh Negi, **Ravi Ranjan**, Neelesh Kumar Jain, "**Effect of nozzle tilt angle on microstructure and mechanical properties of SS316L multilayer depositions by µ-PMBAM process**." (Submitted to **Progress in Additive Manufacturing** on **15th May 2026, Impact factor: 5.4**).

II. **Ravi Ranjan**, Balbir Singh Negi, Priyanka Payal, Neelesh Kumar Jain, Mayur Sawant, "**Study of biocompatibility, bacterial inhibition, microstructure and mechanical properties of Ti-9M0-7Nb-xCu alloys" (**ready for submission to **Additive Manufacturing, Impact factor: 11.1)**

III. **Ravi Ranjan,** Balbir Singh Negi**,** Neelesh Kumar Jain, Mayur S. Sawant, "**Investigations on Wear and corrosion behavior of Ti-9M0-7Nb-xCu alloys**" (to be submitted **Wear, Impact factor: 6.1**)

Conference Paper

I. **Ravi Ranjan**, Balbir Singh Negi, Neelesh Kumar Jain. "Investigation of Nozzle Angle Influence on SS316L Powder Distribution by Micro Plasma Arc-Based Metal Additive Manufacturing Process" 10th International and 31st All India Manufacturing Technology, Design & Research Conference (**AIMTDR 2025**).

TABLE OF CONTENTS

LIST OF FIGURES…….. xiii

LIST OF TABLES……..... xvii

NOMENCLATURE……. xix

ACRONYMS……..... xxi

Chapter 1: Introduction……..... 1

1.1 Introduction to Additive Manufacturing……..... 1

1.2 Classification of Additive Manufacturing Processes..... 2

1.2.1 Classification According to ASTM F-42 Standard…….. 2

1.2.2 Classification Based on Melting Requirement……. 3

1.3 Fusion-Based Additive Manufacturing Processes…..... 4

1.3.1 Beam-Based AM Processes…….. 4

1.3.2 Arc-Based AM Processes……. 5

1.4 Advantages of Additive Manufacturing Processes……..... 6

1.5 Limitations of Additive Manufacturing Processes……..... 7

1.6 Introduction to Titanium Alloys……..... 7

1.6.1 Classification of Titanium Alloys……. 9

1.6.2 Phase Stabilizing Elements for Titanium Alloys…….. 10

1.6.3 Need for Enhancing Properties of Titanium Alloys…….. 12

1.7 Design Using CALPHAD Modelling…….. 13

1.8 Applications of Properties-Enhanced Titanium Alloys……. 14

1.9 Organization of the Thesis……..... 16

Chapter 2: Review of Past Work and Research Objectives…….. 17

2.1 Recent Advances in Vacuum-Assisted Metal Additive Manufacturing……. 17

2.2 Influence of Magnetic Fields on Melt Pool Behaviour and Microstructure in Metal Additive Manufacturing……..... 20

2.3 Advancements in Titanium Alloys for Orthopedic Implants with Antibacterial Properties …… 26

2.4 Summary of the Literature Review……. 30

2.5 Identified Research Gaps……..... 32

2.6 Research Objectives (RO)…… 33
2.7 Research Methodology workflow ……..... 34
Chapter 3: Details of The Experiment……. 35
3.1 Development of Vacuum and Magnetically Assisted μ-PPAM System …… 35
3.1.1 Key Components of Vacuum and Magnetically Assisted μ-PPAM …... 35
3.1.2 Development of Vacuum Chamber…….. 36
3.1.3 Electromagnet Setup and Magnetic Flux Density–Voltage Characterization …… 37
3.2 Design of Alloy …….. 39
3.3 Powder preparation……..... 41
3.4 Apparatus for μ-PPAM Process……..... 50
3.5 Study of single-layer depositions……..... 53
3.6 Characterization of multi-layer depositions……. 54
3.7 Density and porosity evaluation……..... 55
3.8 Study of microstructure and phase evolution ……. 55
3.9 Microhardness Evaluation……... 56
3.10 Tensile test and its fractography …… 56
3.11 Compressive Test……... 58
3.12 Fracture toughness and abrasion resistance……..... 58
3.13 Metallic ions release analysis……..... 59
3.14 Cell viability analysis ……..... 60
3.15 Cell adhesion assessment…….. 61
3.16 Bacterial inhibitory test……. 61
Chapter 4: Results and Analysis for Ti-9Mo-7Nb-xCu…… 63
4.1 Results and analysis of single-layer depositions……. 63
4.2 Results and analysis of multi-layer depositions…….. 67
4.3 Porosity and density results……..... 67
4.4 Analysis of evolution of phases ……..... 68
4.5 Microstructure analysis…… 69
4.6 Microhardness results……..... 72
4.7 Results of tensile test and its fractography ……. 74

4.8 Compressive test results…….. 77
4.9 Fracture toughness and abrasion resistance results……. 78
4.10 Results of metallic ion release…… 83
4.11 Results of cell viability and cell adhesion……..... 87
4.12 Cell adhesion and its morphology analysis…… 89
4.13 Results of bacterial inhibitory test……..... 91
Chapter 5: Conclusion…….. 93
Chapter 6: REFERENCES…….. 95

LIST OF FIGURES

Caption of The Figure	Page No.
Fig 1.1: Key developments in additive manufacturing since 1970s ……...	1
Fig 1.2: Classification of metal additive manufacturing processes according to melting requirement of the feedstock material ……	3
Fig 1.3: Strength-to-weight ratio and fracture toughness for various metals and alloys ……	8
Fig 1.4: Classification of Ti alloys based on phases present at room temperature	9
Fig 1.5: Some biomedical applications of Ti alloys with enhanced properties ……..	15
Fig 2.1: Schematic diagram of MFA-PAAM; (b) MFA_PAAM system; (c) Angle of placement for high-speed camera shooting; (d) Sketch map of the arch pressure measuring device …….	20
Fig 2.2: Schematic diagram of magnetic field, showing: (a) the effect of steady magnetic field on arc during WAAM in yz plane and (b) in xy plane (Red dots are the charged particles and black dots are the magnetic lines) (For interpretation of the references to colour in this figure legend, the reader is referred to the web version of this article) …….	21
Fig 2.3: Schematic representation of WAAM deposition process …….	22
Fig 2.4: (a) (i)Schematic showing the solidification process of L-DED under a 0.55 T transverse SMF, where the thermoelectric current, thermoelectric magnetic force are illustrated in the solidification front and also, distribution of magnetic field intensity. (ii) OM images; and β grains microscopy images; and Histograms of β grain size . (b) Schematic representation of WAAM deposition process and picture of deposited sample. Also, microhardness along the midline of the deposited Inconel 625 alloy without and with magnetic field . (c) MAF processing principles and equipment setup showing two different tool path setups. (d) The schematic diagram of WAAM process with EMF. Also, the macro-morphology of fabricated thin-wall parts with 60 layers: with EMF of 2 A 70 Hz and without EMF ……	24
Fig 2.5: Process Bone Formation and Resorption ……...	27

Fig 2.6: Elastic modulus values of orthopedic alloys ……. 27
Fig 2.7: Schematic representation for biofilm formation on titanium biomaterial 28
Figure 2.8: (**A**) The process of biofilm formation (**B**) Conventional therapy and novel prevention or treatment strategies ……. 29
Fig 2.9: Schematic representation for the steps of biofilm formation on titanium biomaterial. The schematic drawing depicts the five main steps for forming and spreading biofilms such as protein adsorption, microbial adhesion, biofilm formation, maturation, and dispersal. The clinical disease progression is dependent on biofilm accumulation …….. 30
Figure 2.10: Workflow of research methodology……... 34
Fig 3.1: Key Components of Vacuum and Magnetically Assisted μ-PPAM ……. 36
Fig 3.2: Development of the Vacuum chamber…….. 37
Fig 3.3: Electromagnet Setup……... 38
Fig 3.4: Magnetic Flux Density–Voltage…… 38
Fig 3.5a: Thermo-calc simulated phase diagram for deciding upper limit of Cu addition to Ti-9Mo-7Nb-xCu alloy…….. 40
Fig 3.5b: Scheil solidification diagram of Ti-9Mo-7Nb-xCu alloy …….. 41
Fig 3.6: Morphology of as-received powders of Ti, Nb, Mo, and Cu …… 43
Fig 3.7: Morphology, chemical composition, average size of powder particles, and elemental mapping for the prepared powder of Ti-9Mo-7Nb-2Cu alloy …… 45
Fig 3.8: Morphology, chemical composition, average size of powder particles, and elemental mapping for the prepared powder of Ti-9Mo-7Nb-4Cu alloy …… 47
Fig 3.9: Morphology, chemical composition, average size of powder particles, and elemental mapping for the prepared powder of Ti-9Mo-7Nb-6Cu alloy …… 49
Fig 3.10: (A) Represents the working principle of the μ-PPAM process, while (B) shows different deposition tracks possible using the μ-PPAM technique …….. 50
Fig 3.11: Photograph of the developed 5-axis CNC μ-PPAM machine ……. 51
Fig 3.12: Optical microscopic images of the cross-sectional area of a single layer of Ti-9Mo-7Nb-4Cu alloy …… 53
Fig 3.13: Location of cutting different samples from the multi-layer depositions of Ti-9Mo-7Nb-xCu for evaluation of different tests ……..… 54

Fig 3.14: Tensile test samples of Ti-9Mo-7Nb-xCu alloy dimensions as per standard ASTM E8M ……... 57

Fig 4.1: Quality of single-layer depositions of Ti-9Mo-7Nb-4Cu alloy: (a) non-uniform and discontinuous deposition (NCD), and (b) uniform and continuous deposition (UCD) …… 64

Fig 4.2: Variation in width, height, and efficiency of deposition, diluted depth, and dilution % of single-layer depositions of Ti-9Mo-7Nb-4Cu alloy: (a) µ-plasma Power (W), (b) Travel speed of deposition head (mm/min), and (c) Feedstock Powder Flow Rate (g/min) …….. 65

Fig. 4.3 (a) Comparison of experimental density and theoretical density, and (b) average porosity % of Ti-9Mo-7Nb-2Cu, Ti-9Mo-7Nb-4Cu, and Ti-9Mo-7Nb-6Cu alloys …… 67

Fig 4.4: Evolution of phases in multilayer depositions of Ti-9Mo-7Nb-2Cu, Ti-9Mo-7Nb-4Cu, and Ti-9Mo-7Nb-6Cu alloys ……. 69

Fig 4.5: Represent SEM morphology images, chemical composition, area live mapping, and elemental mapping of µ-PPAM developed multilayer deposition of (**a)** Ti-9Mo-7Nb-2Cu, **(b)** Ti-9Mo-7Nb-4Cu, and **(c)** Ti-9Mo-7Nb-6Cu alloy…… 71

Fig 4.6: Microhardness of the developed Ti-9Mo-7Nb-2Cu alloy, Ti-9Mo-7Nb-4Cu, and Ti-9Mo-7Nb-6Cu: (a) microhardness profile along the build direction, and (b) average values of microhardness…… 73

Fig 4.7: Engineering stress and engineering strain graphs for µ-PPAM developed Ti-9Mo-7Nb-2Cu alloy, Ti-9Mo-7Nb-4Cu, and Ti-9Mo-7Nb-6Cu …… 74

Fig 4.8: SEM images showing the fractography of tensile samples of the developed: (a)Ti-9Mo-7Nb-2Cu alloy, (b) Ti-9Mo-7Nb-4Cu, and (c) Ti-9Mo-7Nb-6Cu alloy……..... 75

Fig 4.9: Compressive stress–strain curve for µ-PPAM developed Ti-9Mo-7Nb-2Cu alloy, Ti-9Mo-7Nb-4Cu, and Ti-9Mo-7Nb-6Cu alloys ……... 77

Fig 4.10: Scratch COF variation along the scratch track length at different 5N and 10N applied loads for: (a)Ti-9Mo-7Nb-2Cu alloy, (b) for Ti-9Mo-7Nb-4Cu alloy, and (c) for Ti-9Mo-7Nb-6Cu alloy …….. 80

Fig 4.11: Optical microscopic images of the track length at 5N and 10N applied load: (a) for Ti-9Mo-7Nb-2Cu alloy, (b) for Ti-9Mo-7Nb-4Cu alloy, and (c) for Ti-9Mo-7Nb-6Cu alloy……. 81
Fig 4.12: Effect of applied load for Ti-9Mo-7Nb-2Cu alloy, Ti-9Mo-7Nb-4Cu alloy, and Ti-9Mo-7Nb-6Cu alloys on their: (a) average COF, (b) scratch volume, (c) fracture toughness and (d) scratch hardness …… 81
Fig 4.13: Released amounts of metallic ions of constituent elements (a) Ti, (b) Mo, (c) Nb, and (d) Cu at pH 5.4 and 7.4 in SBF and PBS solution for immersion durations of 1, 2, and 3 weeks ……. 85
Fig 4.14: Viability of L929 fibroblast cells at different incubation durations of 2,4, and 6 days in the developed Ti-9Mo-7Nb-2Cu, Ti-9Mo-7Nb-4Cu, and Ti-9Mo-7Nb-6Cu alloys ……..... 88
Fig 4.15: Fluorescence microscopic images depicting cell adhesion to the samples of Ti-9Mo-7Nb-2Cu, Ti-9Mo-7Nb-4Cu, and Ti-9Mo-7Nb-6Cu and the control using Calcein AM dye for the live cells (shown green colour) and Propidium Iodide dye for dead cells (shown red colour) ……. 89
Fig 4.16: SEM images showing adhesion and morphology of L929 fibroblast cells on Ti-9Mo-7Nb-2Cu, Ti-9Mo-7Nb-4Cu, and Ti-9Mo-7Nb-6Cu and the control surfaces at different magnifications ……..… 90
Fig 4.17: Morphologies of E. coli bacteria correspond to Ti-9Mo-7Nb-2Cu, Ti-9Mo-7Nb-4Cu, and Ti-9Mo-7Nb-6Cu alloys ……..…. 91
Fig 4.18: Bar graph representing the antibacterial rate against E. coli of the developed Ti–9Mo–7Nb–2Cu, Ti–9Mo–7Nb–4Cu, and Ti–9Mo–7Nb–6Cu alloys ... 91

LIST OF TABLES

Caption of the Table	Page No.
Table 1.1: Classification of AM processes according to the ASTM F-42 standard…	2
Table 1.2: Summary of phase stabilizing elements for Ti alloys and their effects .;..	11
Table 1.3: Summary of typical applications of Ti alloys and their required properties …….....	12
Table 2.1: Effect of Magnetic Field-Assisted and Additive Manufacturing Techniques on Microstructure and Mechanical Properties of Metallic Alloys..…..…	25
Table 3.1: Chemical compositions of the designed Ti-Mo-Nb-xCu alloys by wt.%	43
Table 3.2: Value of μ-PPAM process parameters, and design of experiments approach used in different phases of experiments….....	52
Table 4.1: Measured and computed responses of the Ti-9Mo-7Nb-4Cu alloy for various combinations of input parameters in the μ-PPAM process ……	63
Table 4.2: Experimental density, theoretical density, relative density, and porosity values of Ti-9Mo-7Nb-2Cu, Ti-9Mo-7Nb-4Cu, and Ti-9Mo-7Nb-6Cu alloys ……..	68
Table 4.3: Tensile yield strength, Ultimate tensile strength (UTS) and % elongation for Ti-9Mo-7Nb-2Cu alloy, Ti-9Mo-7Nb-4Cu, and Ti-9Mo-7Nb-6Cu alloys obtained from their tensile tests……	75
Table 4.4: Compressive yield strength, Ultimate compressive strength (UCS) and % increase in the cross-section area for Ti-9Mo-7Nb-2Cu alloy, Ti-9Mo-7Nb-4Cu, and Ti-9Mo-7Nb-6Cu alloys ……...	77
Table 4.5: Computed values of average scratch COF, average scratch track width and depth, scratch volume, fracture toughness and scratch hardness number at different values of applied load for Ti-9Mo-7Nb-2Cu, Ti-9Mo-7Nb-4Cu, and Ti-9Mo-7Nb-6Cu alloys …….....	82
Table 4.6: presents the released amounts of metallic ions Ti, Mo, Nb, and Cu at pH 5.4 and 7.4 in SBF and PBS solutions with immersion duration, i.e., 1 to 3 weeks for Ti-9Mo-7Nb-2Cu, Ti-9Mo-7Nb-4Cu, and Ti-9Mo-7Nb-6Cu alloys …….	85

NOMENCLATURE

Symbol / Term	Description
μ	Micro
β-Ti	Beta titanium
α-Ti	Alpha titanium
at.%	Atomic percentage
wt%	Weight percentage
NL	Normal liter
w	Deposition width
h	Deposition height
Dd	Dilution depth
AD	Deposition area
Ad	Diluted area
AR	Aspect ratio
D	Dilution
η	Deposition efficiency
F'	Powder mass flow rate (g/min)
ρp	Density of the feedstock powder (g/mm^3)
ρe	Experimental density
ρt	Theoretical density
ma	Mass of each sample in air
mw	Mass of each sample in deionised (DI) water
ρi	Density of the *i*th element of the alloy
fi	Atomic fraction of the *i*th element of the alloy
w	Scratch width
d	Scratch depth
Hs	Scratch hardness number

Symbol / Term	Description
Sv	Scratch volume
F	Applied scratch load
D	Stylus diameter
L	Scratch length
Ft	Fracture toughness
S	Shape factor
Φ	Half apex angle
Fh	Horizontal scratch loads
Fv	Vertical scratch loads
α	Position of the cone-shaped diamond
Ncontrol	Number of bacterial colonies observed for the control sample
Nsample	Number of bacterial colonies observed for the test sample
AR	Antibacterial rate

ACRONYMS

Acronym	Full Form
AM	Additive Manufacturing
ASTM	American Society for Testing and Materials
CAD	Computer-Aided Design
STL	Stereolithography File Format
CNC	Computer Numerical Control
CAM	Computer-Aided Manufacturing
PBF	Powder Bed Fusion
DED	Directed Energy Deposition
EBM	Electron Beam Melting
SLS	Selective Laser Sintering
SLM	Selective Laser Melting
MJF	Multi Jet Fusion
DMLS	Direct Metal Laser Sintering
LENS	Laser Engineered Net Shaping
LMD	Laser Metal Deposition
WAAM	Wire Arc Additive Manufacturing
μ-PMAM	Micro-Plasma Metal Additive Manufacturing
LOM	Laminated Object Manufacturing
UAM	Ultrasonic Additive Manufacturing
PP	Polypropylene
MJM	Multi Jet Modeling
FDM	Fused Deposition Modeling
SLA	Stereolithography Apparatus
DLP	Digital Light Processing
FBAM	Fusion-Based Additive Manufacturing

Acronym	Full Form
SSAM	Solid-State Additive Manufacturing
GMA	Gas Metal Arc
MIG	Metal Inert Gas
TIG	Tungsten Inert Gas
GTA	Gas Tungsten Arc
PTA	Plasma Transferred Arc
CSAM	Cold Spray Additive Manufacturing
AFSD	Additive Friction Stir Deposition
FSPAM	Friction Stir Powder Additive Manufacturing
DLF	Directed Light Fabrication
DMD	Direct Metal Deposition
LBMD	Laser-Based Metal Deposition
LFF	Laser Freeform Fabrication
LDC	Laser Direct Casting
EBFF	Electron Beam Freeform Fabrication
HAZ	Heat-Affected Zone
μ-PPAM	Micro-Plasma Powder Additive Manufacturing
CP	Commercially Pure
HCP	Hexagonal Close-Packed
BCC	Body-Centered Cubic
CALPHAD	CALculations of PHAse Diagrams
PAAM	Plasma Arc Additive Manufacturing
UHV	Ultra-High Vacuum
MFA-AM	Magnetic Field-Assisted Additive Manufacturing
L-DED	Laser Directed Energy Deposition

Acronym	Full Form
LPBF	Laser Powder Bed Fusion
GMAW	Gas Metal Arc Welding
RO	Research Objectives
VMA-μPPAM	Vacuum- and Magnetically Assisted μ-Plasma Powder Additive Manufacturing
DC	Direct Current
SEM	Scanning Electron Microscopy
XRD	X-ray Diffractometer
WEDM	Wire Electric Discharge Machining
OFAT	One-Factor-at-a-Time
UTM	Universal Testing Machine
UTS	Ultimate Tensile Strength
SBF	Simulated Body Fluid
PBS	Phosphate-Buffered Saline
ICP-OES	Inductively Coupled Plasma Optical Emission Spectroscopy
DMEM	Dulbecco's Modified Eagle Medium
FBS	Fetal Bovine Serum
MTT	3-(4,5-dimethylthiazol-2-yl)-2,5-diphenyltetrazolium Bromide
DMSO	Dimethyl Sulfoxide
UV	Ultraviolet
LB	Lysogeny Broth
AR	Antibacterial Rate
NCD	Non-Uniform Discontinuous Deposition
UCD	Uniform and Continuous Deposition

Acronym	Full Form
UCS	Ultimate Compressive Strength
COF	Coefficient of Friction

Chapter 1

Introduction

1.1 Introduction to Additive Manufacturing

Manufacturing technologies have undergone a paradigm shift in recent decades, moving from conventional subtractive and formative processes towards layer-by-layer construction methods now collectively called Additive Manufacturing (AM) [1]. The evolution of AM from the late 1970s to the present has been remarkable. In 1977, pioneering work on directing a laser onto a tray submerged in liquid plastic to fuse solid layers was demonstrated. By 1986, Chuck Hull patented stereolithography, focusing UV light on a liquid photopolymer surface to create cross-linked layers. Rapid prototyping, rapid tooling, and eventually full-functional end-use manufacturing soon followed. By the early 2000s, AM began producing complete functional products. Boeing's debt of FAA-approved 3D-printed titanium parts for the 787 Dreamliner in 2017 marks a milestone in aerospace manufacturing (*Fig. 1.1*) [2].

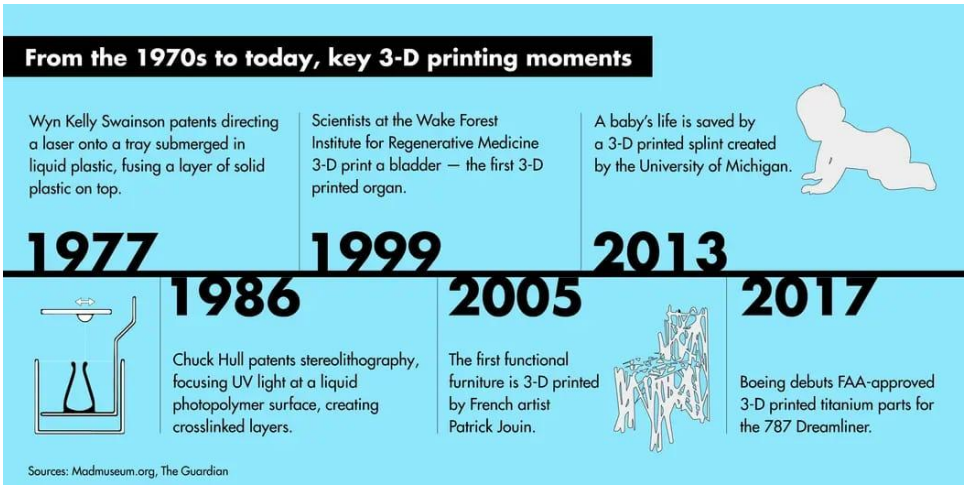


Fig 1.1: *Key developments in additive manufacturing since 1970s.*

American Society for Testing and Materials (ASTM) standard ISO/ASTM 52900:2021 formally defines additive manufacturing as "a process of joining materials to make objects from the data of 3D computer-aided design (CAD) model, usually layer upon layer, as opposed to subtractive manufacturing processes". The AM process is also referred to as 3D printing, freeform manufacturing, additive fabrication, or toolless manufacturing. A CAD model is created using appropriate design software, and its data is exported to a stereolithography (STL)

file format, which an AM machine can read. Some AM machines use a computer numerical control (CNC) part program written in G and M codes [1].

Metal additive manufacturing is gaining global attention for applications in the aerospace, biomedical, oil and gas, marine, automotive, sports, and luxury sectors due to features such as part design flexibility, component complexity, lightweighting, part consolidation, and design for function. AM is inherently interdisciplinary, utilising CAD, computer-aided manufacturing (CAM), advanced materials, robotics, sensing, monitoring, and control. It is recognized as one of the key enablers of Industry 4.0 [2].

1.2 Classification of Additive Manufacturing Processes

1.2.1 Classification According to ASTM F-42 Standard

According to the ASTM F-42 standard, different AM processes are classified into the following seven major categories: (i) Powder Bed Fusion (PBF), (ii) Directed Energy Deposition (DED), (iii) Sheet Lamination, (iv) Binder Jetting, (v) Material Jetting, (vi) Material Extrusion, and (vii) Vat Photo Polymerization. Table 1.1 presents their working principle, some examples, and applicable materials — i.e., the material type that can be used for making components from a particular category of AM process [2].

Table 1.1*: Classification of AM processes according to the ASTM F-42 standard [2]*

Category	Working Principle	Some Examples	Applicable Material
Powder Bed Fusion (PBF)	Thermal energy selectively fuses regions of a powder bed	EBM, SLS, SLM, MJF, DMLS	Metallic materials, Polymers
Directed Energy Deposition (DED)	Focused thermal energy fuses materials by melting as the material is being deposited	LENS, LMD, WAAM, μ-PMAM	Metallic materials
Sheet Lamination	Sheets of material are bonded to form an object	LOM, UAM	Metals, Fabric, Paper
Binder Jetting	A liquid bonding agent is selectively deposited to join powder materials	PBIH, Plaster-based 3D Printing (PP)	Metallic materials, Polymers
Material Jetting	Droplets of build material are selectively deposited	Multi-Jet Modelling (MJM)	Polymers, Waxes

Category	Working Principle	Some Examples	Applicable Material
Material Extrusion	Material is selectively dispensed through a nozzle or orifice	Fused Deposition Modelling (FDM)	Polymers
Vat Photo Polymerization	Liquid photopolymer in a vat is selectively cured by light-activated polymerization	Stereolithography (SLA), Digital Light Processing (DLP)	Photopolymers

1.2.2 Classification Based on Melting Requirement

The AM processes can also be classified according to the requirement of melting of the deposition or feedstock material and type of heat source (Fig. 1.2). Accordingly, the AM processes are divided into the following two major categories: (i) Fusion-Based Additive Manufacturing (FBAM) processes, which require melting of the feedstock material and are referred to as the Directed Energy Deposition (DED) process, and (ii) Solid-State Additive Manufacturing (SSAM) processes, which do not require melting of the feedstock material [1], [2].

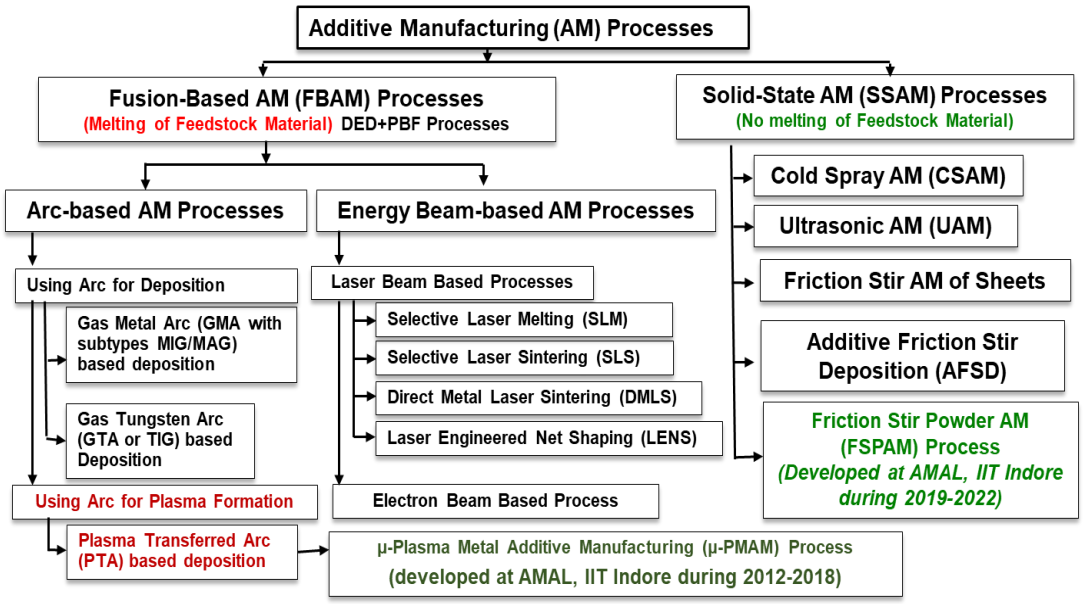


Fig 1.2: *Classification of metal additive manufacturing processes according to melting requirement of the feedstock material [1], [2]*

The FBAM-type processes have unique multi-functional capabilities of freeform manufacturing of complicated parts, coating, cladding, surface texturing, surface alloying, repairing, remanufacturing, rapid prototyping, and rapid tooling. They are used for various applications in the fields of biomedical, post-injury rehabilitation, aerospace, automobile, marine, power generation, gas turbines, oil and gas extraction, and sports equipment [1].

1.3 Fusion-Based Additive Manufacturing Processes

1.3.1 Beam-Based AM Processes

(a) Laser Beam-Based Processes

Laser beam is the most commonly used heat source in commercially available FBAM machines. The process of Laser Engineered Net Shaping (LENS) was developed at Sandia National Laboratories in 1995 and commercialized by Optomec in 1998. It is also referred to as Directed Light Fabrication (DLF), Direct Metal Deposition (DMD), Laser-Based Metal Deposition (LBMD), Laser Freeform Fabrication (LFF), Laser Direct Casting (LDC), 3D Laser Cladding, Laser Cast, and Laser Consolidation. Different types of lasers used in commercial FBAM machines include CO_2 laser, Nd:YAG laser, Yb-fiber laser, and Excimer laser [3], [4]. Laser-based FBAM processes are generally applicable to powder form of the feedstock material. High-intensity laser irradiation is focused to fuse the feedstock material particles which solidify to form a deposition layer on the substrate or previously deposited layer. Significant process parameters include spot size, beam power, beam focal offset, flow rate, morphology and moisture content of feedstock powder, travel speed of the deposition head, and inert gas flow. The deposition process is carried out with a coaxially flowing shielding gas to protect the melt pool or in a hermetically sealed chamber filled with argon gas to regulate the oxygen and moisture level [5].

(b) Electron Beam Based Processes

Electron beam-based FBAM is another category of FBAM process developed by NASA Langley Research Center and named as Electron Beam Freeform Fabrication (EBFF) process. It uses a high-power electron beam in a highly vacuum environment (10^{-4} torr or below) to melt the feedstock material, thus eliminating the need for a shielding gas as used in laser-based FBAM processes. The EBFF process can be used to build very complicated components using wire form of feedstock material and has been found to have almost 100% deposition efficiency and 95% efficiency in power utilization. It can be applied for materials having high reflectivity

such as aluminum, copper, and their alloys, for which laser-based FBAM processes cannot be used [1].

1.3.2 Arc-Based AM Processes

Arc-based FBAM processes have low machine cost, less build time, and better deposition efficiency compared to laser and electron beam-based processes. Spencer and Dickens from the University of Nottingham conducted a feasibility study in 1998 using Gas Metal Arc (GMA) or metal inert gas (MIG) in a FBAM process by generating an arc between the consumable wire electrode and substrate to fuse the wire to make its deposition. The deposition melt pool was protected by a shielding gas flowing through the GMA torch and does not require any customized

working environment. This process has low buy-to-fly ratios, higher deposition rates, and unlimited built volume potential, but is limited to wire form of feedstock only [6], [7].

Gas Tungsten Arc (GTA) or Tungsten Inert Gas (TIG)-based FBAM is another arc-based deposition process where the arc is generated between the non-consumable tungsten electrode and the metallic substrate to fuse the feedstock material. The melt pool is protected by shielding gas flowing through the GTA torch. It does not require any customized working environment for deposition as required in the case of laser or electron beam-based FBAM processes. However, heat accumulation, accuracy, and surface roughness are major drawbacks associated with multi-layer depositions made by arc-based FBAM processes [8].

Plasma arc-based FBAM is another arc-based process where plasma is generated from a tungsten electrode within the nozzle and forced through a hole in it which constricts the arc, resulting in arc stability even at low current, higher energy density, smaller Heat-Affected Zone (HAZ), and less thermal distortion as compared to GTA and GMA-based FBAM processes. Since the electrode is inside the nozzle, deposition material refrains from encountering the feedstock material, enabling this process to use both powder and wire form. Jhavar et al. (2014a) developed a new process named micro-plasma powder additive manufacturing (μ-PPAM) at IIT Indore (India) to reduce heat input during deposition. It has been successfully used for deposition of wire of AISI P20 tool steel, repairing of dies and molds, deposition of powder of Ti-6Al-4V, coating of Stellite 6 powder, and dimple and spot texturing on high-speed steel cutting tools [9], [10], [11], [12].

1.4 Advantages of Additive Manufacturing Processes

Following are some unique advantages offered by the AM processes:

- **Free-form fabrication:** The AM processes have potential to manufacture components having intricate geometry which are impractical to produce using any other manufacturing process. They surpass the limitations of conventional manufacturing processes such as casting, forming, powder metallurgy, and machining [1], [2].
- **Digital-driven fabrication is highly controllable and repeatable:** Optimized complicated geometries of products generated by a computer program can be manufactured repeatedly by AM processes with the same accuracy [2].
- **Development of different materials:** Functionally graded materials, shape memory materials, biomaterials, and smart materials can be developed by AM processes using their constituents in the desired proportion [1]**Personalized manufacturing at low cost:** Traditional large-scale production usually needs an expensive prefabricated mold, which is a time-consuming process. AM processes allow solid realization directly from a CAD model without a mold, which is much more efficient and cheaper. This is favored in applications such as multi-functional surgical tools, customized bone replacement, and heritage replication and repair [1], [2].
- **Automatic manufacturing process:** Computer-designed part geometries and multi-material manufacturability of AM processes allow unmanned manufacturing of a complicated product and material-diverse object through a single machine [2].
- **Reduction of material waste:** In conventional manufacturing processes, material is typically removed from a larger-size piece. In contrast, AM starts from scratch, adding material to create a component or part. By using the substance only to create a part, AM ensures minimal waste and reduces the need for tooling [1], [2].
- **Environment friendliness:** AM processes yield significant saving of material, energy, and time as compared to traditional manufacturing processes such as casting, machining, and forming. Most of the processes do not emit harmful gases, making AM processes very environmentally friendly [1].

1.5 Limitations of Additive Manufacturing Processes

Although AM processes offer many significant advantages, they still suffer from the following limitations:

- **Material limitation:** Machines for an AM process are usually designed for a limited range of materials that have similar properties. This restricts processing of entirely different materials on a particular AM machine. Developments in materials science can considerably contribute in realization of AM technology [1], [2].
- **Large manufacturing time for large-scale production:** Even though AM is good at making customized products, the technology is positioned in the small-scale production sector. There are constraints on the size of AM machines and additively manufactured components. Preferably, AM processes are frequently used to manufacture complex geometries that are usually unmanageable in traditional ways [1].
- **Poor manufacturing accuracy:** The layered manufacturing strategy of AM processes ignores the edge shape in a single layer in the spatial direction to fit the real surface curvature. The layered structure on the surface is not ignorable [1].
- **Post-processing requirements:** Generally, AM processes are not net-shape manufacturing processes but only a core step of the process. The AM-manufactured component requires further processing to be a functional product [2].
- **Large cost for metallic materials:** Though production costs of additively manufactured components are quite favorable and economically attractive for polymers, wax, and fabric materials, production costs of additively manufactured metallic components are high due to the complexity of obtaining the required metallic material in the desired form [1].

1.6 Introduction to Titanium Alloys

Continuous evolution of industrial technologies necessitates development of novel materials with tailored properties to meet application-specific requirements across aerospace, automobile, marine, biomedical, energy, chemical, sports, and other industries [13]. Researchers are actively engaged in developing lighter, stronger, novel, and biocompatible materials to address key engineering challenges that include: applications requiring better performance at elevated temperatures and harsh environments; enabling production of next-generation high-strength lightweight aircraft and automotive parts; seamless integration with

the human body to improve orthopedic and dental implant success rates; superior corrosion and heat resistance for chemical and pharmaceutical industries; and minimization of adverse environmental impacts.

Advanced computational tools are enabling researchers to model and simulate the behavior of developed materials at the atomic level, facilitating precise prediction and optimization of their properties. Traditional materials such as iron, nickel, copper, aluminum, magnesium, and their alloys have been extensively studied for their diverse properties and continue to find numerous applications across different industries. Fig. 1.3 shows the strength-to-weight ratio and fracture toughness for different materials; these properties play a vital role in the selection of materials for diverse industries.

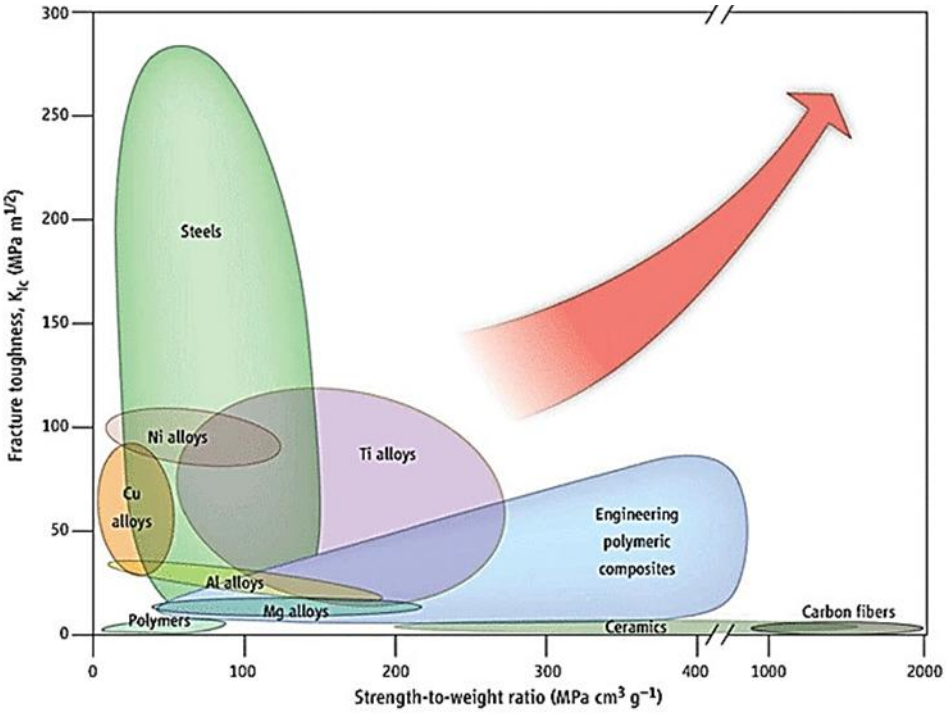


Fig 1.3: *Strength-to-weight ratio and fracture toughness for various metals and alloys [13].*

As seen from Fig. 1.3, steel and nickel alloys possess higher toughness but lower strength-to-weight ratio, whereas aluminum alloys, magnesium alloys, and polymers have high strength-to-weight ratio but possess less toughness. In this context, Ti alloys offer a desirable balance between strength-to-weight ratio and fracture toughness. Low density of Ti alloys reduces weight of aerospace and automotive parts, translating to reduced fuel consumption and operational costs. They also have higher specific strength over a considerable range of service temperature and smaller corrosion rate, leading to extended service life and reduced

maintenance cost [14]. Ti alloys containing α-Ti and β-Ti phases, and metastable β-Ti alloys are particularly attractive for both aerospace and automotive applications.

1.6.1 Classification of Titanium Alloys

Ti alloys are categorized into five groups based on the phases present at room temperature as shown in Fig. 1.4 and summarized below.

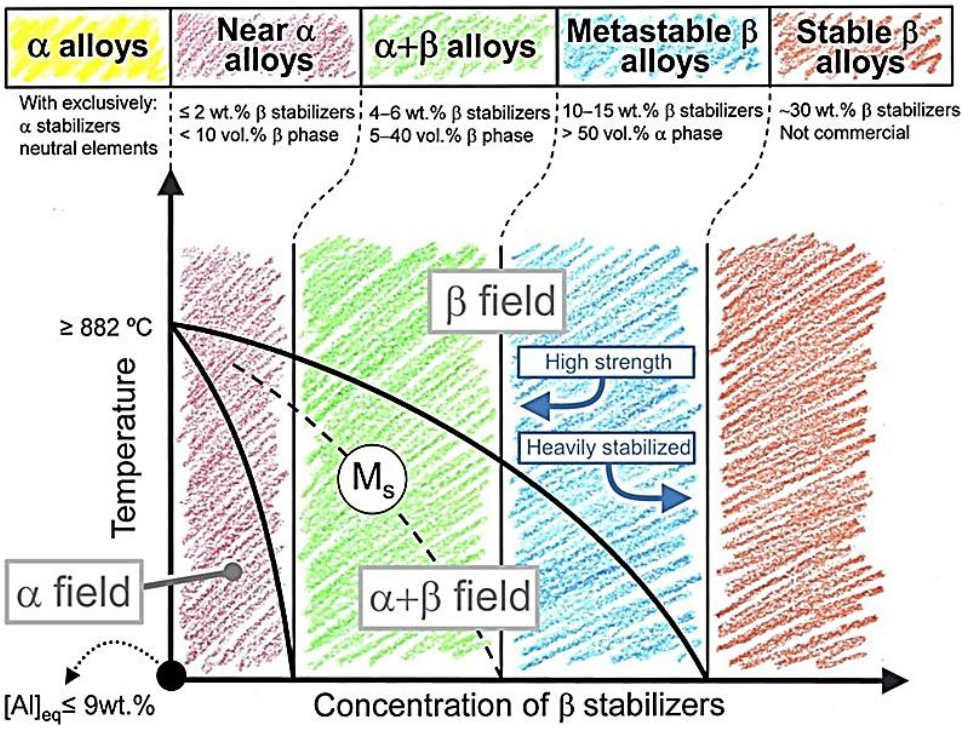


Fig 1.4: *Classification of Ti alloys based on phases present at room temperature*

- **α-Ti alloys:** contain maximum amount of commercially pure (CP) Ti, α-Ti phase stabilizers (i.e., aluminum, boron, rare earth elements, germanium, and gallium), neutral elements (i.e., tin and zirconium), and minimal amounts of impurities such as carbon, oxygen, and nitrogen. They have hexagonal close-packed (HCP) crystal structure at room temperature and are commonly used in chemical and marine industries due to their superior corrosion and creep resistance. However, their low strength limits high-strength applications. Ti-5Al-2.5Sn alloy is the most commonly used α-Ti alloy for making honeycomb structures and turbomachinery pumps [15].
- **Near α-Ti alloys:** contain 5–10 vol.% of β-Ti phase (BCC crystal structure) and up to 2 wt.% of β-Ti phase stabilizers. The presence of β-phase stabilizers modifies their microstructure, enhances their properties, and stabilizes the β-Ti phase at room temperature. Ti-3Al-2.5V is a widely used near α-Ti alloy in aircraft hydraulic tubing.

Other near α-Ti alloys such as Ti-6Al-2Sn-4Zr-2Mo and Ti-5.8Al-4Sn-3.5Zr-0.5Mo-0.7Nb-0.35Si are used in aerospace applications due to their high strength, toughness, and creep resistance at elevated temperatures (up to 500°C) [16], [17], [18].

- **α+β Ti alloys:** contain 5 to 40 vol.% of β-Ti phase, 4 to 10 wt.% of β-Ti phase stabilizers, and α-Ti phase stabilizers. The β-Ti phase stabilizers modify their microstructure, enhance properties, and stabilize the β-Ti phase. These alloys are widely used in aerospace, automotive, shipbuilding, and chemical industries due to their lightweight, high strength, good corrosion and oxidation resistance, and excellent high-temperature strength (up to 600°C). Ti-6Al-4V is the most commonly used α+β Ti alloy [19], [20], [21].
- **Metastable β-Ti alloys:** contain more than 50 vol.% of β-Ti phase, 10 to 20 wt.% of β-Ti phase stabilizers. The β-Ti phase is not thermodynamically stable but is kinetically trapped due to rapid cooling or addition of specific alloying elements. These alloys possess high strength, good formability, excellent corrosion resistance, lower Young's modulus, and higher capacity for mechanical damping compared to α+β Ti alloys, making them well-suited for biomedical and aerospace applications [22], [23].
- **β-Ti alloys:** primarily consist of β-Ti phase only with more than 30 wt.% of β-Ti phase stabilizers. They possess high-temperature strength, high wear, corrosion, fatigue, and creep resistance, and higher thermal stability. However, they have drawbacks such as embrittlement, self-diffusion, creep failure at high temperatures, and formation of brittle phases, which restrict their applications [22].

1.6.2 Phase Stabilizing Elements for Titanium Alloys

Phase stabilizing elements for Ti alloys are classified into three categories based on their effects on the microstructure, solubility, and phase stability: α-Ti phase stabilizing elements, β-Ti phase stabilizing elements, and neutral elements. They can either increase or decrease the β-transus temperature as depicted in table1.2. The addition of these phase stabilizing elements significantly affects the final microstructure of Ti alloys.

Table 1.2: *Summary of phase stabilizing elements for Ti alloys and their effects*

Element Type	Effect on β-Transus	Examples
α-Ti Phase Stabilizing Elements	Increase β-transus temperature	Substitutional: Al (most used), B, Ga, Ge, rare earth elements Interstitial: O, N, C
β-Ti Phase Stabilizing Elements	Decrease β-transus temperature	β-isomorphous: V, Mo, Nb, Ta, Re β-eutectoid: Fe, Cu, Ni, Cr, Co, Mn, Si
Neutral Elements	Minimal effect on β-transus	Sn and Zr (high solubility in Ti); act as strengthening agents

- **α-Ti phase stabilizing elements:** are soluble in α-Ti phase and increase the β-transus temperature. They are further classified as substitutional and interstitial elements. Aluminium is the most widely used substitutional type stabilizer for the α-Ti phase. Boron, gallium, germanium, and rare earth elements are other substitutional type stabilizers with limited solubility. Oxygen, nitrogen, and carbon are interstitial type stabilizers. Addition of α-Ti phase stabilizers improves corrosion resistance, flow stress, thermal stability, thermal and electrical conductivity, and weldability of Ti alloys [24], [25].
- **β-Ti phase stabilizing elements:** readily dissolve in β-Ti phase and decrease the β-transus temperature. They are further categorized as β-isomorphous and β-eutectoid. Vanadium, molybdenum, niobium, tantalum, and rhenium are important β-isomorphous elements for stabilizing the β-Ti phase due to their high solubility. Iron, copper, nickel, chromium, cobalt, manganese, and silicon are important β-eutectoid elements due to their limited solubility; addition of higher amounts can promote formation of intermetallic phases that degrade mechanical properties [26], [27], [28], [29].
- **Neutral elements:** are soluble in both α-Ti and β-Ti phases with minimal influence on the β-transus temperature. Tin and zirconium are important neutral elements due to their high solubility in Ti. These neutral elements can act as strengthening agents and slow down kinetic reactions [30], [31].

1.6.3 Need for Enhancing Properties of Titanium Alloys

Manufacturing useful engineering components from newly developed novel materials presents major challenges, such as their unavailability in raw form for manufacturing useful components and limited understanding of their structure-property relationships. Moreover, these materials may experience degradation of their useful properties during manufacturing of components and often incur higher manufacturing costs [32], [33]. Ti alloys suffer from certain limitations such as strength reduction at temperatures exceeding 600°C, and low values of fatigue strength, fracture toughness, modulus of elasticity, wear resistance, abrasion resistance, corrosion resistance, oxidation resistance particularly at elevated temperature, and surface hardness [34], [35]. Table 1.3 presents a summary of typical applications of Ti alloys and the corresponding properties required for these applications.

Table 1.3: *Summary of typical applications of Ti alloys and their required properties [32], [35].*

Industry Type	Typical Applications	Required Properties
Aerospace	Propeller, stator and rotor blade, engine valve, casing, and disk	High strength, hardness, fatigue strength, corrosion resistance and oxidation resistance
Biomedical	Knee and hip joint, dental implant, stent, bone and cranial plate, cardiac intima	Low elastic modulus; high corrosion and wear resistance; good biocompatibility
Marine & Shipbuilding	Pressure vessels, pump, fire extinguisher, riser, pipe	High corrosion resistance and strength
Chemical Industries	Heat exchanger, reactor, piping, pump, reaction tower, autoclave	High corrosion resistance and oxidation resistance

Industry Type	Typical Applications	Required Properties
Automotive	Connecting rods, exhaust pipes, valve and valve springs, mufflers	Low density; high specific strength, wear resistance, toughness and fatigue resistance
Defense	Wheel, tank, cannon barrel, tailstock, shaft	High strength, corrosion resistance; low density

Reduced values of wear resistance, fatigue strength, fracture toughness, and creep strength of Ti alloys at elevated temperature restrict their aerospace applications. Whereas reduced values of corrosion resistance, abrasion resistance, fatigue strength, fracture toughness, and increased stress corrosion cracking restrict their marine applications. Biomedical applications of some Ti alloys (such as Ti-6Al-4V) are restricted due to their relatively higher modulus of elasticity which can lead to stress shielding effect; they also have relatively less fatigue strength, corrosion resistance, and wear resistance in the human body environment, which can cause failure of knee, hip, and dental implants [36]. The aforementioned limitations of Ti alloys and failures of their components in different industries necessitate enhancement of their properties.

1.7 Design Using CALPHAD Modelling

A simulation software known as CALPHAD (an acronym of CALculations of PHAse Diagrams) is most commonly used for predicting and understanding the phase equilibria in a multi-component alloy. It leverages thermodynamic databases and computational algorithms to simulate the phase diagrams of a multi-component alloy, thus enabling the researchers to predict the phases that will form under various combinations of temperature and composition. The CALPHAD software offers a more comprehensive and versatile approach as compared to the traditional design approach based on thermodynamic and Hume-Rothery parameters, making it a preferred choice for researchers to design and understand different phases of a multi-component alloy [37], [38], [39].

The CALPHAD approach has been used for Thermo-Calc simulations of Ti-based multi-component alloys such as Al-Cr-Nb-V-Mo, Ti-6Al-4V-0.9Ni, and Ti-6Al-4V-3Cu. Simulation results from the CALPHAD generally show good agreement with the experimental results for various multi-component alloys.

1.8 Applications of Properties-Enhanced Titanium Alloys

Properties-enhanced Ti alloys find many applications in aircraft, spacecraft, biomedical, automotive, marine, and chemical industries which are described in the following paragraphs.

(a) Aerospace Applications

Properties-enhanced Ti alloys are being used in aerospace applications due to their enhanced corrosion resistance, fatigue, and fracture toughness and their inherent high strength-to-weight ratio. They are used for fabrication of lightweight, durable, and fuel-efficient aircraft components such as airframes, wing box, skin panel, landing gear, and cockpit window frame [40], [41]. They are also used in the components of a jet engine such as fan blades and casing, compressor blades and casing, rotors disc and blade, and stator blade due to their enhanced creep resistance, corrosion resistance, and high-temperature strength. They are also used for manufacturing spacecraft components such as satellite frames, payload housings, and propulsion systems, as well as missile components including airframes, fuel tanks, and guidance systems.

(b) Biomedical Applications

Properties-enhanced Ti alloys are being used in different biomedical and dental applications. It is due to their very good biocompatibility, osseointegration, enhanced corrosion and wear resistance inside the human body, and lower modulus of elasticity. They are widely used to manufacture orthopedic implants for the replacement of knee joints, elbow joints, hip joints, and shoulder joints, and for fabrication of bone plates, screws, and spinal implants [42], [43].They are also used for patient-specific mandibular prosthetic implants in maxillofacial clinical applications, cranial plates and mesh for cranioplasty applications, and dental implants which serve as artificial tooth roots to support dental prostheses such as crowns, bridges, and dentures.

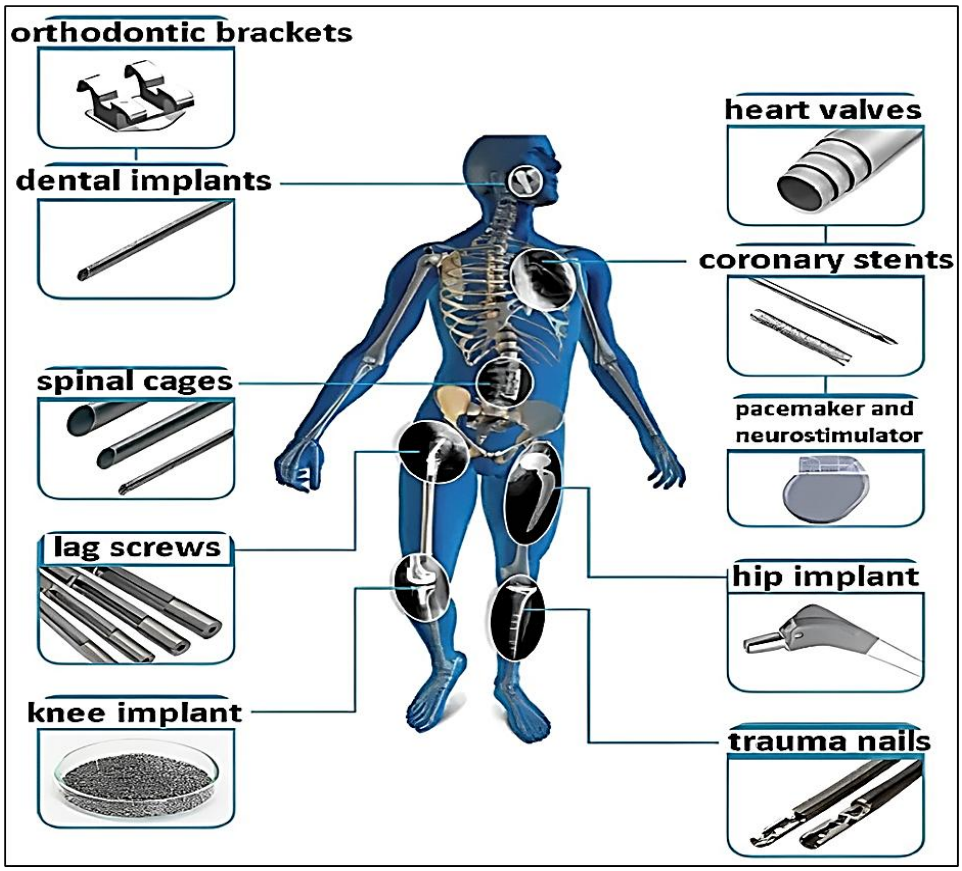


Fig 1.5: *Some biomedical applications of Ti alloys with enhanced properties [30].*

(c) Marine and Chemical Industry Applications

Properties-enhanced Ti alloys are used in manufacturing chemical plant items such as tanks, vessels, reactors, heat exchangers, pumps, valves, and piping systems due to their high corrosion and oxidation resistance in alkaline and acidic environments [32]. They are used in marine applications to manufacture ship hull, propeller, heat exchanger, engine valve, and piping systems. It is due to their high corrosion resistance in saline and reactive environments and wear resistance under extreme sea weather [44], [45].

(d) Automotive Applications

Properties-enhanced Ti alloys are used in racing cars for manufacturing exhaust systems, suspension components (such as coil springs and shock absorbers), engine components (such as connecting rods and intake valves), and turbocharger components due to their high strength, fatigue and toughness, and corrosion resistance. However, their higher cost and manufacturing challenges restrict their large-scale applications in the automotive industry.

1.9 Organization of the Thesis

This thesis is organized into six chapters which explain all the aspects of the present research work:

- **Chapter 1:** Provides a brief overview of introduction to additive manufacturing (AM), their classifications and applications as well as a brief about Ti alloys, their classification, and phase stabilizing elements. It also discusses the need for enhancing properties of Ti alloys, different methods for it, and design methodology of multi-component alloys,
- **Chapter 2:** Presents a comprehensive literature review of previous research on vacuum and magnetically assisted process and ti based material, identification of gaps, research objectives, and the methodology adopted to meet the identified research objectives.
- **Chapter 3:** Presents details of preparation of powders, design and planning of experiments, apparatus, evaluation of different responses, including in-vitro biocompatibility, microstructure, evolution of phases, mechanical characteristics and fracture toughness.
- **Chapter 4:** Describes results and their analyses of materials developed through the μ-PPAM process, covering microstructure analysis, microhardness, tensile and compression tests , fracture toughness and in-vitro biocompatibility assessment,
- **Chapter 5:** Summarises the conclusions derived from the research, key contributions, and future scope of the work.
- **Chapter 6:** Lists all references cited in this thesis.

Chapter 2

Review of Past Work and Research Objectives

This chapter describes the previous research work on the use of different vacuum- and magnetic-assisted additive manufacturing techniques and their applications. It also discusses Ti-based biomaterials and their advancements over time for orthopedic implant applications. Furthermore, the chapter presents a summary of relevant past studies, identifies existing research gaps and objectives, and explains the methodology adopted to achieve the identified research objectives.

2.1 Recent Advances in Vacuum-Assisted Metal Additive Manufacturing

Vacuum-assisted additive manufacturing (AM) has emerged as an important approach for producing high-quality metallic components with improved mechanical performance, reduced porosity, and enhanced metallurgical integrity. The application of vacuum environments during metal additive manufacturing is particularly beneficial for reactive metals such as titanium and its alloys, which are highly susceptible to oxidation and contamination at elevated temperatures. In conventional atmospheric processing, molten titanium easily reacts with oxygen, nitrogen, and hydrogen, leading to oxide formation, embrittlement, and deterioration of mechanical properties. Therefore, vacuum-assisted systems are increasingly utilized in advanced manufacturing sectors such as aerospace, biomedical implants, and space applications where high material purity and structural reliability are essential [46], [47], [48], [49].

A vacuum environment significantly minimizes atmospheric contamination during deposition and solidification. The reduced oxygen partial pressure suppresses oxidation and prevents the formation of brittle oxide inclusions within the deposited layers. As a result, improved metallurgical bonding, enhanced density, lower porosity, and superior mechanical properties are achieved [46], [47]. In titanium-based biomedical alloys, vacuum processing is especially important because contamination-free surfaces improve corrosion resistance, biocompatibility, and long-term implant performance [46]. Furthermore, reduced contamination contributes to better fatigue strength and fracture resistance, which are critical requirements for orthopaedic and load-bearing biomedical applications [48].

Among various vacuum-assisted AM technologies, Electron Beam Melting (EBM) is one of the most established processes. EBM operates inside a high-vacuum chamber, generally

maintained at pressures around 10^{-3}mbar, to allow efficient propagation of the electron beam without scattering by atmospheric gases. The vacuum environment ensures precise energy transfer to the powder bed and enables uniform melting and solidification. In addition, the vacuum promotes in-situ degassing of metal powders by removing trapped gases and moisture prior to melting, thereby reducing gas porosity in the fabricated components [49]. The absence of oxygen during processing also prevents oxidation of reactive metals such as titanium, resulting in cleaner microstructures and improved mechanical performance. These advantages make EBM highly suitable for aerospace and biomedical applications requiring near-fully dense metallic parts [49], [50].

Vacuum environments are also beneficial in plasma arc additive manufacturing (PAAM) and directed energy deposition (DED) systems. In these processes, the controlled atmosphere minimizes oxidation and stabilizes the molten pool during deposition. *DebRoy et al.* reported that vacuum-assisted or low-pressure environments improve arc stability, reduce contamination, and enhance layer bonding in metallic AM systems. Moreover, inert gas backfilling after vacuum generation can provide a stable arc environment while still maintaining low oxygen levels during deposition [5]. Such hybrid vacuum–inert gas systems are increasingly adopted to improve process reliability and deposition quality in titanium alloy manufacturing.

Despite these advantages, several technical challenges are associated with vacuum-assisted AM systems. One major challenge is maintaining stable vacuum conditions in large manufacturing chambers. Leakage, improper sealing, and outgassing from chamber walls significantly increase evacuation time and reduce vacuum efficiency [47]. Outgassing refers to the release of absorbed or trapped gases from internal chamber surfaces and is considered a major limitation in achieving ultra-high vacuum conditions. Water vapor is one of the primary contributors to outgassing in vacuum systems. To overcome this issue, bake-out techniques are commonly employed to remove adsorbed gases from chamber surfaces before operation [51].
Another challenge in vacuum-assisted AM is the generation of metal vapors and powder spattering during high-energy melting processes. Metallic vapors can contaminate chamber walls, sensors, and vacuum pipelines, thereby affecting process stability and increasing maintenance requirements. Fine metal powders may also enter vacuum pumps and damage internal components, particularly in rotary and turbomolecular pumps [48]. To address these

problems, researchers have proposed the use of multi-stage vacuum systems integrated with high-efficiency filtration units between the chamber and the pump. Water-cooled chamber walls and shielding systems are additionally employed to reduce thermal deposition and vapor accumulation inside the chamber [51].

Vacuum heat treatment is another important application associated with additive manufacturing. Additively manufactured metallic parts often contain significant residual stresses because of rapid heating and cooling cycles during deposition. These stresses can lead to distortion, cracking, and premature failure of components [52]. Vacuum heat treatment processes such as annealing, stress relieving, and solution treatment are therefore widely used to improve microstructural homogeneity and mechanical performance. Since these treatments are carried out in oxygen-free environments, surface oxidation is avoided while residual stresses are effectively reduced [50], [52]. Consequently, improved ductility, dimensional stability, and fatigue resistance are obtained in the manufactured components [50].

Recent research has also demonstrated the application of additive manufacturing in ultra-high vacuum (UHV) systems and space manufacturing technologies. Additively manufactured vacuum chambers have achieved pressures below 10^{-10}mbar, demonstrating their feasibility for portable quantum technologies and accelerator systems [51]. Furthermore, vacuum-compatible fused filament fabrication systems have been investigated for in-space manufacturing applications where convective heat transfer is absent [53]. These developments indicate the growing importance of vacuum-assisted AM in advanced engineering applications requiring high precision and contamination-free manufacturing environments.

Vacuum-assisted additive manufacturing plays a crucial role in improving the quality and performance of metallic components by minimizing oxidation, reducing porosity, enhancing metallurgical bonding, and enabling efficient post-processing heat treatments. Vacuum environments are particularly beneficial for titanium-based biomedical alloys and aerospace materials, where high purity and superior mechanical properties are essential. Although challenges such as outgassing, vacuum leakage, and powder contamination remain significant, advancements in vacuum system design, filtration technologies, and process monitoring have considerably improved the reliability and efficiency of vacuum-assisted AM systems. Therefore, vacuum-assisted additive manufacturing continues to be an important research area for the development of high-performance metallic components.

2.2 Influence of Magnetic Fields on Melt Pool Behaviour and Microstructure in Metal Additive Manufacturing

Magnetic field-assisted additive manufacturing (MFA-AM) has emerged as an advanced approach for improving melt pool stability, refining microstructure, and enhancing the mechanical performance of metallic components produced through additive manufacturing (AM). In metal AM processes, rapid melting and solidification generate steep thermal gradients, unstable molten pool flow, and non-uniform element distribution, which often result in porosity, cracking, coarse dendritic structures, and anisotropic mechanical properties [54], [55]. These defects are particularly significant in titanium alloys, nickel-based superalloys, and stainless steels used in aerospace, biomedical, and high-temperature engineering applications [56]. Therefore, external magnetic fields are increasingly applied during additive manufacturing to regulate melt pool dynamics, control heat and mass transfer, and improve the final properties of deposited materials.

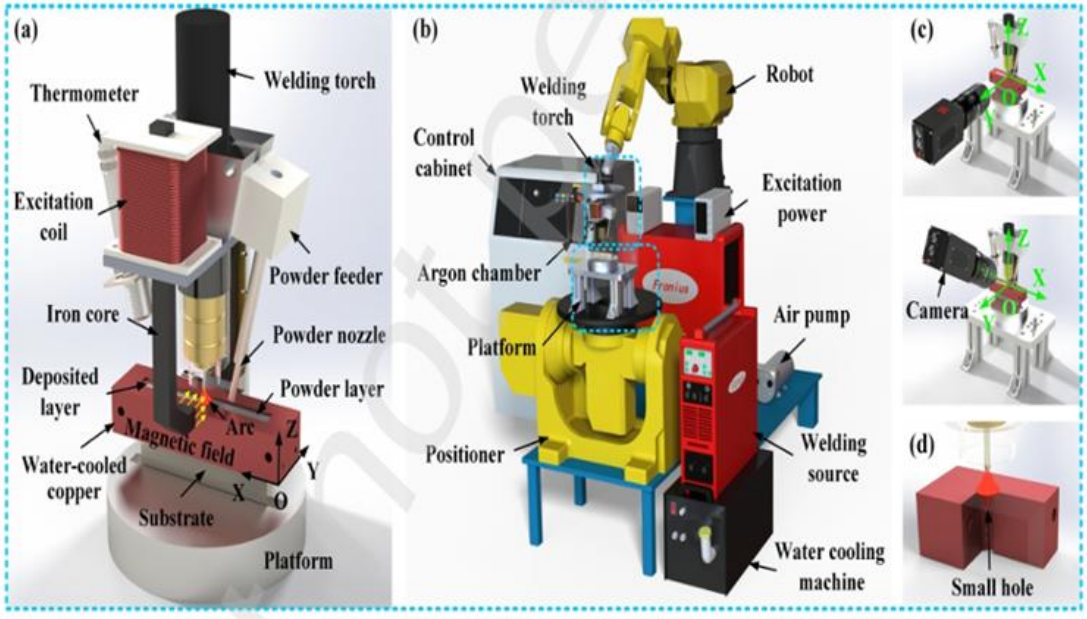


Fig 2.1: *Schematic diagram of MFA-PAAM; (b) MFA_PAAM system; (c) Angle of placement for high-speed camera shooting; (d) Sketch map of the arch pressure measuring device [57]*

The application of magnetic fields significantly influences melt pool behavior during metal deposition. When an external magnetic field interacts with the electrically conductive molten metal, Lorentz forces are generated inside the melt pool. These forces alter the molten metal flow pattern, enhance convection, and homogenize temperature distribution during

solidification [58]. Magnetic stirring additionally suppresses excessive Marangoni convection and stabilizes the molten pool, thereby reducing thermal gradients and minimizing residual stresses [59]. Zhou et al. demonstrated that the application of an external longitudinal magnetic field during arc-based additive manufacturing induced tangential stirring forces in the melt pool, which improved bead geometry and enhanced surface accuracy [60]. Similarly, Liu et al. reported that magnetic-field-induced rotation of molten droplets improved heat distribution and suppressed the formation of brittle intermetallic phases during welding and additive manufacturing processes [61].

Magnetic fields also play a significant role in grain refinement and microstructural evolution during solidification. In conventional additive manufacturing, rapid cooling often results in coarse columnar dendrites and non-uniform grain growth along the build direction. The introduction of magnetic fields modifies the solidification process by increasing melt pool convection and enhancing nucleation rates, which leads to the formation of finer and more equiaxed grains [62]. Wang et al. investigated the effect of magnetic fields on Inconel 625 fabricated by wire arc additive manufacturing (WAAM) and observed significant refinement of dendritic structures under magnetic stirring conditions. The magnetic field reduced dendrite size to nearly one-third of that produced without magnetic assistance and improved the uniform distribution of alloying elements such as Nb and Mo. Consequently, the fabricated alloy exhibited higher tensile strength, microhardness, and elongation due to refined microstructure and reduced elemental segregation [63].

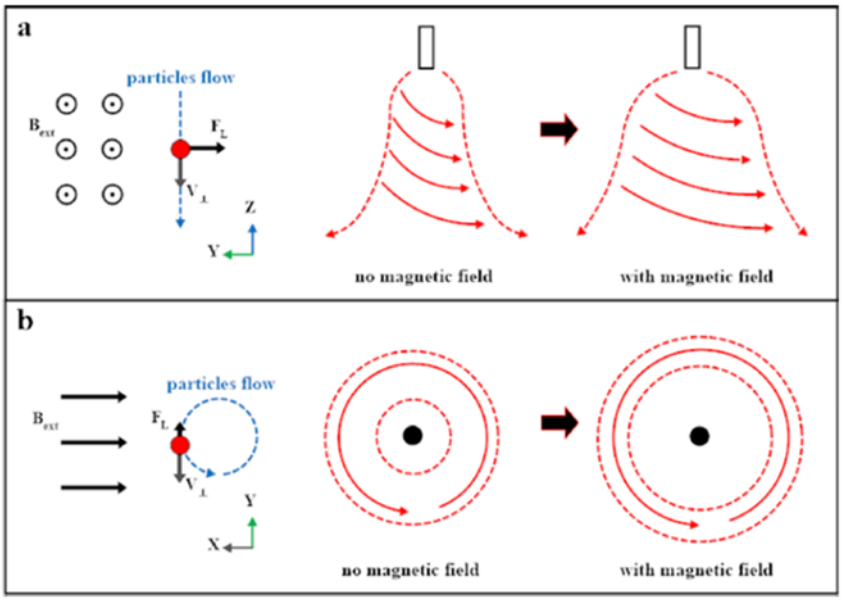


Fig 2.2: *Schematic diagram of magnetic field, showing: (a) the effect of steady magnetic field on arc during WAAM in yz plane and (b) in xy plane (Red dots are the charged particles and black dots are the magnetic lines) (For interpretation of the references to colour in this figure legend, the reader is referred to the web version of this article) [Source].*

In titanium alloy additive manufacturing, static magnetic fields have also demonstrated considerable improvements in microstructural control and mechanical properties. Zhao et al. fabricated Ti-6Al-4V alloy using laser directed energy deposition (L-DED) under a static magnetic field and reported refined β-grains and discontinuous α-grain boundaries [64]. The refined grain structure significantly improved ductility and elongation of the alloy. Similarly, Zhou et al. studied magnetic field-assisted laser powder bed fusion (LPBF) of SS316L stainless steel and observed suppression of epitaxial dendritic growth along the build direction. The magnetic field promoted the formation of equiaxed grains, reduced dislocation density, and improved ductility while minimizing crack formation during tensile loading [65].

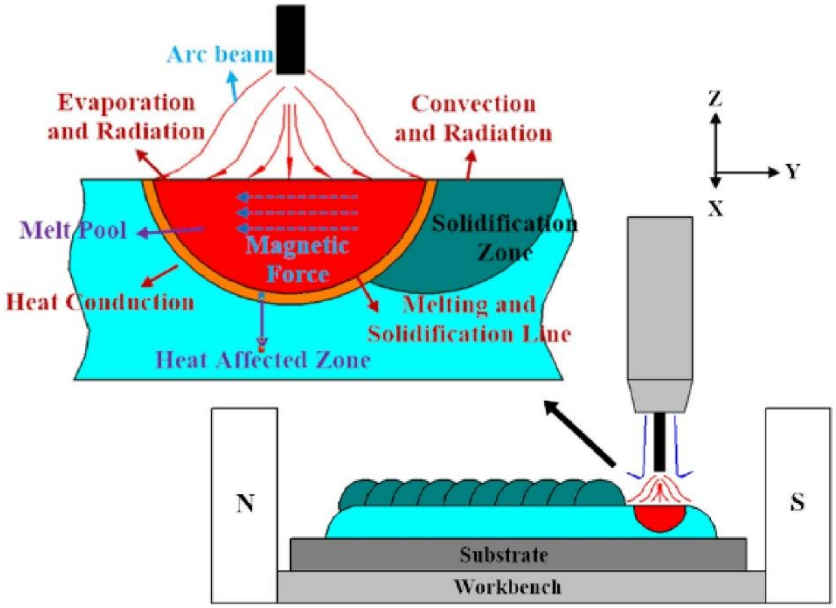


Fig 2.3: *Schematic representation of WAAM deposition process [Source]*

Magnetic fields additionally contribute to porosity reduction and improved deposition quality in additive manufacturing processes. During conventional deposition, unstable arc behavior and powder spattering frequently produce defects such as pores, incomplete fusion, and rough surface morphology [55]. The application of magnetic fields stabilizes the plasma arc and regulates powder flow, thereby improving melt pool stability and deposition efficiency [66]. Guan et al. reported that magnetic field-assisted gas metal arc welding (GMAW) reduced

spatter formation and refined the weld microstructure, leading to increased tensile strength [67]. Furthermore, magnetic-field-assisted directed energy deposition of 316L stainless steel resulted in reduced porosity, finer grains, and enhanced hardness without significantly affecting ductility. These improvements are primarily attributed to enhanced molten metal convection and uniform heat transfer under magnetic influence [68].

The influence of magnetic fields on additive manufacturing is strongly dependent on magnetic field intensity and orientation. Moderate magnetic fields generally improve melt pool convection and grain refinement; however, excessively high magnetic field intensities may suppress fluid flow excessively and result in grain coarsening [68]. Du et al. investigated static magnetic field-assisted directed energy deposition of IN718 superalloy and observed that increasing magnetic field intensity altered dendrite arm spacing and promoted the formation of long columnar grains with low-angle grain boundaries. The authors reported that magnetic fields affect solidification behavior through thermoelectric magnetic convection and damping effects, which significantly modify heat and mass transfer inside the molten pool [69].

Apart from improving microstructure and mechanical properties, magnetic fields also enhance surface quality and dimensional accuracy of additively manufactured components. Wu et al. investigated magnetic field-assisted finishing of selective laser melted SS316L parts and observed significant improvement in surface roughness due to controlled movement of magnetic abrasive particles along the build direction [63]. Similarly, Zhao et al. applied an alternating magnetic field during WAAM of Al–5Mg alloy and reported finer and more uniformly distributed grains together with improved tensile strength, hardness, and elongation [70]. These studies indicate that magnetic field-assisted AM can simultaneously improve both bulk material properties and surface characteristics of fabricated components.

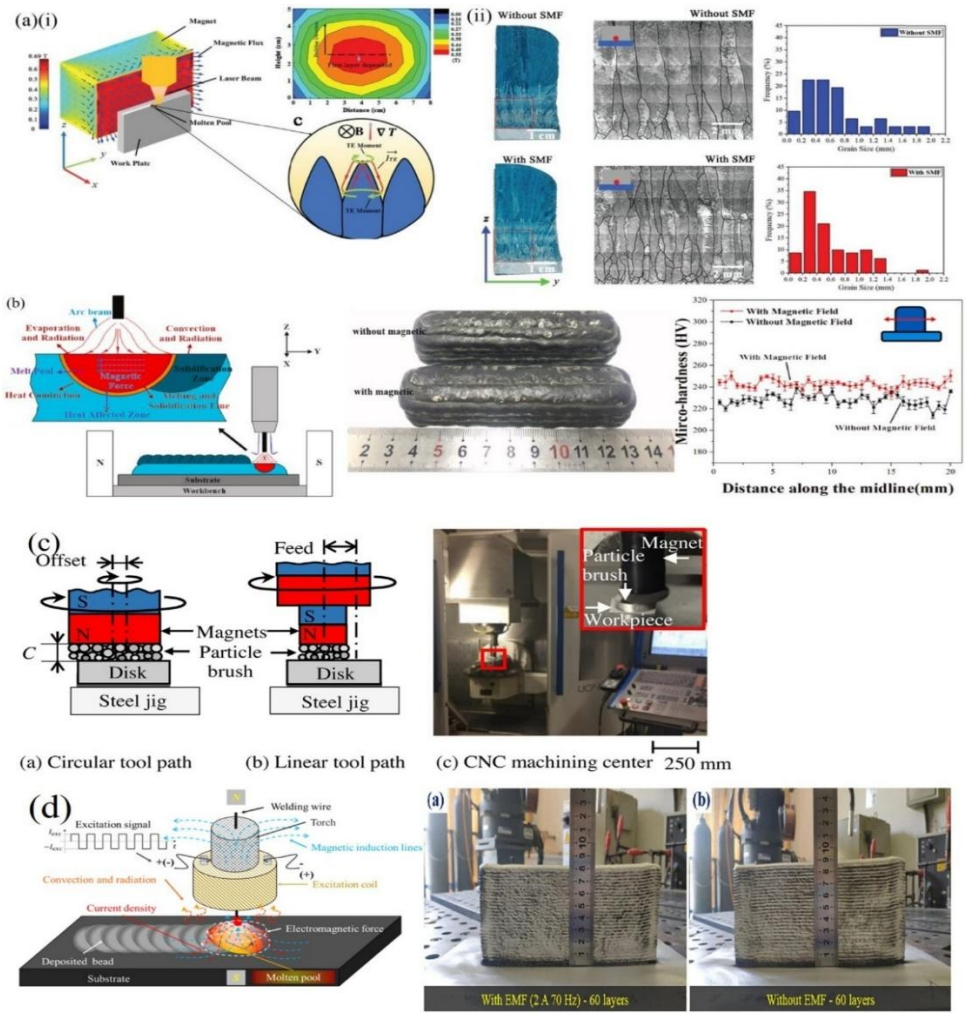


Fig 2.4: *(a) (i)Schematic showing the solidification process of L-DED under a 0.55 T transverse SMF, where the thermoelectric current, thermoelectric magnetic force are illustrated in the solidification front and also, distribution of magnetic field intensity. (ii) OM images; and β grains microscopy images; and Histograms of β grain size. (b) Schematic representation of WAAM deposition process and picture of deposited sample. Also, microhardness along the midline of the deposited Inconel 625 alloy without and with magnetic field . (c) MAF processing principles and equipment setup showing two different tool path setups. (d) The schematic diagram of WAAM process with EMF. Also, the macro-morphology of fabricated thin-wall parts with 60 layers: with EMF of 2 A 70 Hz and without EMF [Source].*

Although magnetic field-assisted additive manufacturing offers several advantages, certain challenges still remain. The integration of magnetic systems into existing AM equipment increases system complexity and cost. Additionally, excessive magnetic field intensity may

destabilize the arc or alter melt pool behavior unfavorably, leading to inconsistent deposition quality [69]. Precise control of magnetic field strength, orientation, and frequency is therefore essential to achieve optimal processing conditions. Moreover, further research is required to establish comprehensive relationships among magnetic field parameters, melt pool dynamics, microstructural evolution, and mechanical performance for different alloy systems [69].

Table 2.1: *Effect of Magnetic Field-Assisted and Additive Manufacturing Techniques on Microstructure and Mechanical Properties of Metallic Alloys*

Metal / Alloy	AM Technique	Property Improved
Ti-6Al-4V	L-DED	Improved mechanical properties, refined grain size, and reduced grain coarsening [63]
Inconel 625	Magnetic Field-Assisted EDM	Refined and more uniform microstructure with improved surface quality [70]
SS316L	LPBF	Formation of equiaxed grains, reduced dislocation density, improved ductility, and fewer cracks [64]
Fe–Cr Alloy on 45 Steel	Magnetic Field-Assisted Laser Cladding	Improved concentration mixing and homogeneous element distribution [71]
SS316L Stainless Steel	DED	Finer microstructure, smaller grain size, reduced porosity, increased hardness, and improved tensile strength [66]
Inconel 625 Superalloy	WAAM	Refined microstructure, reduced dendrite size, increased tensile strength, yield strength, and elongation [62].
SS316L	Magnetic Field-Assisted SLM Finishing	Improved surface finish and reduced surface roughness [68].
Al–5%Mg Alloy	WAAM with Alternating Magnetic Field	Finer and more uniform microstructure, higher tensile strength, elongation, and hardness [69].

In summary, magnetic field-assisted additive manufacturing has demonstrated significant potential for improving melt pool behavior, reducing porosity, refining microstructure, and enhancing mechanical properties in metallic components. Magnetic stirring and Lorentz-force-induced convection improve heat transfer and element distribution during solidification, leading to finer grain structures and improved material performance. These benefits are particularly

important for titanium alloys, stainless steels, and nickel-based superalloys used in aerospace and biomedical applications. Consequently, magnetic field-assisted additive manufacturing is emerging as an effective strategy for producing high-performance metallic components with improved structural integrity and reliability.

2.3 Advancements in Titanium Alloys for Orthopedic Implants with Antibacterial Properties

Increase in the accidents, sports injuries, and prevalence of degenerative diseases (i.e., osteoarthritis, osteoporosis, and rheumatoid arthritis) have significantly enhanced use of different types of implants such as knee implants, hip joints, and dental implants [69], [72]. Projections till 2030 indicate a substantial rise in revision surgeries for both hip (137%) and knee (607%) implants which highlighting critical need for durable and effective implant materials [73]. Since orthopaedic and dental implants remain inside the human body for a prolonged duration, implant materials should possess superior biocompatibility, non-cytotoxic behaviour, chemical stability, excellent corrosion resistance, low elastic modulus, and high mechanical strength [74].

Stainless steel, titanium alloys, Co-Cr-Mo alloys are the most commonly used implant materials [75], [76]. Among these, titanium alloys are highly favoured due to their outstanding biocompatibility, superior specific strength, and excellent corrosion resistance [76], [77]. Commercially pure titanium (CP-Ti) and Ti-6Al-4V are widely used Ti alloys. Of these, Ti-6Al-4V alloy is particularly popular due to its enhanced strength, corrosion resistance, and hardness as compared to CP-Ti [83-86]. But, release of toxic aluminium and vanadium ions by Ti-6Al-4V alloy leads to long-term health issues and cytotoxic effects, including neurological disorders and Alzheimer's disease [84, 86, 87]. Furthermore, mismatch between elastic modulus of titanium alloys (e.g., CP-Ti and Ti-6Al-4V having ~110 GPa) and human bone (10-30 GPa) leads to stress shielding effects, which causes bone resorption and implant failure [76], [78].

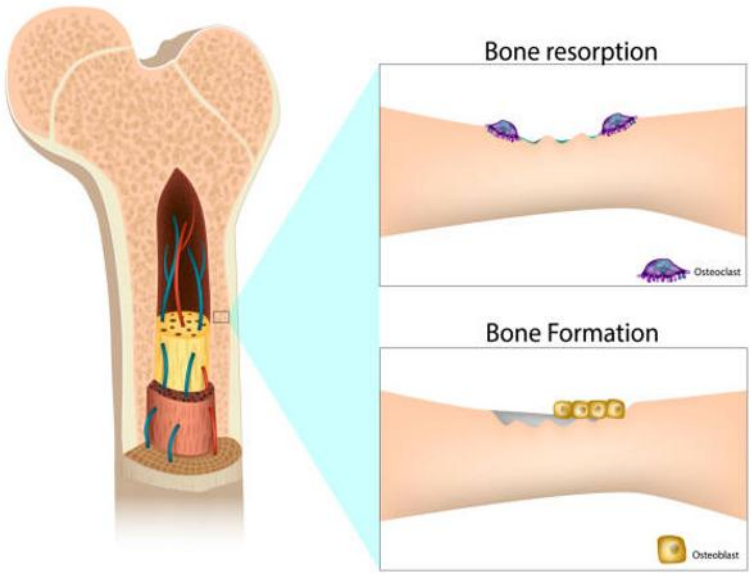


Fig 2.5: *Process Bone Formation and Resorption [Source]*

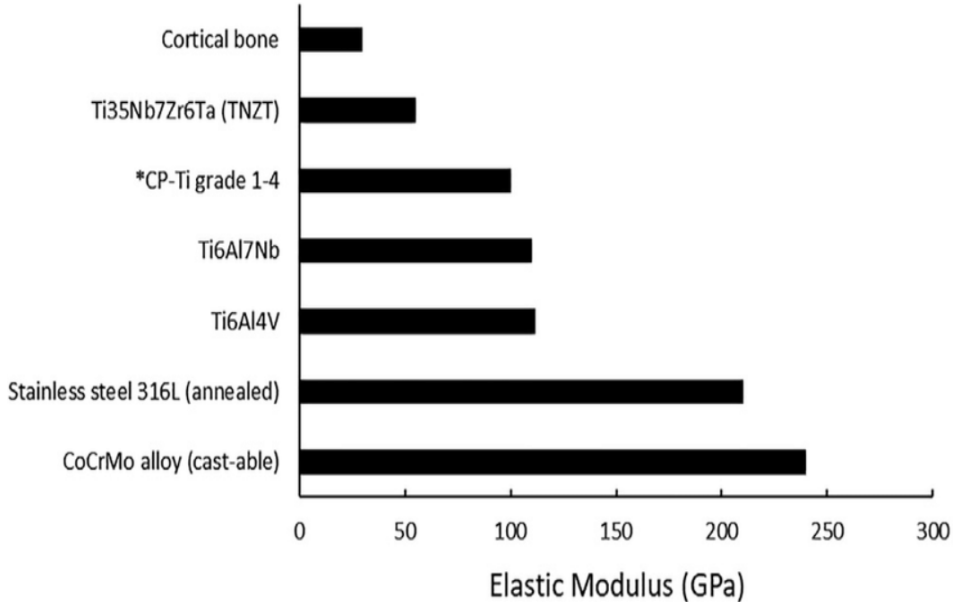


Fig 2.6: *Elastic modulus values of orthopedic alloys* ***[Source]***

In this context, β-Ti alloys having nontoxic and allergy-free alloying elements such as Nb, Zr, Mo, and Ta, seem to be promising implant material as they exhibit lower elastic modulus (55-85 GPa) thus reducing stress shielding effect and improving load transfer capacity of an implant [79]. Niobium is a critical β-stabilizing element that offers several advantages, including non-toxicity, excellent corrosion resistance, enhanced biocompatibility, and improved cell adhesion. Whereas, molybdenum is an even stronger beta-stabiliser, promoting

formation of a stable equiaxed β-phase, which enhances mechanical properties and corrosion resistance [42], [80], [81]. Therefore, researchers have developed different β-Ti alloys. Nmachi et *al.* developed β-Ti-8Mo-xNb-xZr alloys (with x = 2, 3, 4, 5 and 6 at.%) by arc melting process using tungsten electrode on a water-cooled copper hearth[82]. Their study found that addition of Nb and Zr alloying elements reduced elastic modulus of all the alloys and minimum elastic modulus of 35.4 GPa was achieved for Ti-8Mo-4Nb-2Zr alloy. Other such β-Ti alloys include Ti-24Nb-4Zr-8Sn, Ti-25Nb-3Zr-3Mo-2Sn, and Ti-15Zr-4Nb-4Ta-0.2Pd [82, 90] having superior biocompatibility, elastic modulus closer to human bones, and high mechanical strength and corrosion resistance.

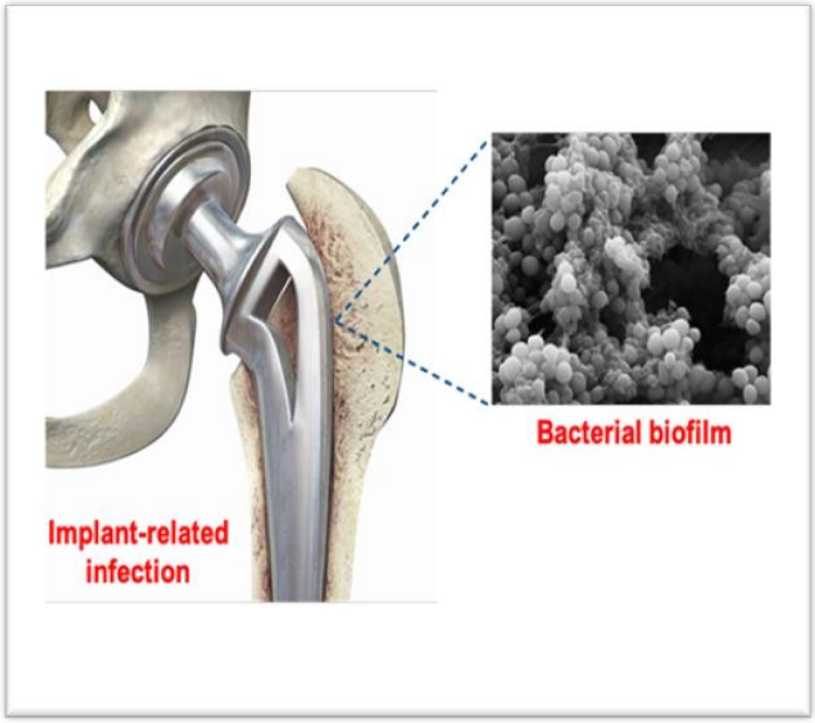


Fig 2.7: *Schematic representation for biofilm formation on titanium biomaterial [Source]*

Despite these developments, implant-related infections remain a significant clinical challenge, with reported infection rates reaching up to 20% in some orthopaedic procedures [83]. On average, 2-5% of implants are estimated to be contaminated, and the additional cost associated with managing each patient with an implant-related infection (i.e., treatment and surgical revision) is estimated at around 100,000 USD [84]. It has been reported that even if surgery is performed under strict aseptic conditions, average infection rate of Ti alloy orthopaedic implants is still 0.5%–5% [85]. In USA, 4.3% of the orthopaedic implants failed every year due to bacterial infections [86]. Infection incidences of total knee arthroplasty were

0.5-5% and total hip arthroplasty were 0.6-16% [87]. Copper has emerged as a promising alloying element for the orthopaedic and dental implants due to its antibacterial and biological functionalities. It is an essential trace element in the human body which can promote growth of endothelial cells, inhibit excessive proliferation of arterial smooth muscle, promote bone formation, and reduce thrombosis [88]. Antibacterial effect of Cu-containing β-Ti alloys primarily stems from controlled Cu ion release and from formation of Ti_2Cu precipitates within the microstructure thereby significantly enhancing its antibacterial performance [88]. It offers an optimal balance between high antibacterial efficiency, low cost, and relatively low cytotoxicity. Furthermore, addition of Cu can improve mechanical properties by increasing hardness and strength, although excessive amounts may reduce ductility [89].

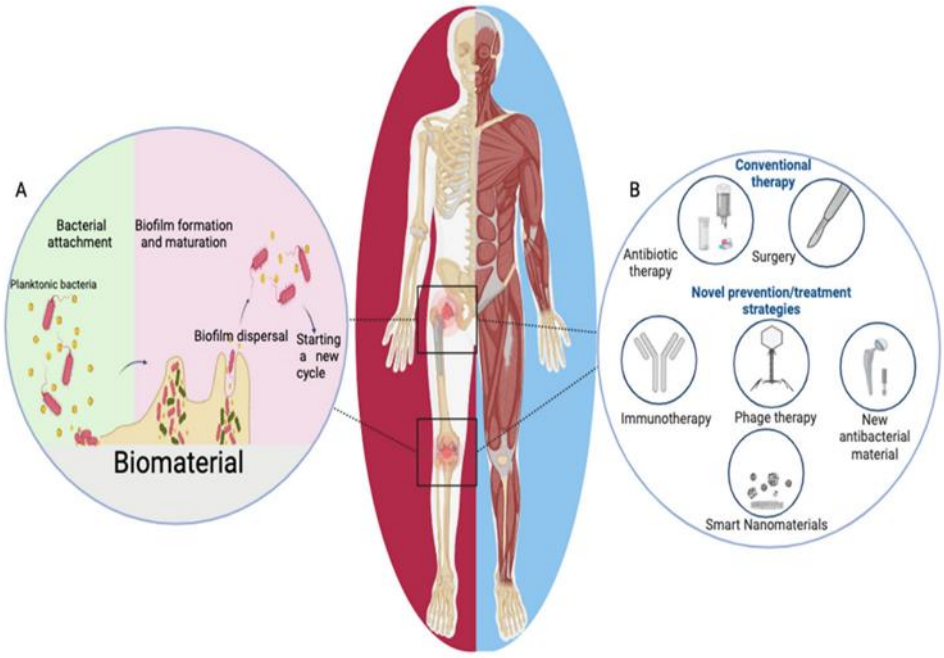


Figure 2.8: *(**A**) The process of biofilm formation (**B**) Conventional therapy and novel prevention or treatment strategies* [Source]

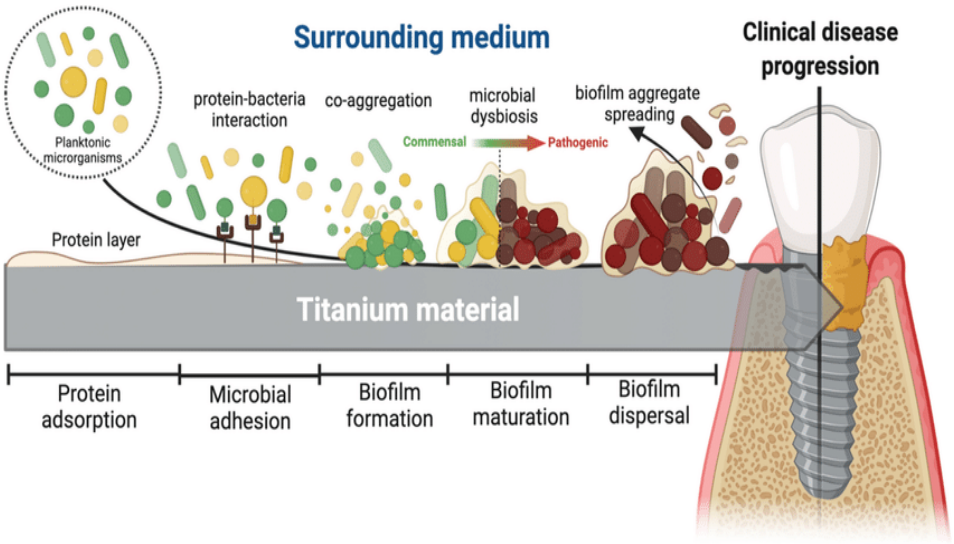


Fig 2.9: *Schematic representation for the steps of biofilm formation on titanium biomaterial. The schematic drawing depicts the five main steps for forming and spreading biofilms such as protein adsorption, microbial adhesion, biofilm formation, maturation, and dispersal. The clinical disease progression is dependent on biofilm accumulation [Source]*

Therefore, some researchers incorporated Cu in β-Ti alloys to achieve enhanced antibacterial performance along with improved biocompatibility and mechanical properties thereby addressing critical challenges in modern implantology. He et *al.* fabricated Ti-40Nb-xCu alloys (with x as 0, 2.5, 5, 7.5, and 10 wt.%) by spark plasma sintering process [90]. Their microstructure study showed formation of β-Ti as primary phase with intermetallic Ti_2Cu. Among different developed alloys, Ti-40Nb-5Cu alloy exhibited low elastic modulus thereby reducing stress shielding effect, high yield and compressive strength, and large plastic strain. Their antimicrobial study showed that increasing Cu content increased inhibitory response against *E. coli* and *S. aureus* bacteria than *C. albicans* fungi. Xu et *al.* developed Ti-10Mo-xCu alloys (with x as 0, 1, 3, and 5 wt.%) by the cold isostatic pressing and sintered them at different temperatures to study their cytocompatibility, bacterial inhibitory response, and mechanical properties [86]. Their study revealed that Ti-10Mo-3Cu alloy exhibited excellent cytocompatibility and bacterial inhibitory response, high strength, and good elongation.

2.4 Summary of the Literature Review

Following conclusions can be drawn from the review of the relevant past work described in the previous sections:

- Vacuum-assisted additive manufacturing significantly improves the quality of metallic components by reducing oxidation, contamination, and porosity during deposition, especially for reactive metals such as titanium alloys.
- Vacuum environments enhance melt pool stability, metallurgical bonding, density, corrosion resistance, fatigue strength, and overall mechanical performance in processes such as EBM, DED, and PAAM.
- Magnetic field-assisted additive manufacturing improves melt pool behavior through Lorentz-force-induced convection, resulting in grain refinement, reduced porosity, improved element distribution, and enhanced mechanical properties.
- Application of magnetic fields during additive manufacturing stabilizes plasma arc behavior, reduces powder spattering, improves surface finish, and enhances tensile strength, hardness, and ductility of metallic alloys.
- Conventional implant materials such as SS316L, Co–Cr alloys, CP-Ti, and Ti–6Al–4V suffer from limitations including stress shielding effect, toxic ion release, allergic reactions, poor antibacterial behavior, and implant-related infections.
- β-titanium alloys containing non-toxic alloying elements such as Nb, Mo, Zr, and Ta exhibit lower elastic modulus, superior corrosion resistance, improved cytocompatibility, and better osseointegration compared to conventional titanium alloys.
- Addition of copper (Cu) into β-titanium alloys provides excellent antibacterial properties along with improved hardness, strength, corrosion resistance, and biological performance due to controlled Cu ion release and Ti_2Cu precipitate formation.
- Previous studies mainly focused on conventional processing routes such as casting, sintering, and powder metallurgy for Ti–Mo–Nb–Cu alloys, while very limited work has been reported using additive manufacturing techniques, especially μ-PPAM
- Existing literature demonstrates significant advancements in vacuum-assisted and magnetic field-assisted additive manufacturing individually; however, research on their combined application in micro-plasma powder additive manufacturing (μ-PPAM) is extremely limited.
- No systematic study is available on μ-PPAM processing of Ti–9Mo–7Nb–xCu alloys for orthopaedic implant applications, particularly regarding their microstructure, phase evolution, antibacterial behaviour, biocompatibility, and mechanical properties.

- Therefore, further research is required to develop optimized μ-PPAM systems and investigate Ti–9Mo–7Nb–xCu biomedical alloys for next-generation orthopaedic implant applications.

2.5 Identified Research Gaps

Based on the detailed review of previous studies related to additive manufacturing, vacuum-assisted processing, magnetic field-assisted deposition, and titanium-based biomedical alloys, the following major research gaps have been identified:

1. **Lack of Research on Combined Vacuum and Magnetic Field-Assisted μ-PPAM:** Although vacuum-assisted additive manufacturing and magnetic field-assisted additive manufacturing have been independently investigated, very limited research is available on the simultaneous application of vacuum and magnetic fields in micro-plasma powder additive manufacturing (μ-PPAM). The combined influence of vacuum conditions and magnetic fields on melt pool behavior, powder flow characteristics, microstructural evolution, porosity reduction, and mechanical performance has not yet been systematically studied.
2. **Absence of Standardized Magnetic Field Design Parameters in μ-PPAM:** Existing studies on magnetic field-assisted additive manufacturing mainly focus on general process behavior, while very limited information is available regarding the optimized design of magnetic systems for μ-PPAM. Important parameters such as magnetic coil geometry, air gap distance, magnetic flux density, current input, and field orientation lack proper experimental validation and simulation-based optimization guidelines. Therefore, there is a need to establish standardized magnetic field design criteria for stable and efficient μ-PPAM processing.
3. **Limited Development of Ti–Mo–Nb–Cu Biomedical Alloys through Additive Manufacturing:** Previous studies have extensively investigated conventional implant materials such as SS316L, Ti–6Al–4V, Co–Cr alloys, and commercially pure titanium; however, these materials still suffer from several limitations including stress shielding effect, release of toxic ions, poor antibacterial behavior, and allergic reactions inside the human body. Although β-titanium alloys containing non-toxic alloying elements such as Mo, Nb, Zr, and Cu have shown promising biomedical characteristics, very limited research

has been reported on the design and additive manufacturing of Ti–9Mo–7Nb–xCu alloys, particularly in powder form.

4. **Insufficient Understanding of Microstructure–Property Relationships in µ-PPAM Processed Ti–9Mo–7Nb–xCu Alloys:** The effect of µ-PPAM process parameters on phase evolution, grain refinement, porosity formation, residual stresses, and mechanical behavior of Ti–9Mo–7Nb–xCu alloys has not been comprehensively investigated. Furthermore, the influence of vacuum and magnetic field-assisted deposition on β-phase stability, dendritic growth, hardness, tensile behavior, fracture characteristics, and corrosion resistance remains unclear.
5. **Lack of Comprehensive Biomedical Assessment of Additively Manufactured Ti–9Mo–7Nb–xCu Alloys:** Very limited literature is available on the biological and antibacterial performance of Ti–9Mo–7Nb–xCu alloys fabricated using µ-PPAM. Systematic investigations related to cytocompatibility, antibacterial activity, osseointegration potential, hemocompatibility, and in-vitro corrosion behavior are still lacking. Therefore, comprehensive evaluation of the biomedical suitability of these additively manufactured β-titanium alloys is essential for their application in next-generation orthopedic and dental implants.

2.6 Research Objectives (RO)

RO-1: Design and Development of a vacuum- and magnetically assisted µ-plasma powder additive manufacturing (VMA-µ-PPAM) system with controlled processing conditions to enable stable and precise metallic powder deposition.

RO-2: Design of Ti–zMo–yNb–xCu alloys and their multi-layer depositions by µ-plasma powder additive manufacturing (µ-PPAM) process using the optimum parametric combination identified through pilot and main experiments fabricating single-layer depositions

RO-3: Study of Microstructure and Mechanical Properties of the fabricated multi-layer deposition of Ti-9Mo-7Nb-xCu Alloys in terms of Porosity, Microhardness, Tensile test and its Fractography, Compressive strength, Fracture toughness, Scratch hardness

RO-4: *In-vitro* biocompatibility assessment using Cell viability, Cell adhesion, Bacterial Inhibition test, Release of metallic ions, and Corrosion behavior in the simulated biofluids

2.7 Research Methodology workflow

The research methodology followed in this study is presented in Figure 2.10. The work involves the development of a VMA-µPPAM system, design of Ti-based alloys using thermodynamic simulations, and optimization of deposition parameters through single-layer experiments. The identified optimum conditions were used for multi-layer fabrication of Ti-alloys. Finally, the fabricated samples were evaluated through microstructural, mechanical, and in vitro biocompatibility characterization to assess their suitability for biomedical applications.

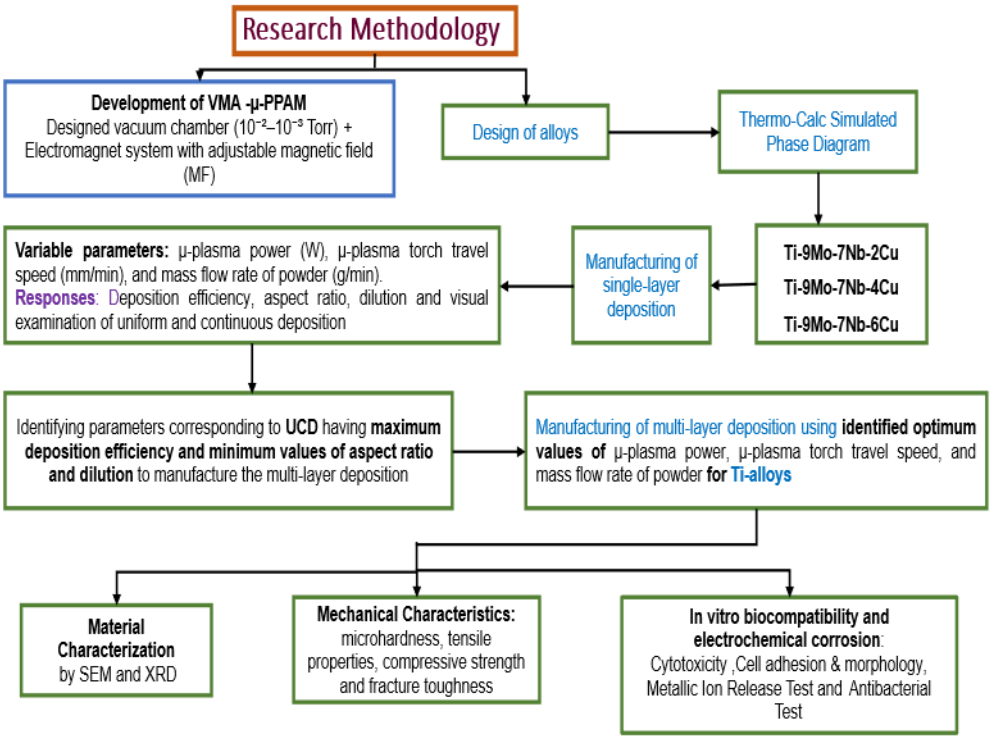


Figure 2.10: *Workflow of research methodology*

Chapter 3

Details of The Experiment

This chapter presents the details of the design of Ti–zMo–yNb–xCu alloys, preparation of the powders, and development of the machine used for the μ-PPAM process. It also describes the design and planning of experiments, along with the evaluation of various responses such as density, porosity, microstructure, phase analysis, mechanical properties, and in-vitro biocompatibility of μ-PPAM-fabricated Ti–9Mo–7Nb–xCu alloys. In addition, the chapter includes details of sample preparation and characterization procedures used for the investigation.

3.1 Development of Vacuum and Magnetically Assisted μ-PPAM System

This section describes the development and integration of the vacuum and magnetically assisted micro-Plasma Powder Additive Manufacturing (μ-PPAM) system used for the fabrication of Ti–9Mo–7Nb–xCu biomedical alloys. The developed setup consisted of a vacuum chamber, vacuum generation and monitoring units, powder feeding system, plasma torch, electromagnet assembly, and CNC-controlled deposition platform. The system was designed to provide a controlled low-pressure environment and magnetic assistance during deposition in order to improve powder flow behavior, molten pool stability, densification, and overall deposition quality.

3.1.1 Key Components of Vacuum and Magnetically Assisted μ-PPAM

The developed μ-PPAM setup consisted of several integrated subsystems including a vacuum pump, Pirani gauge, suction filtration unit, electromagnet, plasma torch, powder feeder, and CNC worktable. Fig. 3.1 shows the major components of the developed vacuum and magnetically assisted μ-PPAM system.

A two-stage rotary vacuum pump (Model: PVD2-250) having a free air displacement capacity of 250 LPM was used to evacuate the chamber and create the required low-pressure environment during deposition. The pump was capable of achieving an ultimate vacuum of approximately 0.005 mmHg at closed suction conditions. The vacuum environment minimized atmospheric contamination and oxidation during plasma deposition of titanium-based alloys.

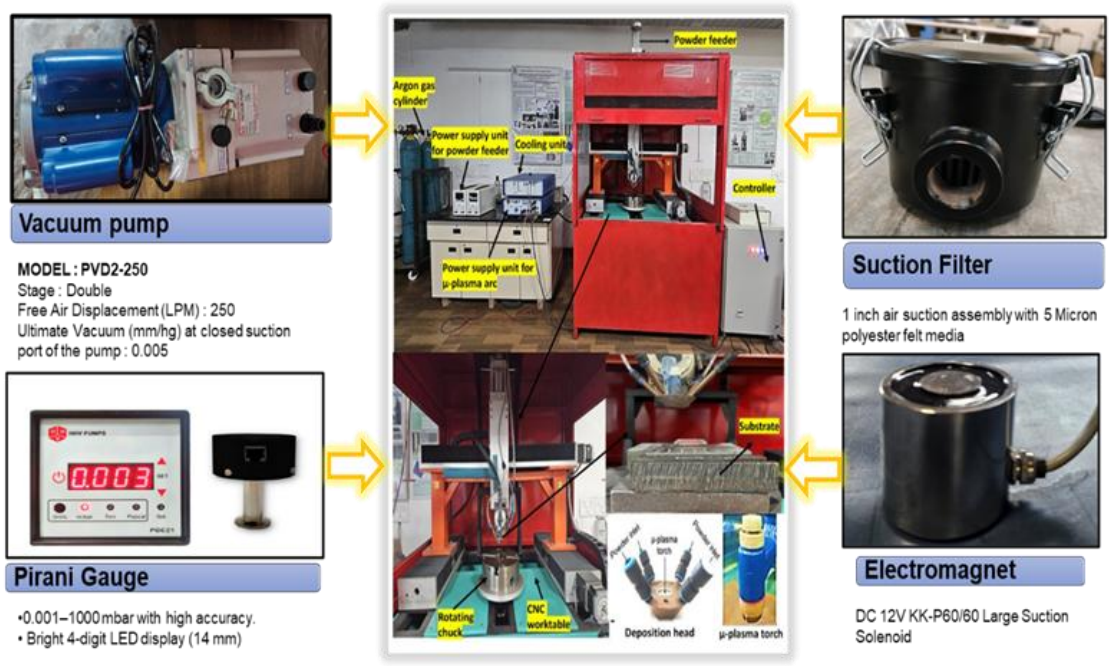


Fig 3.1: *Key Components of Vacuum and Magnetically Assisted µ-PPAM*

To continuously monitor the chamber pressure, a Pirani vacuum gauge having a measurement range of 0.001–1000 mbar was integrated into the system. The gauge provided high-accuracy pressure measurements through a bright four-digit LED display, enabling precise monitoring and control of the vacuum conditions throughout the deposition process.

A suction filter assembly containing a 5-micron polyester felt filter media was connected between the vacuum chamber and pump line. The filtration system prevented fine metallic powders and process contaminants from entering the vacuum pump, thereby protecting the pump components and improving operational reliability.

For magnetic assistance, a DC electromagnet (KK-P60/60 large suction solenoid) operating at 12 V DC was integrated below the deposition region. The electromagnet generated a controllable magnetic field during deposition, which assisted in powder confinement, stabilization of the molten pool, and improved deposition characteristics.

3.1.2 Development of Vacuum Chamber

A dedicated vacuum chamber was designed and fabricated for the vacuum-assisted µ-PPAM process. The chamber was developed to accommodate the complete deposition system including the CNC worktable, rotating chuck, plasma torch assembly, powder feeder, and

electromagnet setup. Fig. 3.2 presents the stages involved in the development of the vacuum chamber.

Initially, the μ-PPAM setup was operated under atmospheric conditions for system alignment, calibration, and preliminary deposition trials. After successful validation of the deposition system, a closed vacuum enclosure was designed and fabricated around the complete setup.

The fabricated chamber was made using rigid metallic structural sections capable of withstanding low-pressure operating conditions. Transparent viewing windows were provided on the front doors to enable process observation during deposition. Proper sealing arrangements were incorporated at all joints and access doors to minimize vacuum leakage during operation.



Fig 3.2: *Development of the Vacuum chamber*

Vacuum ports, electrical feedthroughs, gas inlet connections, and cooling line passages were integrated into the chamber design for proper functioning of the plasma torch, powder feeder, and electromagnet system. The chamber was connected to the vacuum pump through the suction filtration assembly to maintain the required pressure range during deposition.

The developed vacuum chamber enabled controlled deposition under reduced pressure conditions, thereby minimizing oxidation, improving arc stability, and enhancing the metallurgical quality of the deposited Ti-based alloys.

3.1.3 Electromagnet Setup and Magnetic Flux Density–Voltage Characterization

An electromagnet-assisted deposition arrangement was developed to study the influence of magnetic field application during the μ-PPAM process. The electromagnet was positioned beneath the deposition region in such a manner that the generated magnetic field interacted directly with the molten pool and powder stream during deposition.



Fig 3.3: *Electromagnet Setup*

A regulated DC power supply having an operating range of 0–24 V was used to energize the electromagnet. The magnetic flux density generated by the electromagnet was measured using a calibrated gaussmeter probe under controlled voltage conditions. Fig. 3.3 shows the experimental setup used for magnetic flux density measurements and the corresponding voltage–magnetic flux density relationship.

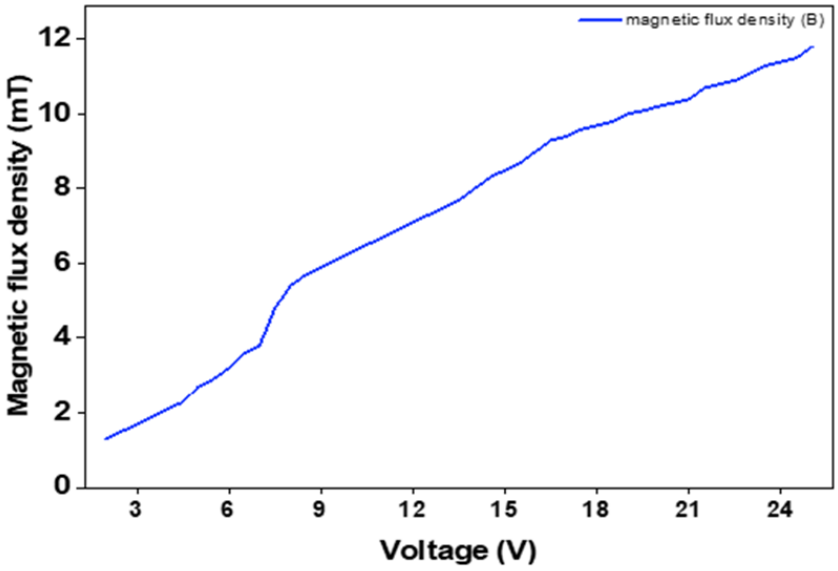


Fig 3.4: *Magnetic Flux Density–Voltage*

Fig. 3.4 shows The magnetic flux density increased progressively with increase in applied voltage. A nearly linear increase in magnetic field strength was observed within the operating

voltage range of approximately 3–12 V. At higher voltages, the magnetic flux density gradually approached saturation and reached a maximum value of approximately 11.5–12 mT.

The developed electromagnet system enabled controlled magnetic field application during deposition experiments. The magnetic assistance improved powder attraction and confinement near the deposition zone, enhanced molten pool stability, and contributed toward improved deposition quality and microstructural characteristics of the fabricated alloys.

3.2 Design of Alloy

Amount Mo and Nb to be included in Ti-zMo-yNb-xCu alloys was selected with an objective to maximize stabilization of β-Ti phase based upon the following findings: (i) Nmachi et *al.* used 8 at.% of Mo and varied Nb up to 6 at.% in Ti-8Mo-xNb-xZr alloys (with x = 2, 3, 4, 5 and 6 at.%) developed by arc melting [83], and (ii) Xu et *al.* developed Ti-10Mo-xNb by arc melting and graphite mould casting process used 10 wt.% Mo and varied Nb at 3; 7; and 10 wt.%. Accordingly [72], [91], Mo was selected as 9 wt% and Nb as 7 wt.% leading to development of β-Ti-9Mo-7Nb-xCu alloys. Upper limit of Cu can be added to Ti-9Mo-7Nb-xCu alloy was determined using Thermo-Calc simulated phase diagram shown in Fig. 3.5(a) which depicts occurrence of different phases with temperature and increasing wt.% of Cu. It can be observed from Fig. 3.5(a) that the Ti-9Mo-7Nb-xCu alloys predominantly stabilises the β-Ti phase having body centred cubic (BCC) crystal structure (i.e., BCC_B2 phase) over a wide temperature range due to presence of Mo and Nb which are β-stabilizing elements. Formation of intermetallic compounds (IMC) such as Ti_2Cu and $MoSi_2$ begins beyond 6 wt.% of Cu due to their limited solubility in β-Ti matrix. These IMC increase brittleness of Ti-9Mo-7Nb-xCu alloys. Therefore, Cu addition in the present study was limited to 6 wt.% to avoid the excessive formation of the brittle IMC. This decision is consistent with the findings of Zhang et *al.*, who reported that addition of Cu beyond 6 wt.% has significantly increased formation of Ti_2Cu IMC which led to embrittlement and reduced cell viability of osteoblast cells due to higher release of metallic ions [91]. It is also evident from the phase diagram that the β-phase regions within 6 wt.% of Cu remain stable which may be beneficial to achieve low elastic modulus and improved mechanical properties of Ti-9Mo-7Nb-xCu alloys.

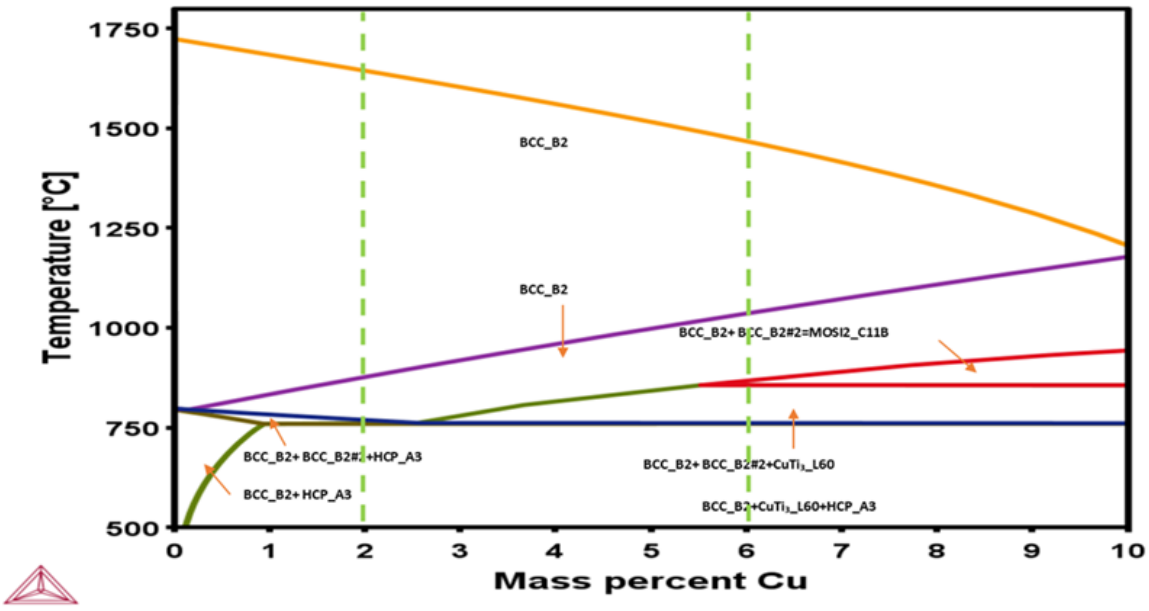


Fig 3.5(a): *Thermo-calc simulated phase diagram for deciding upper limit of Cu addition to Ti-9Mo-7Nb-xCu alloy.*

Fig 3.5(b) shows Scheil solidification diagram for Ti-9Mo-7Nb-xCu alloys depicting variation of temperature with its mole fraction during non-equilibrium solidification. Black coloured dotted line corresponds to the equilibrium solidification path while red coloured solid line represents the non-equilibrium solidification condition involving formation of β-Ti phase (BCC_B2) phase from the liquid phase. It can be seen from Fig. 2 that at the beginning of solidification (mole fraction ~ 0), both equilibrium and non-equilibrium curves start nearly from the same temperature i.e., ~1940 °C indicating initial liquidus temperature of Ti-9Mo-7Nb-xCu alloys. As the solidification progresses, the equilibrium curve shows a gradual decrease in temperature suggesting stable solidification under equilibrium conditions. Whereas, non-equilibrium curve involving LIQUID and BCC_B2 phases exhibits a steeper reduction in temperature with increasing mole fraction of the solid. This behaviour indicates pronounced solute redistribution and segregation during the rapid solidification. The widening gap between the equilibrium and non-equilibrium curves suggests increasing constitutional undercooling and deviation from equilibrium conditions. Temperature for red coloured curve decreases continuously from nearly 1800°C to 1650°C for the mole fraction values from 0.2 to 0.8 indicating progressive formation of β-Ti phase along with the residual liquid. The extended solidification interval implies a significant partitioning of the alloying elements during the

solidification. Near the final stage of solidification (i.e., mole fraction > 0.9), temperature of the red coloured curve drops sharply to ~1410°C. This sudden decrease indicates final solidification of the remaining solute-enriched liquid which is commonly associated with severe micro-segregation and possible formation of secondary or brittle IMC. Overall, the simulation indicates that Ti-9Mo-7Nb-xCu alloys undergo a broad non-equilibrium solidification range with significant segregation effects, while the equilibrium solidification predicts a comparatively stable and narrow solidification behaviour. Presence of β-Ti phase during solidification suggests that Ti-9Mo-7Nb-xCu alloys composition and cooling conditions strongly influence the phase evolution and microstructural stability.

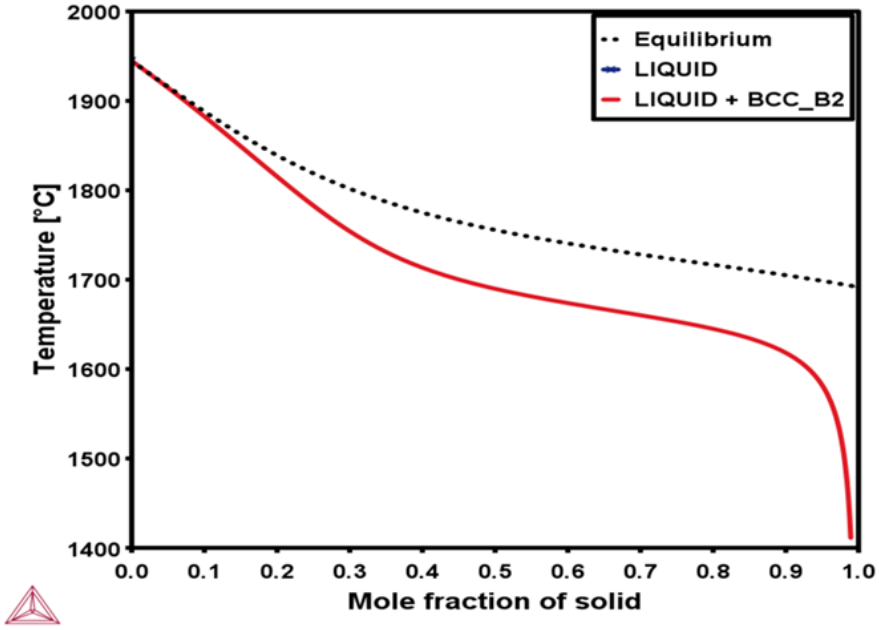


Fig 3.5(b): *Scheil solidification diagram of Ti-9Mo-7Nb-xCu alloy*

3.3 Powder preparation

Elemental powders of titanium (Ti), molybdenum (Mo), niobium (Nb), and copper (Cu) having a purity of 99.9% and particle size ranging from 45–105 μm were used for the preparation of Ti–9Mo–7Nb–xCu alloy powders. The powders were procured from Orion Chemicals Pvt. Ltd., Pune, India. Titanium was selected as the base metal due to its excellent biocompatibility, corrosion resistance, and favorable strength-to-weight ratio for biomedical implant applications. Mo and Nb were used as β-phase stabilizers to improve the mechanical properties and reduce the elastic modulus of titanium alloys, whereas Cu was added to enhance antibacterial behavior, hardness, and wear resistance.

The chemical compositions of the designed alloys are presented in Table 3.1. Three different alloy compositions containing 2 wt.%, 4 wt.%, and 6 wt.% Cu were prepared while maintaining Mo and Nb contents constant at 9 wt.% and 7 wt.% respectively. The composition range was selected to study the effect of Cu addition on the microstructure, phase evolution, mechanical properties, and biological performance of the developed alloys.

The required quantity of each elemental powder was weighed accurately using a precision electronic weighing balance according to the compositions listed in Table 3.1. The weighed powders were then blended using a planetary ball milling machine (Model: STC-XQM-0.4A, Tico, Shenzhen, China). Mixing was carried out for 3 hours at a rotational speed of 350 rpm using tungsten carbide balls of 6 mm diameter. A ball-to-powder weight ratio (BPR) of 2:1 was maintained during the milling process to ensure effective blending and homogeneous distribution of alloying elements throughout the powder mixture.

Planetary ball milling was adopted to improve particle interaction and achieve uniform dispersion of Mo, Nb, and Cu particles within the Ti matrix. The milling process also helped in reducing powder agglomeration and improving compositional homogeneity, which is essential for obtaining defect-free and compositionally uniform deposits during the μ-PPAM process.
After completion of the milling operation, the prepared powders were de-moisturized in a furnace at 100°C for 30 minutes prior to deposition. This step was necessary to remove absorbed moisture and volatile contaminants from the powder surfaces, thereby minimizing oxidation, porosity formation, and instability during plasma deposition.

Fig. 3.6 presents the scanning electron microscopy (SEM) images of the as-received Ti, Mo, Nb, and Cu powders. The Ti powder particles exhibited predominantly irregular and angular morphology, while Mo and Nb powders showed comparatively finer and sharper particle structures. Cu powder particles displayed relatively smoother surfaces and irregular shapes. The morphology and particle size distribution of the powders significantly influence powder flowability, melting behavior, and deposition quality during additive manufacturing.

Fig. 3.7, 3.8, and 3.9 show the detailed characterization of the prepared Ti–9Mo–7Nb–2Cu, Ti–9Mo–7Nb–4Cu, and Ti–9Mo–7Nb–6Cu alloy powders respectively. These figures include SEM morphology, energy dispersive spectroscopy (EDS) analysis, particle size measurements, and elemental mapping results. The SEM images confirmed the homogeneous mixing of

alloying elements after ball milling. EDS analysis verified the presence of Ti, Mo, Nb, and Cu elements in compositions close to the designed alloy chemistry.

Table 3.1: *Chemical compositions of the designed Ti-Mo-Nb-xCu alloys by wt.%.*

Alloy type	Ti	Mo	Nb	Cu
Ti-9Mo-7Nb-2Cu	82	9	7	2
Ti-9Mo-7Nb-4Cu	80	9	7	4
Ti-9Mo-7Nb-6Cu	78	9	7	6

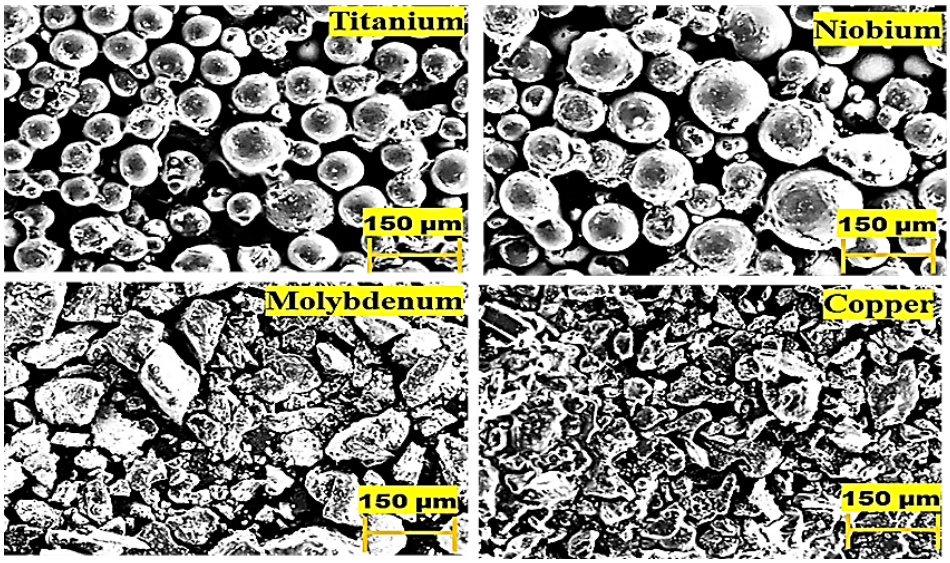
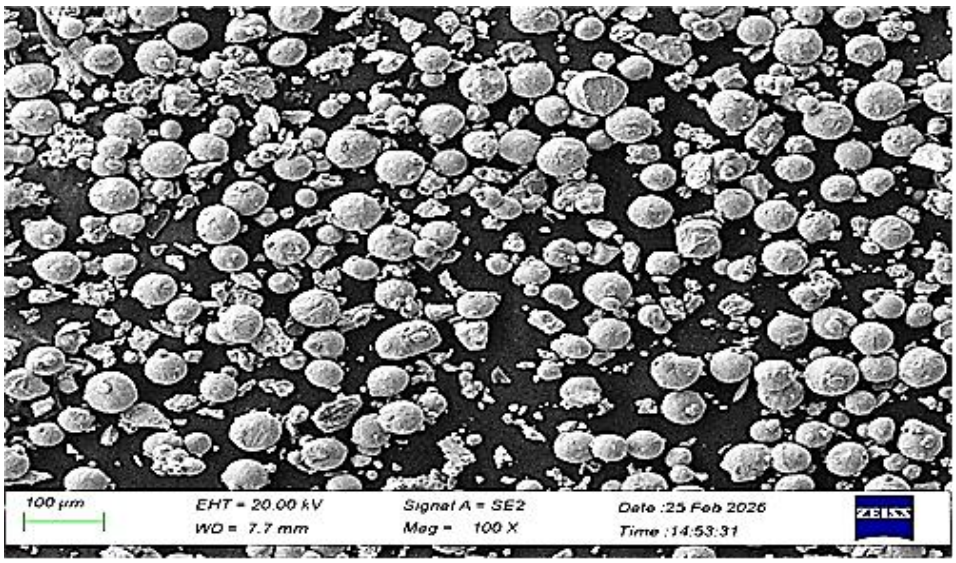
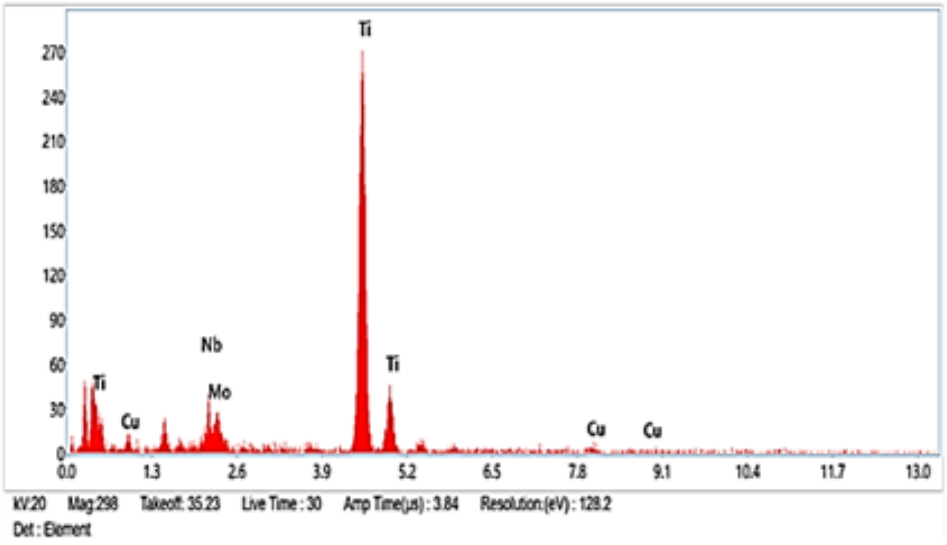


Fig 3.6: *Morphology of as-received powders of Ti, Nb, Mo, and Cu.*


100 µm
EHT = 20.00 kV
WD = 7.7 mm
Signal A = SE2
Mag = 100 X
Date :25 Feb 2026
Time :14:53:31
ZEISS


Ti
Nb
Mo
Ti
Ti
Cu
Cu
Cu
270
240
210
180
150
120
90
60
30
0
0.0
1.3
2.6
3.9
5.2
6.5
7.8
9.1
10.4
11.7
13.0
kV:20 Mag:298 Takeoff: 35.23 Live Time : 30 Amp Time(µs) : 3.84 Resolution:(eV) : 128.2
Det : Element

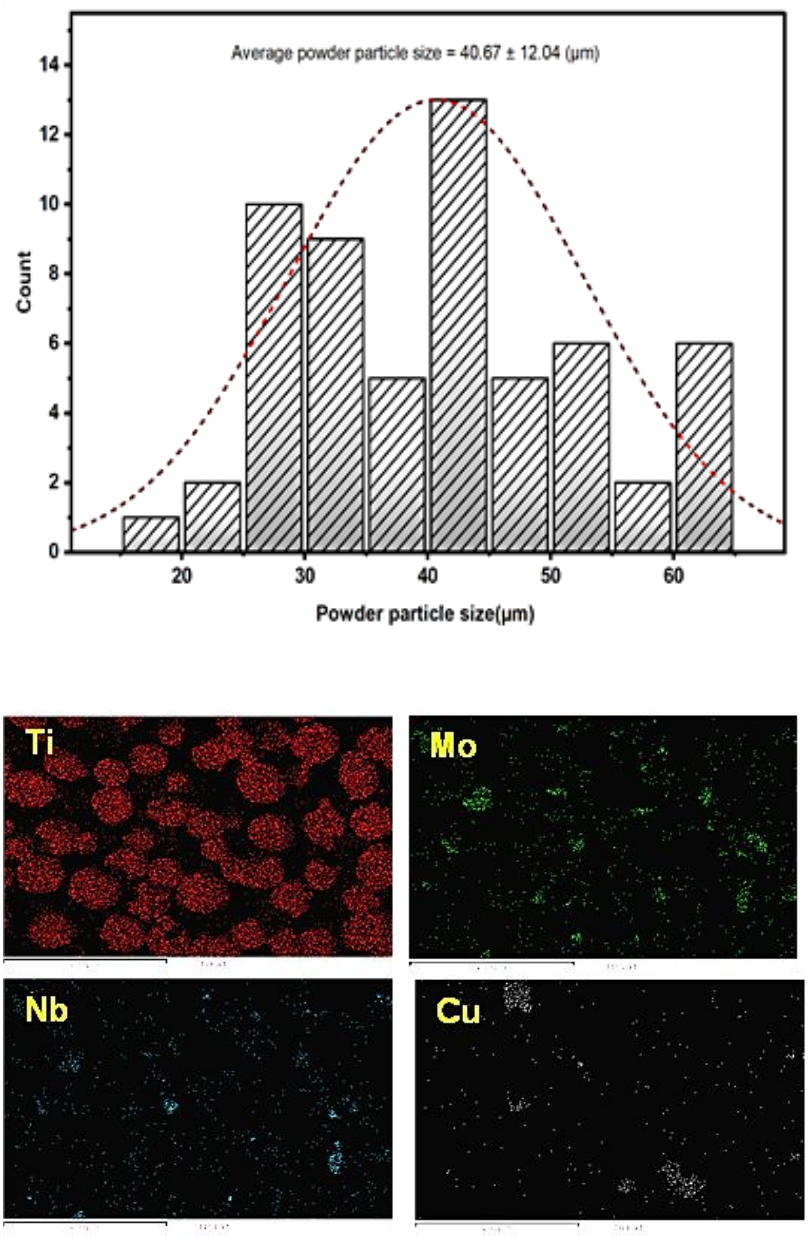
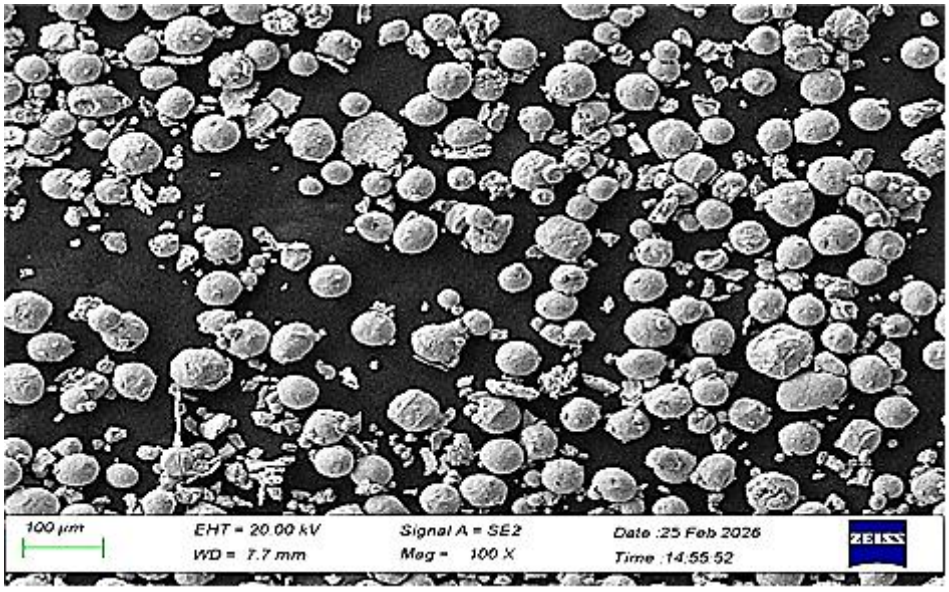
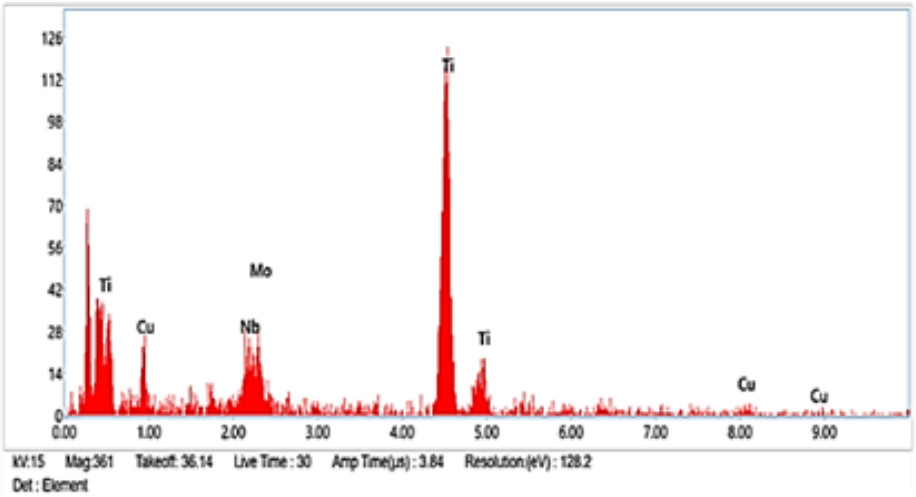


Fig 3.7: *Morphology, chemical composition, average size of powder particles, and elemental mapping for the prepared powder of Ti-9Mo-7Nb-2Cu alloy.*


100 µm
EHT = 20.00 kV
WD = 7.7 mm
Signal A = SE2
Mag = 100 X
Date :25 Feb 2026
Time :14:55:52
ZEISS


126
112
98
84
70
56
42
28
14
0
Ti
Cu
Mo
Nb
Ti
Ti
Cu
Cu
0.00
1.00
2.00
3.00
4.00
5.00
6.00
7.00
8.00
9.00
kV:15 Mag:361 Takeoff: 36.14 Live Time : 30 Amp Time(µs) : 3.84 Resolution(eV) : 128.2
Det : Element

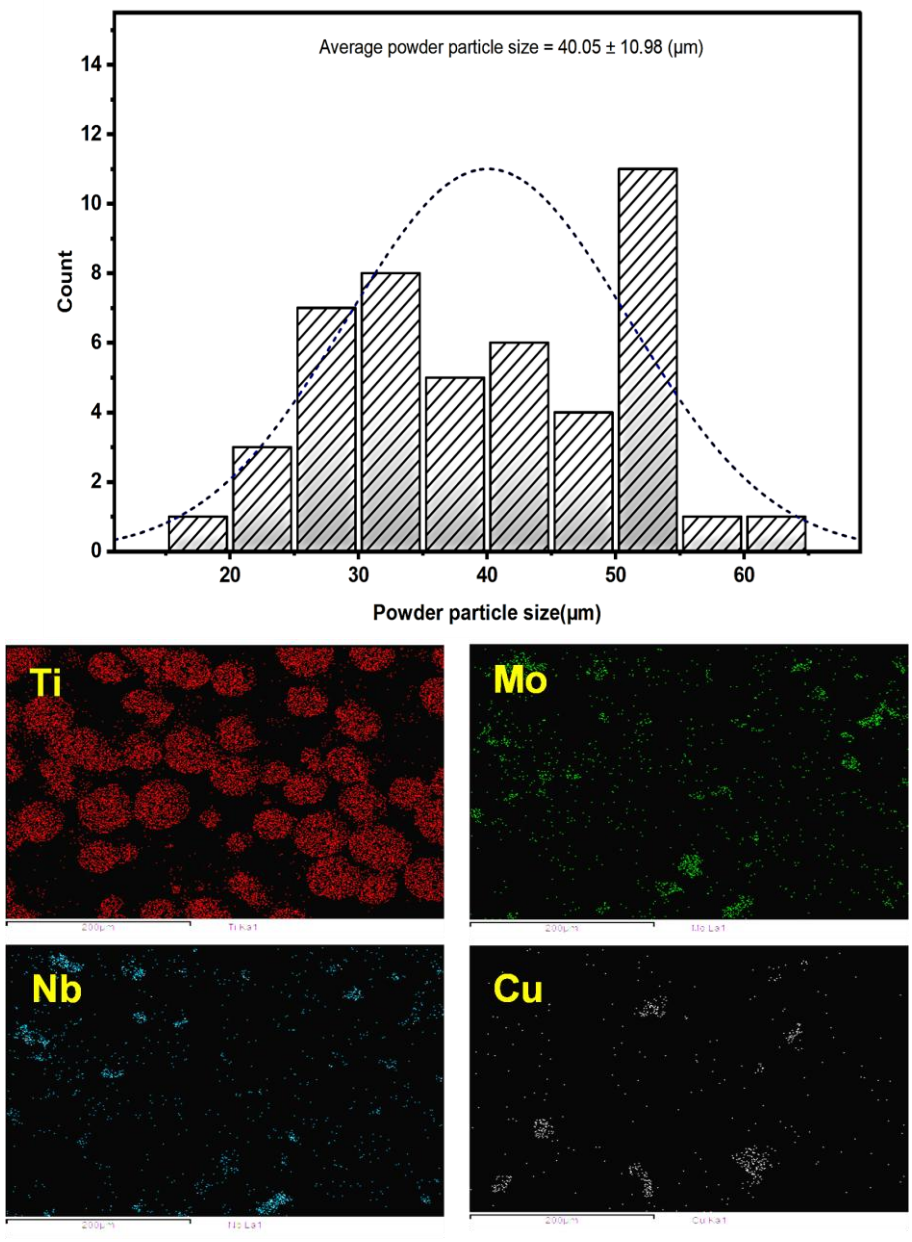
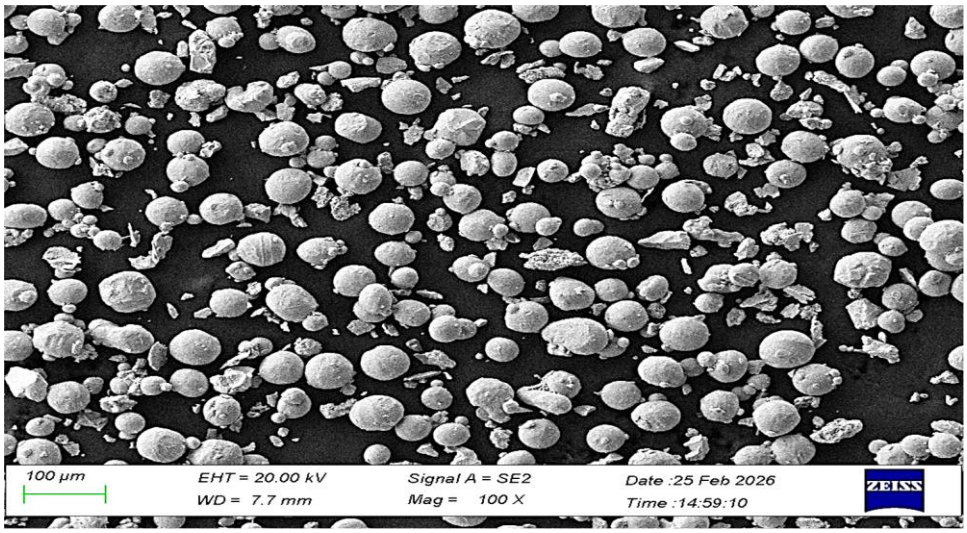
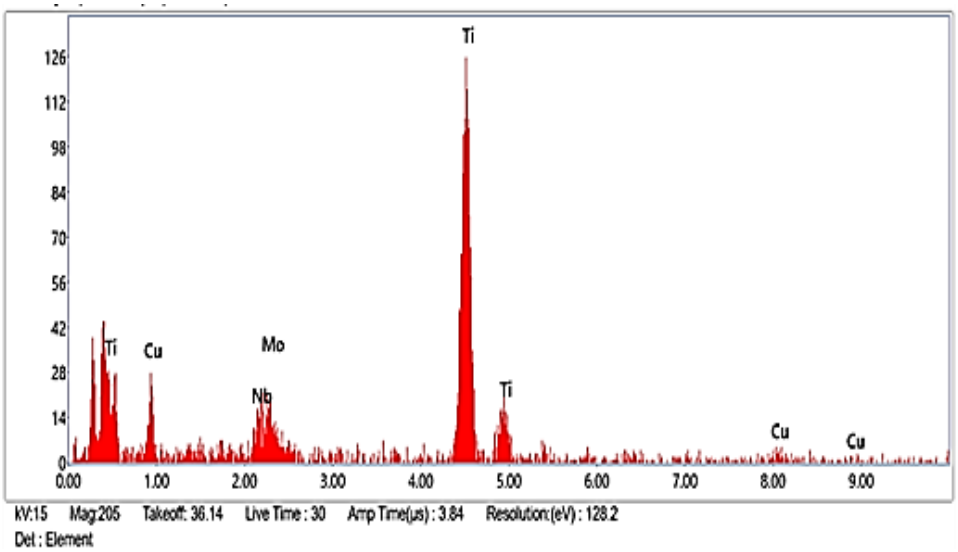


Fig 3.8: *Morphology, chemical composition, average size of powder particles, and elemental mapping for the prepared powder of Ti-9Mo-7Nb-4Cu alloy.*


100 µm
EHT = 20.00 kV
WD = 7.7 mm
Signal A = SE2
Mag = 100 X
Date :25 Feb 2026
Time :14:59:10
ZEISS


Ti
Ti
Cu
Mo
Nb
Ti
Cu
Cu
126
112
98
84
70
56
42
28
14
0
0.00
1.00
2.00
3.00
4.00
5.00
6.00
7.00
8.00
9.00
KV:15 Mag:205 Takeoff: 36.14 Live Time : 30 Amp Time(µs) : 3.84 Resolution:(eV) : 128.2
Det : Element

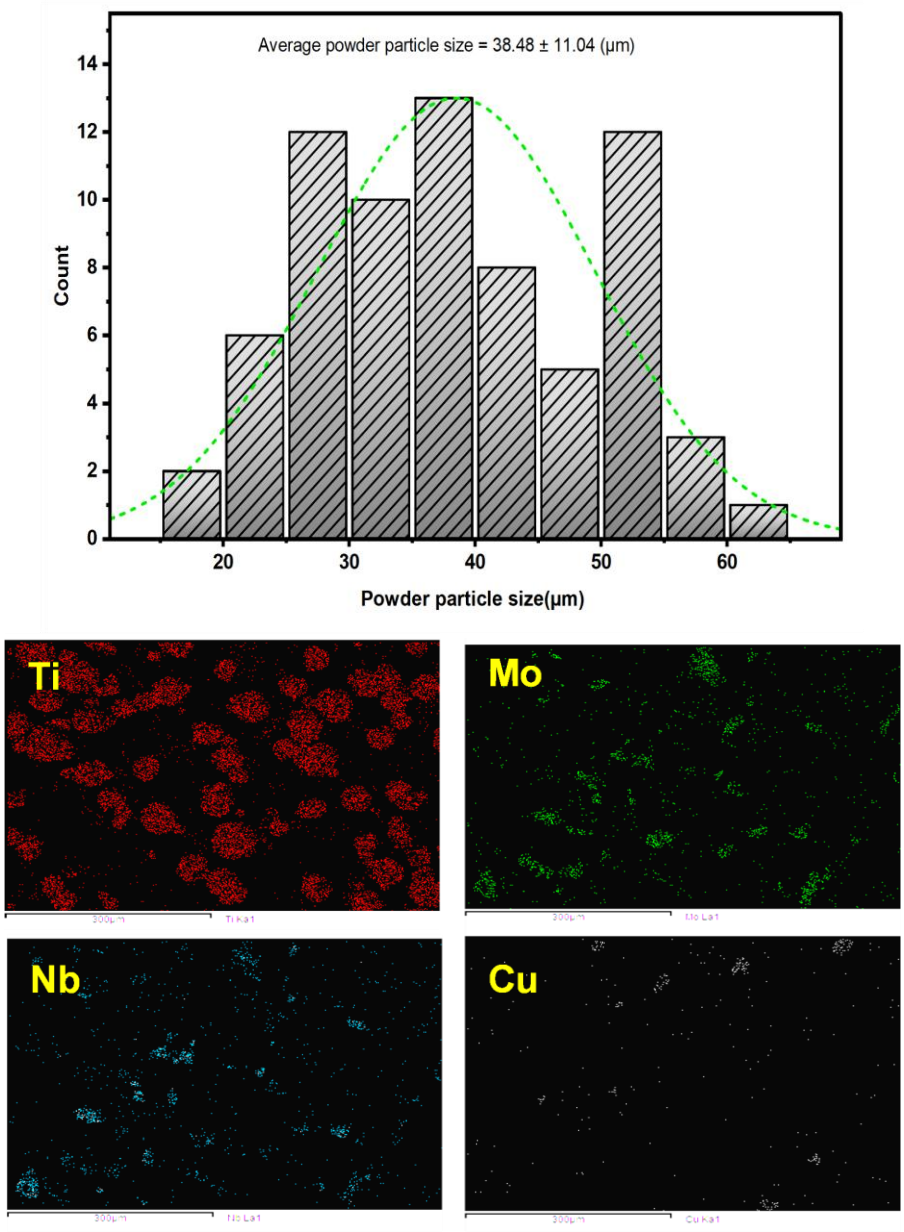
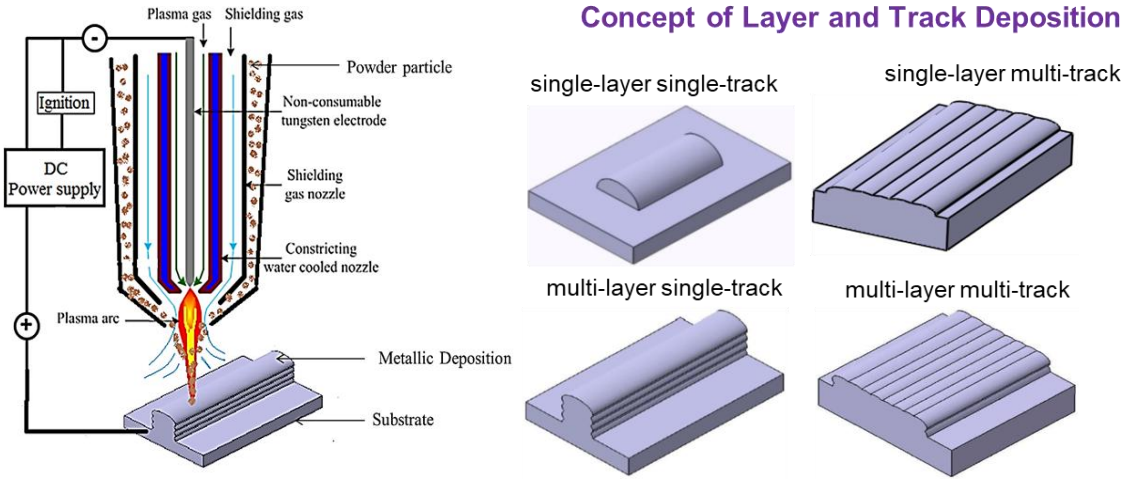


Fig 3.9: *Morphology, chemical composition, average size of powder particles, and elemental mapping for the prepared powder of Ti-9Mo-7Nb-6Cu alloy.*

3.4 Apparatus for µ-PPAM Process

Experiments were carried out using a developed 5-axis CNC-based micro-Plasma Powder Additive Manufacturing (µ-PPAM) machine, as shown in Fig. 3.11. The setup consisted of a CNC-controlled worktable, µ-plasma torch, powder feeding system, argon gas supply system, cooling unit, controller unit, vacuum chamber, and electromagnet-assisted deposition arrangement. The developed machine was used for fabrication of Ti–9Mo–7Nb–xCu biomedical alloys under controlled deposition conditions.

The working principle of the µ-PPAM process is shown in Fig. 3.10(a). A direct current (DC) power supply was used to ionize the plasma-forming gas and generate a stable µ-plasma arc between the non-consumable tungsten electrode and the substrate. The generated plasma arc acted as a concentrated heat source to melt the feedstock powder and fuse it with the substrate or previously deposited layer. Argon gas was used as both plasma-forming and shielding gas to protect the molten deposition zone from atmospheric contamination and oxidation. Fig. 3.10(b) presents different deposition strategies possible in the µ-PPAM process such as single-layer single-track, single-layer multi-track, multi-layer single-track, and multi-layer multi-track depositions.



(a) (b)

Fig 3.10: *(a) Represents the working principle of the µ-PPAM process, while (b) shows different deposition tracks possible using the µ-PPAM technique.*

The developed μ-PPAM machine consisted of five major units:

(i) CNC worktable,

(ii) μ-plasma power supply unit,

(iii) powder feeding system,

(iv) gas supply and cooling system, and

(v) deposition head assembly.

The deposition head consisted of a μ-plasma torch at the center surrounded by inclined powder inlet nozzles for uniform powder delivery into the molten pool.

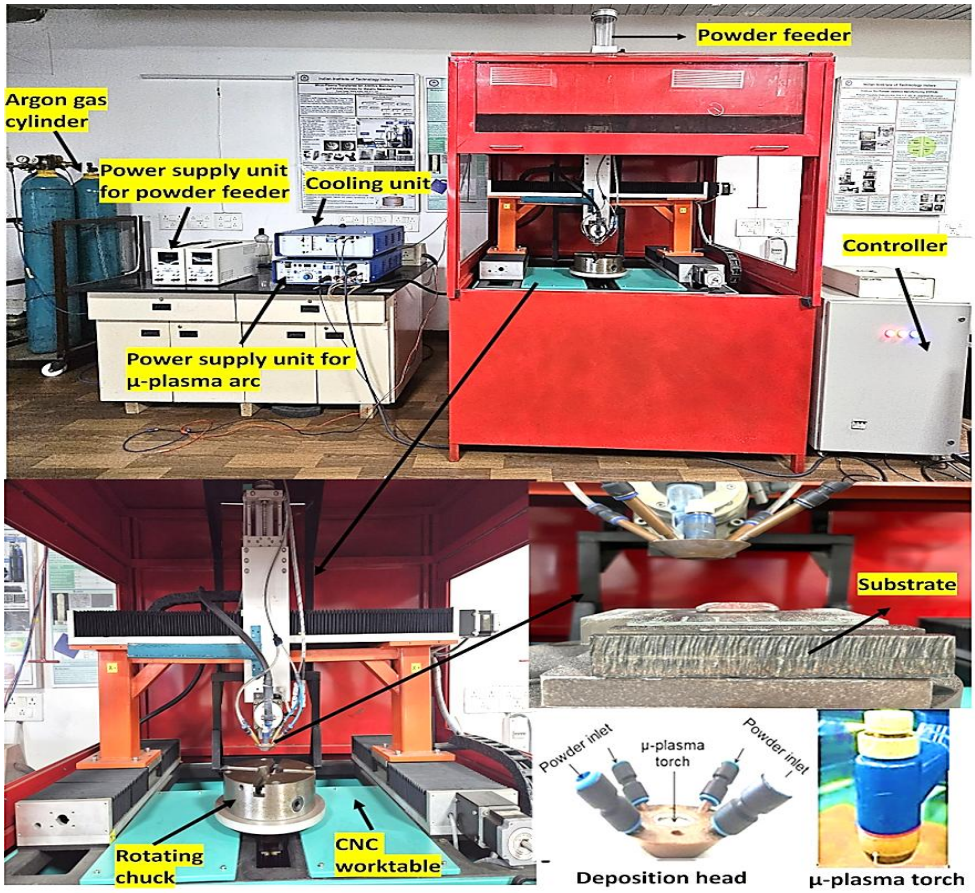


Fig 3.11: *Photograph of the developed 5-axis CNC μ-PPAM machine.*

The experiments were conducted in two stages, namely pilot experiments and main experiments. Initially, pilot experiments were performed using a one-factor-at-a-time (OFAT) approach to identify suitable operating ranges of important μ-PPAM process parameters. Single-layer depositions of Ti–9Mo–7Nb–4Cu alloy were fabricated on Ti substrate plates of dimensions 120 mm × 120 mm × 10 mm. Before deposition, the substrate surface was polished using SiC emery paper followed by acetone cleaning to remove contaminants and oxide layers.

The pilot experiments were conducted by varying six important parameters, namely µ-plasma power (110–440 W), powder mass flow rate (0.6–5.0 g/min), deposition head travel speed (40–200 mm/min), plasma-forming gas flow rate (0.1–0.5 NL/min), shielding gas flow rate (3–8 NL/min), and stand-off distance (3–15 mm). Based on the pilot experiments, optimized parameters for the main experiments were identified as µ-plasma power of 385, 396, and 407 W; powder mass flow rate of 2.7, 3.0, and 3.3 g/min; and deposition head travel speed of 42, 44, and 46 mm/min. The plasma-forming gas flow rate, shielding gas flow rate, and stand-off distance were maintained constant at 0.5 NL/min, 5 NL/min, and 9 mm respectively during deposition experiments.

Table 3.2: *Value of µ-PPAM process parameters, and design of experiments approach used in different phases of experiments.*

Parameters	Range available on µ-PPAM machine	Range used in 30 pilot experiments	Values Identified for 27 main experiments
Design of Experiments Approach	-	One-factor-at-a time	Full factorial
Number of Experiments	-	30	27
µ-Plasma Power (W)	1-440	270-430	385, 396, 407
Feedstock Powder Flow Rate (g/min)	0.1-15	0.9-5	2.7, 3, 3.3
Deposition Head Travel Speed (mm/min)	10-200	25-180	42, 44, 46
Plasma Formation Gas Flow Rate (Normal liter/min i.e., Nl/min)	0.1-0.8	0.1-0.5	0.5
Shielding Gas Flow Rate (Nl/min)	1-12	3-10	5
Stand-off distance (mm)	1-20	3-15	9

3.5 Study of single-layer depositions

Single-layer single-track depositions of Ti-9Mo-7Nb-4Cu alloy were fabricated using a μ-PPAM machine for each parameter combination to evaluate its deposition quality. The quality of each deposited track was initially assessed based on bead continuity, surface uniformity, and absence of visible defects such as discontinuities or excessive spreading. Then, the single-layer deposited samples were cut perpendicular to the deposition direction using the Wire Electric Discharge Machining (WEDM) process for cross-sectional sample analysis (shown in Fig. 3.12). Then, the cut samples were hot-mounted and polished up to 2500 grit size using SiC emery papers. The deposition width *'w'*, deposition height *'h'*, and dilution depth *'D_d'* were measured using a stereo zoom microscope (model: *Macscope-Z*, Chennai Metco, India). These images were further quantified through image analysis using AutoCAD/ImageJ software to compute the deposition area *'A_D'* and diluted area *'A_d'*. Aspect ratio (AR) was measured as the ratio of its *'w'* to *'h'*, to assess bead shape stability and spreading behaviour of the deposited layer.

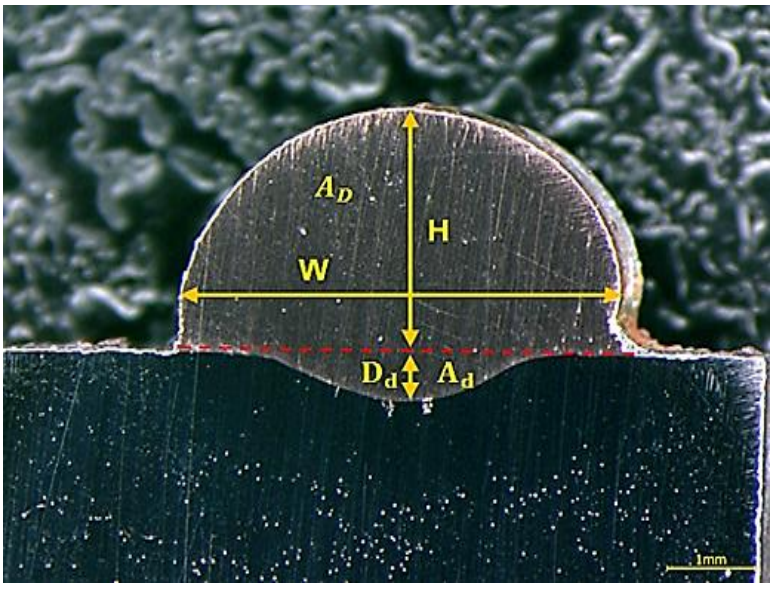


Fig 3.12: *Optical microscopic images of the cross-sectional area of a single layer of Ti-9Mo-7Nb-4Cu alloy.*

Dilution *'D'* is the ratio of diluted area *'A_d'* to the summation of diluted area *'A_d'* and deposition area *'A_D'*. It measures the amount of the feedstock material mixed with the base plate material. It is an important parameter, and a value more than 10 % is unfavourable because it

reduces deposition quality and increases thermal distortion and residual stress. Dilution percentage (D) was calculated using Eq. 1.

$$D = \frac{A_d}{A_D + A_d} \times 100 \quad (1)$$

The deposition efficiency (η) was evaluated using Eq. 2.

$$\eta = \frac{A_D \times S \times \rho_p}{F} \times 100 \quad (2)$$

where *'S'* is the deposition head travel speed (mm/min), *'F'* is the powder mass flow rate (g/min), and *'ρ_p'* is the density of the feedstock powder (g/mm³). Higher deposition efficiency indicates improved effective material utilisation and stable deposition. The optimised parameters obtained were identified based on achieving continuous and defect-free deposition with maximum deposition efficiency, minimum dilution, and desirable bead geometry before multilayer deposition of Ti-9Mo-7Nb-4Cu alloy.

3.6 Characterization of multi-layer depositions

Parametric combination that produced Uniform and Continuous Single-layer Deposition having Minimum Values of dilution and Aspect Ratio, and Maximum Deposition Efficiency, was identified as Optimum combination to Manufacture Multi-layer Depositions of Ti-9Mo-7Nb-xCu Alloys. Fig. 3.13 shows a photograph of different locations of samples that were cut from the multilayer deposition of Ti-9Mo-7Nb-xCu alloy developed by µ-PPAM process to perform density and porosity, microstructural analysis through SEM, phase evolution, tensile and compression testing, microhardness evaluation, fracture toughness and abrasion resistance test, cell viability assessment, cell adhesion study, release of metallic ion, and antibacterial testing.

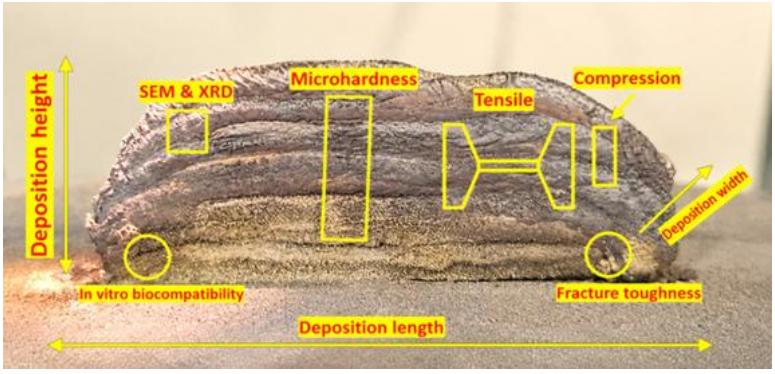


Fig 3.13: *Location of cutting different samples from the multi-layer depositions of Ti-9Mo-7Nb-xCu for evaluation of different tests.*

3.7 Density and porosity evaluation

One cuboid sample having dimensions of 8 mm length, 8 mm width, and 3 mm thickness was cut from each multi-layer deposition of Ti–9Mo–7Nb–2Cu, Ti–9Mo–7Nb–4Cu, and Ti–9Mo–7Nb–6Cu alloys using the Wire Electrical Discharge Machining (WEDM) process. The samples were extracted from the central region of the deposited structure to ensure uniformity and reliability in measurements. Prior to density measurement, the samples were ultrasonically cleaned and dried to remove surface contaminants and moisture.

Experimental density *'ρ_e'* was determined using Archimedes principle as expressed in Eq. 3, whereas the theoretical density *'ρ_t'* was computed using the rule of mixtures represented in Eq. 4. The mass of each sample in air *'m_a'* and deionised (DI) water *'m_w'* was measured using a weighing balance (model: *ME204* from Mettler Toledo) having a least count of ±1 mg. The measurements in DI water were recorded only after ensuring that no air bubbles remained attached to the sample surface. Measurement of each sample was repeated three times, and its average value was further considered for analysis.

$$\rho_e = \frac{m_a}{m_a - m_w}\rho_w \tag{3}$$

$$\rho_t = \sum_{i=1}^{n} \rho_i f_i \tag{4}$$

where *'ρ_i'* and *'f_i'* represent the density and atomic fraction of the i^{th}element of the alloy, respectively.

3.8 Study of microstructure and phase evolution

One cuboid sample of 5 mm length, 5 mm width, and 2 mm thickness was cut from each of the multi-layer depositions of Ti-9Mo-7Nb-2Cu, Ti-9Mo-7Nb-4Cu, and Ti-9Mo-7Nb-6Cu alloys. Then the cut samples were polished with SiC emery papers up to 2500 grit size, then polished by alumina liquid of fineness 1-1.5 μm spread over a velvet cloth, followed by colloidal silica gel to achieve 0.5 μm fineness. The polished samples were then etched using Keller's reagent (190 mL distilled water, 5 mL HNO_3, 3 mL HCl, and 2 mL HF) for 10–20s to reveal their microstructure. Evolution of different phases was analysed using an X-ray diffractometer (XRD) (model: P*ANalytical*; Empyrean, Netherlands) at room temperature using λ radiation having 1.54 Å wavelength, 2θ angle from 20◦ to 90◦, and a dwell period of 1-2 s.

The observed peaks in the XRD plot of a deposition sample were matched with the database of the International Centre for Diffraction Data (ICDD) using the *X'PertHighScorePlu*s analysis software to identify the major phases present in it and their crystal structures.

3.9 Microhardness Evaluation

One sample having dimensions of 6 mm length along the deposition direction, 22 mm height along the build direction, and 3 mm width along the deposition width was cut from each multi-layer deposition of Ti–9Mo–7Nb–2Cu, Ti–9Mo–7Nb–4Cu, and Ti–9Mo–7Nb–6Cu alloys using the Wire Electrical Discharge Machining (WEDM) process. The samples were sectioned along the build direction to study the variation in microhardness throughout the deposited layers.

Prior to microhardness testing, the cut samples were ground and polished using SiC emery papers of progressively finer grit sizes up to 2500 grit to obtain a smooth and scratch-free surface. Proper surface preparation was necessary to ensure accurate indentation measurements and minimize experimental errors during hardness testing.

Microhardness measurements were carried out using a Vickers microhardness tester (Model: VMH-002, Walter UHL, Germany) according to ASTM E92–82 standard. A load of 10 N was applied for a dwell time of 15 s during each indentation. The Vickers hardness test was selected because of its suitability for evaluating localized hardness variations in additively manufactured metallic deposits.

The microhardness of each sample was measured at 10 different locations along the build direction with an interval of 2 mm between successive indentations in order to obtain the microhardness profile throughout the deposition height. Multiple measurements were performed to evaluate the uniformity of hardness distribution and to study the influence of layer-by-layer deposition on mechanical behavior.

3.10 Tensile test and its fractography

Three tensile specimens were cut from each multi-layer deposition of Ti–9Mo–7Nb–2Cu, Ti–9Mo–7Nb–4Cu, and Ti–9Mo–7Nb–6Cu alloys using the Wire Electrical Discharge Machining (WEDM) process according to ASTM E8M standard. The tensile specimens were extracted along the deposition direction to evaluate the mechanical behaviour of the fabricated alloys under tensile loading conditions. The geometry and dimensions of the tensile specimen

are shown in Fig. 3.14. Each specimen had an overall length of 25.4 mm, gauge length of 7.62 mm, width of 5 mm, and thickness of 1.2 mm.

Prior to testing, the specimen surfaces were properly cleaned and finished to remove surface irregularities and machining marks. Tensile testing was carried out using a universal testing machine (UTM) (Model: H50KL, Tinius Olsen, USA) at a constant crosshead speed of 1 mm/min under room temperature conditions. The tensile tests were performed to determine important mechanical properties such as yield strength, ultimate tensile strength (UTS), and percentage elongation of the developed Ti–9Mo–7Nb–xCu alloys.

For each alloy composition, three specimens were tested and the average values of the obtained tensile properties were considered for further analysis in order to improve reliability and minimize experimental variation. The tensile behaviour of the deposited alloys provided important information regarding the influence of Cu addition, microstructural evolution, and phase formation on the strength and ductility of the fabricated structures.

Furthermore, the fracture surfaces of the tensile-tested specimens were examined using scanning electron microscopy (SEM) to investigate their fracture characteristics and failure mechanisms. Fractographic analysis was carried out to identify features such as dimples, cleavage facets, microvoids, river patterns, and crack propagation behaviour. The SEM analysis helped in understanding the ductile or brittle nature of fracture and the influence of alloy composition and deposition conditions on the tensile failure behaviour of the developed alloys.

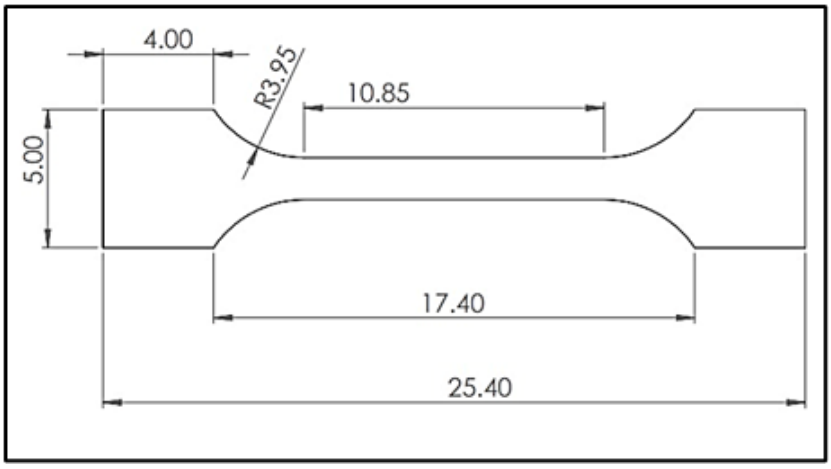


Fig 3.14: *Tensile test samples of Ti-9Mo-7Nb-xCu alloy dimensions as per standard ASTM E8M.*

3.11 Compressive Test

Three cylindrical specimens having dimensions of 3 mm diameter and 6 mm height were cut from each multi-layer deposition of Ti–9Mo–7Nb–2Cu, Ti–9Mo–7Nb–4Cu, and Ti–9Mo–7Nb–6Cu alloys using the Wire Electrical Discharge Machining (WEDM) process according to ASTM E9M standard. The specimens were extracted from the deposited region to evaluate the compressive behaviour and load-bearing capability of the fabricated alloys.

Prior to testing, the sample surfaces were properly finished and cleaned to ensure parallel and smooth loading faces for accurate compression testing. Compression tests were carried out at room temperature using a precision universal testing machine (UTM) (Model: H50KL, Tinius Olsen, USA). The tests were performed at a constant strain rate of 0.001 s^{-1} to determine important compressive properties such as compressive yield strength, ultimate compressive strength, and percentage increase in cross-sectional area after deformation.

For each alloy composition, three specimens were tested and the average values of the obtained compressive properties were considered for further analysis to improve reliability and reduce experimental variation. The compressive testing was carried out to study the deformation behaviour, strength, and plasticity of the developed Ti–9Mo–7Nb–xCu alloys under compressive loading conditions.

3.12 Fracture toughness and abrasion resistance

One cylindrical sample of 8 mm diameter and 3 mm thickness was cut from each multi-layer deposition of Ti-9Mo-7Nb-2Cu, Ti-9Mo-7Nb-4Cu, and Ti-9Mo-7Nb-6Cu alloys by the WEDM process. The cut samples were hot-mounted and wet-ground up to 2500 grit size, followed by fine polishing using alumina suspension on a velvet cloth to achieve 1-1.5 μm fineness. Abrasion resistance of each sample was evaluated through a scratch test as per ASTM G171-03 standard using a scratch tester (Model: *TR-101*, Ducom Instruments, India). A conical diamond stylus having a tip radius of 200 μm and a half apex angle of 120° was employed during the test. Scratch tests were carried out under applied normal loads of 1, 5, and 10 N, scratch track length of 3 mm and a sliding speed of 0.5 mm/min. The width *'w'* and depth *'d'* of the scratch track length were measured using an optical microscope and 3D surface profilometer (model: *LD 130*, MarSurf, Germany), respectively. The scratch hardness number 'H_s' and scratch volume *'*S_v*'* were calculated using Eq. 5 and Eq. 6:

$$H_S = \frac{8F}{\pi w^2} \tag{5}$$

$$S_v = \frac{D^2 L}{8}\left[2\sin^{-1}\left(\frac{w}{D}\right) - \sin\left\{2\sin^{-1}\left(\frac{w}{D}\right)\right\}\right] \tag{6}$$

Where '*F'* is the applied scratch load in N, *w*is the scratch track width (mm), *'D'* is the stylus diameter (0.4 mm), and *'L'* is the scratch length (3 mm). The fracture toughness *'F_t'* was estimated according to the methodology proposed by Akono et *al.* [57] and Akono and Ulm [92], using Eq. 7:

$$F_t = \frac{F_{eq}}{S} \tag{7}$$

where $F_{eq} = F_h$ for $\alpha = 0$, and

$$F_{eq} = \sqrt{F_h^2 + \frac{3}{5}F_v^2} \tag{8}$$

for $\alpha > 0$. The shape factor *'S'* of the conical stylus was determined using:

$$S = \sqrt{4d^3\left(\frac{\tan\phi}{\cos\phi}\right)} \tag{9}$$

Where *'F_h'* and *'F_v'* are the horizontal and vertical scratch loads in N, '*d'* is the scratch depth (mm), and *'Φ'* is the half apex angle of the cone-shaped diamond stylus (=120^o); and *'α'* is the position of the cone-shaped diamond stylus during the scratch test.

3.13 Metallic ions release analysis

Twelve cylindrical samples of 8 mm diameter and 2 mm thickness were cut from each multi-layer deposition of Ti-9Mo-7Nb-2Cu, Ti-9Mo-7Nb-4Cu, and Ti-9Mo-7Nb-6Cu alloys by the WEDM process. Each cut sample was used to study the metallic ion release. The samples were wet ground using SiC emery papers up to 1200 grit size, followed by ultrasonic cleaning in ethanol and distilled water to remove surface contaminants, followed by sterilisation in an autoclave for 30 min. Before immersion testing, the tubes were cleaned using 5 vol.% concentrated HNO_3 solution and ultrapure water to eliminate any impurities. The metallic ion release behaviour of each sample was evaluated in simulated body fluid (SBF) and phosphate-buffered saline (PBS) solutions maintained at 5.4 and 7.4 pH. The samples were then immersed

in PBS and SBF solution at 5.4 and 7.4 pH for durations of 1, 2, and 3 weeks, and 3 weeks at 37 °C. After each immersion duration, the concentration of metallic ion release from each sample in PBS and SBF solution at 5.4 and 7.4 pH was measured using Inductively Coupled Plasma -Optical Emission Spectroscopy (ICP-OES). Ti, Mo, Nb, and Cu released ion concentrations were quantified in parts per million (ppm), and their average value was used for further analysis.

3.14 Cell viability analysis

Four cylindrical samples of 8 mm diameter and 2 mm thickness were cut from each multi-layer deposition of Ti-9Mo-7Nb-2Cu, Ti-9Mo-7Nb-4Cu, and Ti-9Mo-7Nb-6Cu alloys by the WEDM process. The samples were wet ground using 2500-grit SiC papers, followed by ultrasonic cleaning in ethanol for 4 hours and distilled water to remove surface contaminants, followed by sterilisation in an autoclave for 30 min. The sterilised samples were immersed in Dulbecco's Modified Eagle Medium (DMEM) and incubated at 37 °C in a humidified atmosphere containing 5% CO_2 for immersion durations of 2, 4, and 6 days to obtain conditioned media containing released metallic ions from the developed alloys. After each immersion period, the extracted media were collected for *in-vitro* biocompatibility studies. The cell viability study was carried out using the L929 mouse fibroblast cell line. These cells were cultured in DMEM supplemented with fetal bovine serum (FBS) and antibiotics and maintained at 37 °C under 5% CO_2. The cells were subcultured after reaching approximately 80-90% confluency. For cell viability analysis, L929 cells were seeded in a 96-well plate at a density of 10000 cells /well and incubated for 24 h to allow cell attachment. Cell viability was performed using MTT (3-(4,5-dimethylthiazol-2-yl)-2,5-diphenyltetrazolium bromide) assay. The conditioned media corresponding to different immersion durations were added to the wells, followed by the addition of MTT reagent (0.5 mg/mL). The plates were incubated for 3 h at 37 °C in dark conditions for the formation of formazan crystals by viable cells. After incubation, dimethyl sulfoxide (DMSO) was added to dissolve the formazan crystals, and the absorbance was measured using a microplate reader at a wavelength of 570 nm. Untreated cells cultured in normal DMEM medium were considered as the control group. The percentage of cell viability was calculated using Eq.10.

$$\text{Cell viability (\%)} = \frac{\text{Absorbance of treated cells}}{\text{Absorbance of control cells}} \times 100 \qquad (10)$$

All experiments were repeated five times, and the average values along with standard deviation were used for analysis.

3.15 Cell adhesion assessment

Four cylindrical samples of 8 mm diameter and 2 mm thickness were cut from each multi-layer deposition of Ti-9Mo-7Nb-2Cu, Ti-9Mo-7Nb-4Cu, and Ti-9Mo-7Nb-6Cu alloys by the WEDM process. The samples were wet ground using 2000-grit SiC papers, followed by ultrasonic cleaning in ethanol for 2 hours and distilled water to remove surface contaminants, followed by sterilisation in an autoclave for 30 min. The cleaned samples were then sterilised under ultraviolet (UV) light for 24h to ensure aseptic conditions before cell culture experiments. The cell adhesion behaviour of the developed alloys was evaluated using the L929 fibroblast-like mouse cell line. The cells were cultured in Dulbecco's Modified Eagle Medium (DMEM) supplemented with fetal bovine serum (FBS) and antibiotics under a humidified atmosphere containing 5% CO_2 at 37°C. The cells were subcultured after reaching approximately 80–90% confluency. For the cell adhesion study, the sterilized samples were placed in a 48-well culture plate, and the L929 cell line was seeded onto each sample surface at a density of 5×10^4 cells/well. The seeded samples were incubated at 37 °C for 24 h to allow cell attachment and spreading on the alloy surfaces. After incubation, the samples were gently washed with phosphate-buffered saline (PBS) solution to remove non-adherent cells. Live and dead cell staining was performed using Calcein-AM and propidium iodide dyes, respectively. Calcein-AM penetrates viable cells and is converted into fluorescent calcein by intracellular esterases, resulting in green fluorescence from live cells. In contrast, propidium iodide penetrates damaged or dead cells and binds with nucleic acids, producing red fluorescence. Calcein-AM solution and propidium iodide were added to the samples at concentrations of 1 and 2 μg/mL, respectively, followed by incubation under dark conditions. The cells attached on the surfaces of each sample were examined using a fluorescence microscope and cell morphology was carried out using SEM. The obtained fluorescence and SEM micrograph images were used to assess the cell adhesion morphology in the developed alloys.

3.16 Bacterial inhibitory test

Three cylindrical samples of 8 mm diameter and 2 mm thickness were cut from each multi-layer deposition of Ti-9Mo-7Nb-2Cu, Ti-9Mo-7Nb-4Cu, and Ti-9Mo-7Nb-6Cu alloys by the

WEDM process. The samples were wet ground using 2000 grit size, followed by ultrasonic cleaning in ethanol for 2 hours and distilled water to remove surface contaminants, followed by sterilisation under UV light for 1 h. The *E. coli* bacterial strain was cultured in lysogeny broth (LB) medium at 37 °C, and 5 % CO_2 until reaching a concentration of approximately 10^7 CFU/mL. The bacterial suspension was subsequently diluted using PBS to obtain a final growth concentration of 10^7 CFU/mL. Each sterilised specimen was placed individually into a 96-well culture plate, followed by the addition of 50 µL of the diluted bacterial suspension into each well. The specimens were then incubated at 37 °C for 24 h under sterile conditions to allow bacterial interaction with the surface in all the developed alloys.

After incubation, the bacterial suspension collected from each well was diluted, and 100 µL aliquots were spread uniformly onto solid nutrient agar plates. The agar plates were incubated again at 37 °C for 24 h, after which the number of viable bacterial colonies was counted using the plate-count method according to the GB/T 2591 standard. The antibacterial rate (AR) of the alloy specimens was calculated using the following equation:

$$\mathrm{AR} = \frac{\mathrm{N_{control}} - \mathrm{N_{sample}}}{\mathrm{N_{control}}} \times 100 \qquad (11)$$

where $N_{control}$ represents the number of bacterial colonies observed for the control sample, and N_{sample} represents the number of bacterial colonies observed for the Ti-9Mo-7Nb-2Cu, Ti-9Mo-7Nb-4Cu, and Ti-9Mo-7Nb-6Cu alloys.

Chapter 4

Results and Analysis for Ti-9Mo-7Nb-xCu

4.1 Results and analysis of single-layer depositions

Fig. 4.1 shows the photograph of single-layer depositions of Ti-9Mo-7Nb-4Cu alloy using the μ-PPAM process, which is categorised into 13 non-uniform discontinuous deposition (NCD) and 14 uniform and continuous deposition (UCD). Table 4.1 summarises measured and computed responses of the Ti-9Mo-7Nb-4Cu alloy for various combinations of input parameters, which include measured responses i.e., deposition width *'w'*, deposition height *'h'*, and diluted depth *'D_d'* and computed responses such as aspect ratio *'AR'*, dilution % *'D'*, and deposition efficiency *'η'* for different combinations of μ-plasma Power (W), Feedstock Powder Flow Rate (g/min), and Travel speed of deposition head (mm/min). Fig. 4.2 presents variation in deposition width *'w'*, deposition height *'h'*, and deposition efficiency *'η'*, diluted depth *'D_d'*, and dilution % *'D'* of single-layer depositions of Ti-9Mo-7Nb-4Cu alloy: (a) μ-plasma Power (W), (b) Travel speed of deposition head (mm/min), and (c) Feedstock Powder Flow Rate (g/min).

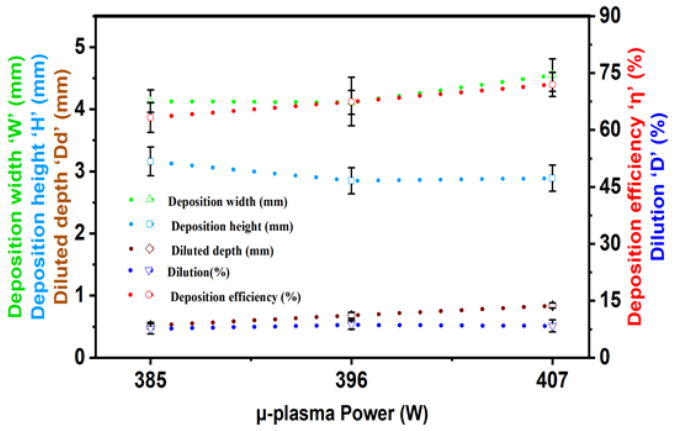
Table 4.1: *Measured and computed responses of the Ti-9Mo-7Nb-4Cu alloy for various combinations of input parameters in the μ-PPAM process*

Exp. No.	Variable input parameters			Measured responses			Computed responses		
	μ-plasma Power (W)	Travel speed of, deposition head (mm/min)	Feedstock Powder Flow Rate (g/min)	Deposition width *'w'* (mm)	Deposition height *'h'* (mm)	Diluted depth *'D_d'* (mm)	Aspect ratio *'AR'*	Dilution *'D'*(%)	Deposition efficiency *'η'* (%)
Uniform and continuous depositions (UCD)									
4	385	44	2.7	4.45	3.31	0.549	1.34	8.77	70.01
5	385	44	3	4.01	3.11	0.511	1.29	7.28	62.3
10	396	42	2.7	4.13	2.77	0.758	1.49	10.97	72.4
11	396	42	3	4.31	3.09	0.739	1.39	8.32	67.5
13	396	44	2.7	4.09	2.81	0.697	1.46	9.21	71.5
14	396	44	3	3.97	2.78	0.683	1.43	8.63	65.3
16	396	46	2.7	3.91	2.61	0.642	1.52	9.01	72.9
17	396	46	3	4.13	2.77	0.623	1.49	8.96	66.3

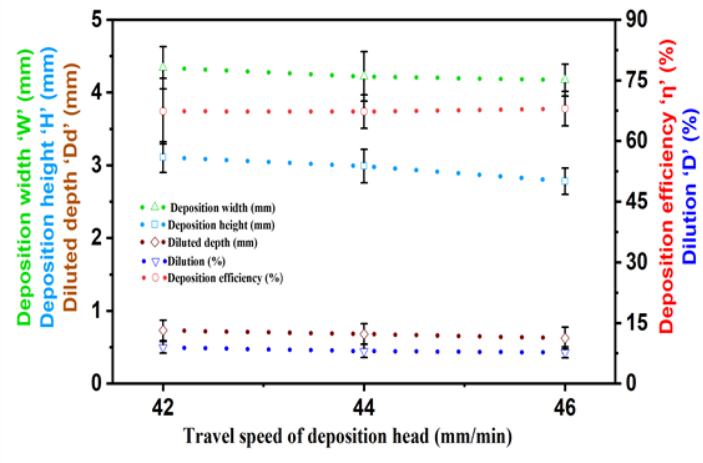
19	407	42	2.7	4.76	3.01	0.893	1.58	10.76	75.6
20	407	42	3	4.83	3.17	0.879	1.52	10.31	72.4
22	407	44	2.7	4.52	2.76	0.854	1.64	10.58	74.1
23	407	44	3	4.75	2.98	0.846	1.59	8.17	71
25	407	46	2.7	4.21	2.51	0.816	1.68	9.32	73.4
26	407	46	3	4.47	2.67	0.792	1.67	7.53	71.5
Nonuniform discontinuous deposition (NCD)									
1	385	42	2.7	3.98	3.01	0.593	1.32	9.47	68.8
2	385	42	3	4.19	3.31	0.573	1.27	8.33	61.3
3	385	42	3.3	4.23	3.44	0.567	1.23	7.03	57.7
6	385	44	3.3	4.11	3.37	0.497	1.22	5.69	61.2
7	385	46	2.7	3.91	2.74	0.479	1.43	8.23	65.3
8	385	46	3	4.37	3.14	0.451	1.39	6.93	62.7
9	385	46	3.3	3.94	2.97	0.436	1.33	5.49	61.1
12	396	42	3.3	4.49	3.28	0.721	1.37	7.32	53.2
15	396	44	3.3	3.84	2.73	0.663	1.41	7.81	69.4
18	396	46	3.3	4.09	2.81	0.607	1.46	7.59	68.7
21	407	42	3.3	4.13	2.91	0.871	1.43	8.14	77.4
24	407	44	3.3	4.79	3.05	0.833	1.57	6.39	66.6
27	407	46	3.3	4.52	2.77	0.778	1.63	6.33	71



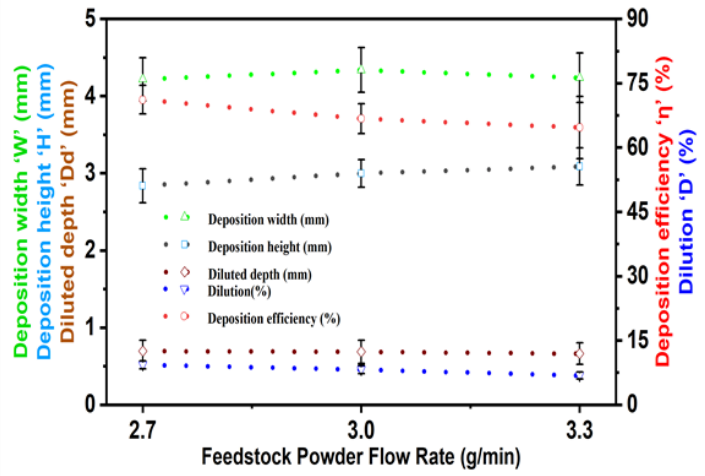
Fig 4.1: *Quality of single-layer depositions of Ti-9Mo-7Nb-4Cu alloy: (a) non-uniform and discontinuous deposition (NCD), and (b) uniform and continuous deposition (UCD).*


Deposition width 'W' (mm)
Deposition height 'H' (mm)
Diluted depth 'Dd' (mm)
Deposition efficiency 'η' (%)
Dilution 'D' (%)
Deposition width (mm)
Deposition height (mm)
Diluted depth (mm)
Dilution(%)
Deposition efficiency (%)
385
396
407
μ-plasma Power (W)

(a)


Deposition width 'W' (mm)
Deposition height 'H' (mm)
Diluted depth 'Dd' (mm)
Deposition efficiency 'η' (%)
Dilution 'D' (%)
Deposition width (mm)
Deposition height (mm)
Diluted depth (mm)
Dilution (%)
Deposition efficiency (%)
42
44
46
Travel speed of deposition head (mm/min)

(b)


Deposition width 'W' (mm)
Deposition height 'H' (mm)
Diluted depth 'Dd' (mm)
Deposition efficiency 'η' (%)
Dilution 'D' (%)
Deposition width (mm)
Deposition height (mm)
Diluted depth (mm)
Dilution(%)
Deposition efficiency (%)
2.7
3.0
3.3
Feedstock Powder Flow Rate (g/min)

(c)

Fig 4.2: *Variation in width, height, and efficiency of deposition, diluted depth, and dilution % of single-layer depositions of Ti-9Mo-7Nb-4Cu alloy: (a) μ-plasma Power (W), (b) Travel speed of deposition head (mm/min), and (c) Feedstock Powder Flow Rate (g/min).*

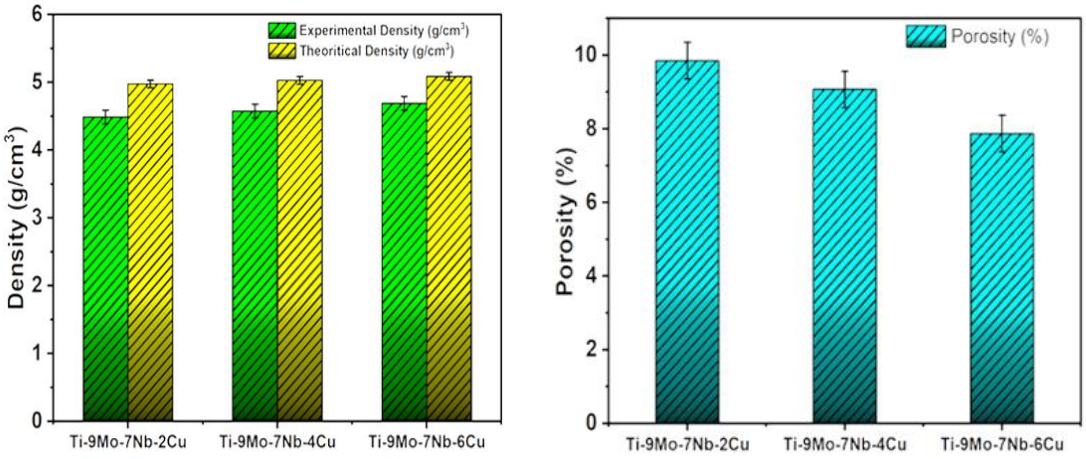
From Fig. 4.1 and Table 4.1, 27 main experiments were conducted, out of which 14 depositions were categorised into UCD and 13 as NCD. It can be observed from Fig. 4.2 a that an increase in the μ-plasma arc power from 385 to 407 W significantly increased the deposition width and deposition efficiency, while slightly decreasing the deposition height. This is due to the increase in the temperature of the molten pool, which reduces the molten metal viscosity, enhancing molten pool fluidity and spreading. Furthermore, an increase in μ-plasma arc power promotes better melting of feedstock powder and improved metallurgical bonding with the substrate, thereby slightly increasing its diluted depth and dilution %. The maximum deposition efficiency of 77.4% was obtained at 407 W, confirming its improved material utilisation under higher μ-plasma arc power conditions. From Fig. 4.2 b, deposition head travel speed exhibited an inverse effect on the single-layer deposition. Increase in the deposition head travel speed from 42 to 46 mm/min reduced the deposition width, deposition height, diluted depth, dilution %, and its deposition efficiency. This is due to reduction in the interaction time between the heat source and feedstock powder, thereby lowering molten pool temperature and decreasing its efficiency. Consequently, reduced heat transfer to the substrate limited substrate melting and resulted in lower dilution and diluted depth. Additionally, the increased viscosity of the molten pool at higher deposition head travel speed restricted molten metal flow, leading to narrower and thinner deposited tracks. From Fig. 4.2 c, the mass flow rate of feedstock powder also influenced the deposition efficiency. Increase in the powder mass flow rate from 2.7 to 3.3 g/min increased both its deposition width and height due to the greater availability of feedstock material for deposition. Consequently, reduced its deposition efficiency and dilution because the available heat energy was insufficient to completely melt the feedstock powder. As a result, a portion of the powder remained partially melted or unmelted, leading to powder wastage and unstable deposition behaviour. This phenomenon was particularly evident in several NCD fabricated at 3.3 g/min powder flow rate.

4.2 Results and analysis of multi-layer depositions

Fig. 4.2 consists of 3 parametric responses, i.e., maximum deposition efficiency, minimum aspect ratio, and minimum dilution of UCD, which were used to manufacture multi-layer depositions of Ti-9Mo-7Nb-2Cu, Ti-9Mo-7Nb-4Cu, and Ti-9Mo-7Nb-6Cu alloys using the μ-PPAM process. These parametric responses promote strong interlayer bonding, deposition stability, and enhanced homogeneity during multilayer depositions. Therefore, Exp. No. 11 yielded 396 W μ-plasma power, 42 mm/min deposition head travel speed, and 3 g/min mass flow rate of feedstock powder as the optimum parametric combination to fabricate its multilayer depositions. Fig. 3.13 shows the photograph of the multilayer deposition of Ti-9Mo-7Nb-4Cu alloy, which consists of 9 deposited layers of 27 mm deposition height.

4.3 Porosity and density results

Fig. 4.3a depicts a bar graph showing variation in experimental density and theoretical density of multilayer deposition of Ti-9Mo-7Nb-2Cu, Ti-9Mo-7Nb-4Cu, and Ti-9Mo-7Nb-6Cu alloys, and Fig. 4.3b depicts their average porosity %. Table 4.2 summarises their experimental density, theoretical density, relative density %, and porosity %.



(a) **(b)**

Fig. 4.3 *(a) Comparison of experimental density and theoretical density, and (b) average porosity % of Ti-9Mo-7Nb-2Cu, Ti-9Mo-7Nb-4Cu, and Ti-9Mo-7Nb-6Cu alloys*

Table 4.2: *Experimental density, theoretical density, relative density, and porosity values of Ti-9Mo-7Nb-2Cu, Ti-9Mo-7Nb-4Cu, and Ti-9Mo-7Nb-6Cu alloys*

Alloy type	**Experimental density (g/cm³)**	**Theoretical density (g/cm³)**	**Relative density (%)**	**Porosity (%)**
Ti-9Mo-7Nb-2Cu	4.485	4.975	90.15	9.85
Ti-9Mo-7Nb-4Cu	4.574	5.030	90.93	9.07
Ti-9Mo-7Nb-6Cu	4.686	5.086	92.13	7.87

It can be observed from Fig. 4.3a and Table 4.2 Ti-9Mo-7Nb-6Cu alloy has the maximum experimental and theoretical density and minimum porosity %, whereas the Ti-9Mo-7Nb-2Cu alloy has the minimum value of experimental and theoretical density but maximum porosity %, and the Ti-9Mo-7Nb-4Cu alloy has in between those of the other two alloys. This is due to the high density and lower melting point of Cu as compared to Ti, Mo, and Nb, which results in better filling of interlayer gaps and fluidity. which promotes enhanced densification and better spreading and filling of interlayer gaps, thereby reducing the formation of pores and lack-of-fusion defects.

4.4 Analysis of evolution of phases

Fig. 4.4 illustrates XRD graphs of Ti-9Mo-7Nb-2Cu, Ti-9Mo-7Nb-4Cu, and Ti-9Mo-7Nb-6Cu alloys. Presence of α-Ti having a hexagonal Close-Packed (HCP) crystal, β-Ti consists of body-centred cubic (BCC), TiO_2, and Ti_2Cu intermetallic phase. XRD peaks corresponding to the β-Ti phase are clearly visible in all developed alloys, suggesting that Mo and Nb act as effective β-phase stabilisers, while the presence of the α-phase suggests partial transformation of the matrix during solidification or cooling. With increasing Cu content, the intensity of the Ti_2Cu intermetallic phase peaks becomes more pronounced, indicating enhanced formation of Ti_2Cu intermetallic phases at increased Cu contents. Increased in the Ti_2Cu intermetallic phases formation is attributed to the limited solubility of Cu in the Ti matrix during rapid solidification, resulting in precipitation of Ti_2Cu intermetallic within the developed alloys. In addition, the development of low TiO_2 peaks was observed in all the developed alloys. The Ti-9Mo-7Nb-6Cu alloy exhibits the highest intensity peak of Ti_2Cu intermetallic phase among all the developed alloys, indicating increased precipitation of Cu-rich intermetallic phases at higher Cu content. Consequently, the Ti-9Mo-7Nb-6Cu alloy exhibits relatively lower α-phase peak

intensity compared to the Ti-9Mo-7Nb-2Cu alloy, indicating improved retention of the β-phase at higher Cu concentrations.

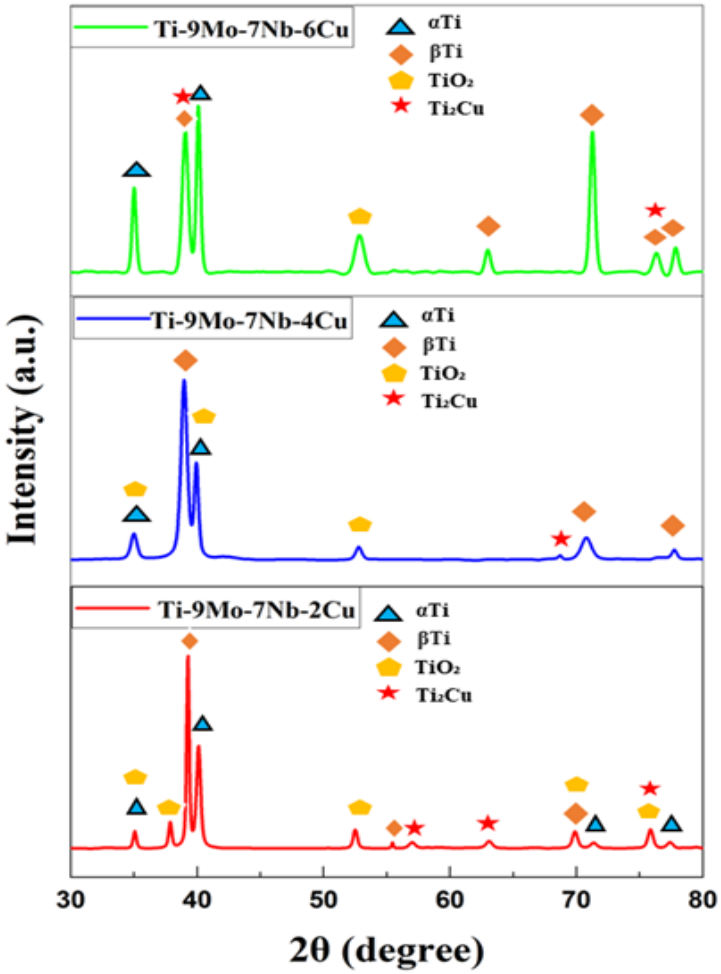
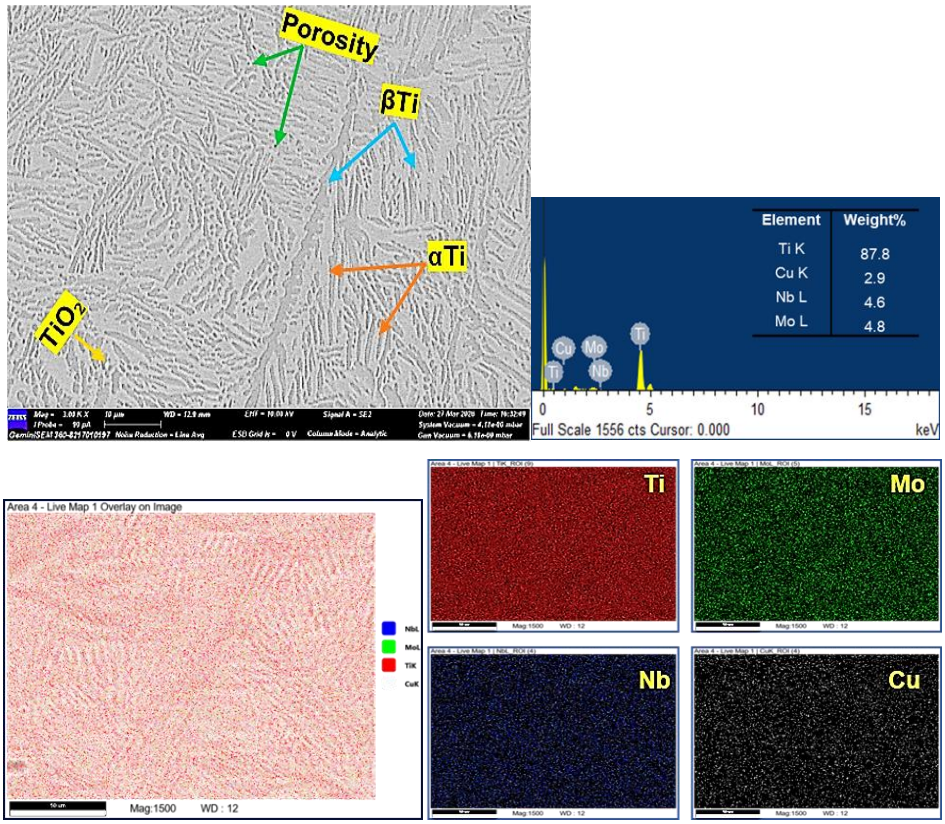


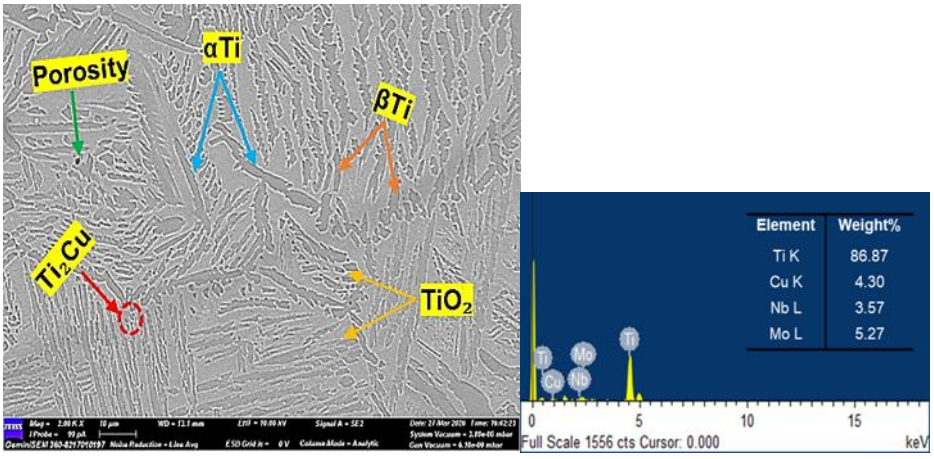
Fig 4.4: *Evolution of phases in multilayer depositions of Ti-9Mo-7Nb-2Cu, Ti-9Mo-7Nb-4Cu, and Ti-9Mo-7Nb-6Cu alloys.*

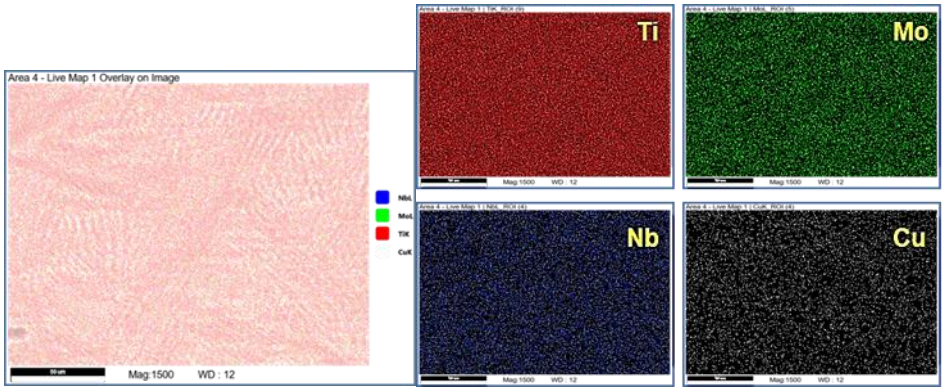
4.5 Microstructure analysis

*Fig. 4.5*a, *4.5*b, and *4.5*c represent the SEM images, chemical composition, area live mapping, and elemental mapping of μ-PPAM developed multilayer deposition of Ti-9Mo-7Nb-2Cu, Ti-9Mo-7Nb-4Cu, and Ti-9Mo-7Nb-6Cu alloy.

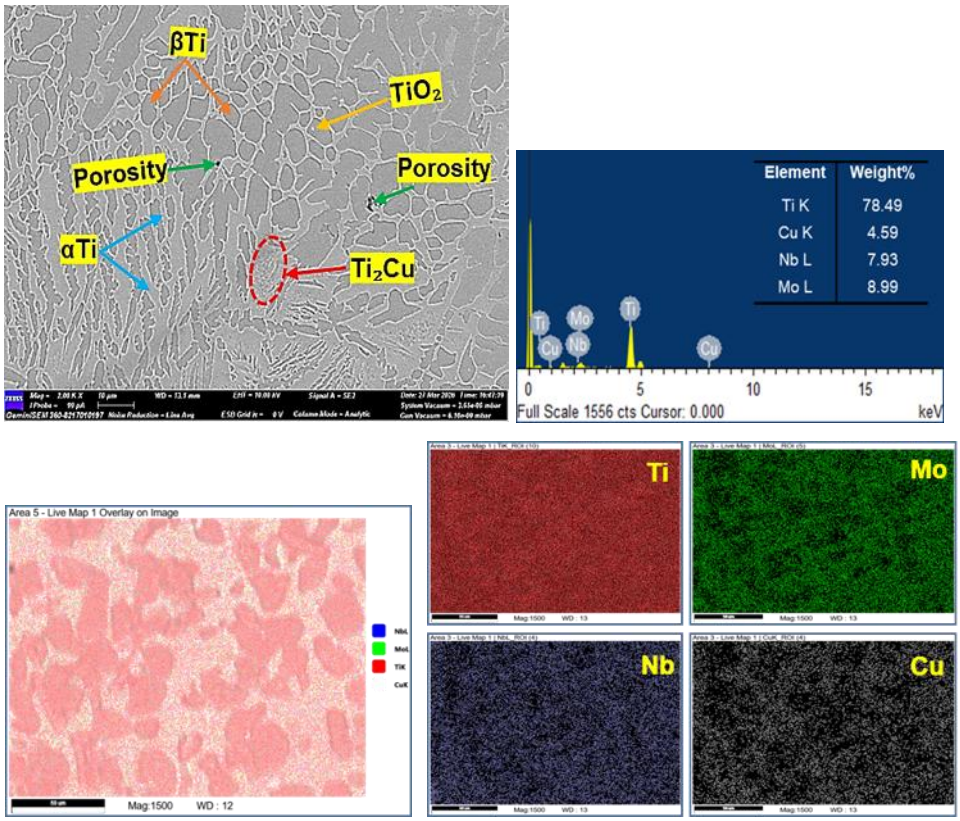

Porosity
βTi
αTi
TiO2
Element
Weight%
Ti K
87.8
Cu K
2.9
Nb L
4.6
Mo L
4.8
Full Scale 1556 cts Cursor: 0.000
keV
Area 4 - Live Map 1 Overlay on Image
Mag:1500
WD : 12
Ti
Mo
Nb
Cu

(a)


Porosity
αTi
βTi
Ti2Cu
TiO2
Element
Weight%
Ti K
86.87
Cu K
4.30
Nb L
3.57
Mo L
5.27
Full Scale 1556 cts Cursor: 0.000
keV



(b)



(c)

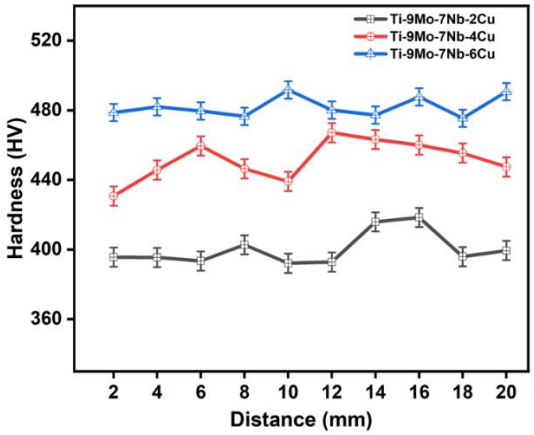
Fig 4.5: *Represent SEM morphology images, chemical composition, area live mapping, and elemental mapping of μ-PPAM developed multilayer deposition of* ***(a)*** *Ti-9Mo-7Nb-2Cu,* ***(b)*** *Ti-9Mo-7Nb-4Cu, and* ***(c)*** *Ti-9Mo-7Nb-6Cu alloy*

It can be observed that the microstructure of developed alloys consists of a primary β-Ti matrix phase with a secondary α-Ti phase, TiO_2 and intermetallic Ti_2Cu. EDS result confirms the presence of the alloying elements in the developed alloys is consistent with their nominal compositions. Presence of a small number of pores located at the grain boundaries of the α-Ti

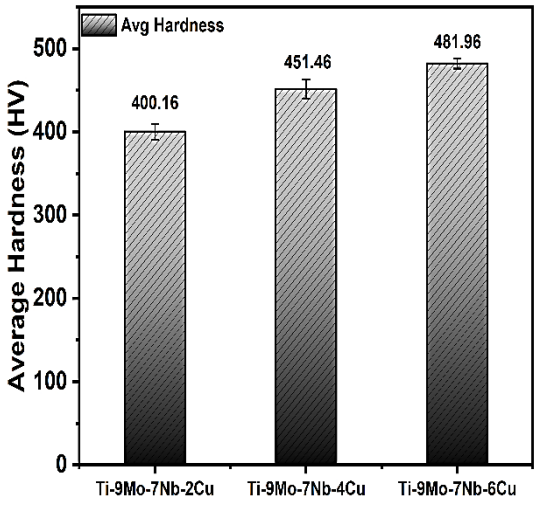
phase. However, the development of the TiO_2 phase remains comparatively low in all the developed alloys. From Fig. 4.5a, it can be observed that the microstructure of Ti-9Mo-7Nb-2Cu alloy predominantly consists of fine acicular α-Ti precipitates distributed within the retained β-Ti matrix. The Ti_2Cu intermetallic phase is present in a very limited amount because of the lower Cu contents and appears as fine precipitates. A comparatively higher amount of porosity is also observed in this alloy, which may be attributed to a lower amount of Cu, which was insufficient to adequately improve molten pool fluidity and fill the gaps. From Fig. 4.5b, the microstructure of Ti-9Mo-7Nb-4Cu alloy becomes comparatively denser and more refined. The amount of Ti_2Cu intermetallic phase increases due to the higher Cu content, and the precipitates become more distinct within the α+β matrix. The β-Ti phase becomes more stable and uniformly distributed owing to the β-stabilizing effect of Cu together with Mo and Nb. Furthermore, porosity decreases compared to the Ti-9Mo-7Nb-2Cu alloy because the increased Cu content improves molten pool fluidity and enhances consolidation during the μ-PPAM process. The lamellar α-Ti structure also appears finer and more uniformly distributed. From Fig. 4.5c, the microstructure of Ti-9Mo-7Nb-6Cu alloy exhibits the highest amount of Ti_2Cu intermetallic phase among all the developed alloys. The increase in Cu addition promotes the formation and growth of Cu-rich intermetallic precipitates within the matrix. The microstructure becomes significantly denser with comparatively lower porosity, indicating improved densification and better interlayer fusion during deposition. The β-Ti phase becomes more dominant due to enhanced β-phase stabilisation, while the α-Ti lamellae appear comparatively finer and more discontinuous. The reduction in porosity is mainly attributed to improved melting behaviour and enhanced molten pool spreading caused by the lower melting point of Cu. Overall, increasing Cu content from 2 wt.% to 6 wt.% results in increased formation of Ti_2Cu intermetallic phases, improved densification with reduced porosity, and enhances the β-phase in the Ti-9Mo-7Nb-6Cu alloy.

4.6 Microhardness results

Fig 4.6 shows microhardness profiles along the built direction of multilayer deposition of Ti-9Mo-7Nb-2Cu alloy, Ti-9Mo-7Nb-4Cu, and Ti-9Mo-7Nb-6Cu alloy developed by the μ-PPAM process and their average values of microhardness are presented through a bar diagram in Fig. 16b.



(a)



(b)

Fig 4.6: *Microhardness of the developed Ti-9Mo-7Nb-2Cu alloy, Ti-9Mo-7Nb-4Cu, and Ti-9Mo-7Nb-6Cu: (a) microhardness profile along the build direction, and (b) average values of microhardness.*

From *Fig. 4.6*, it can be observed that (i) an increase in the Cu content increases the average microhardness value for a minimum of 400.16 HV for Ti-9Mo-7Nb-2Cu alloy to 451.46 HV for Ti-9Mo-7Nb-4Cu alloy and reaches a maximum of 481.96 HV for Ti-9Mo-7Nb-6Cu alloy, (ii) the increase in hardness due to increasing Cu content from 2 to 6 wt.%, which promotes the formation of more amount of Ti_2Cu intermetallic phases within the α+β titanium matrix (shown in Fig. 4.5c). This intermetallic phase is comparatively hard and brittle in nature, thereby increasing resistance against localized plastic deformation and consequently enhancing the hardness in Ti-9Mo-7Nb-6Cu alloy, (iii) microstructure refinement due to addition of 6 wt.%

Cu increases its grain boundary area, which restricts the dislocation movement and contributes to an increase in microhardness, and (iv) Cu acts as a strengthening element and improves solid solution strengthening in the α+β titanium matrix. This reduced porosity and improved densification observed with increasing Cu content also contribute to achieving the maximum microhardness of Ti-9Mo-7Nb-6Cu alloy.

4.7 Results of tensile test and its fractography

Fig. 4.7 shows engineering stress- strain curves of Ti-9Mo-7Nb-2Cu alloy, Ti-9Mo-7Nb-4Cu, and Ti-9Mo-7Nb-6Cu alloy obtained from their uniaxial tensile tests. Figs. 4.8a, 4.8b, and 4.8c show the fractography of tensile samples after their tensile test. Table 4.3 presents values of their tensile yield strength, ultimate tensile strength (UTS), and % elongation.

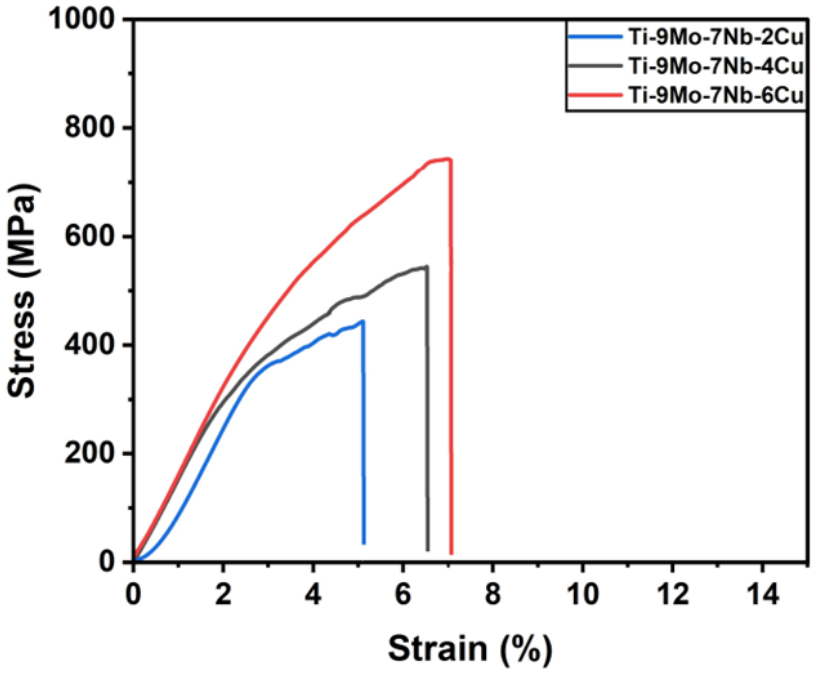
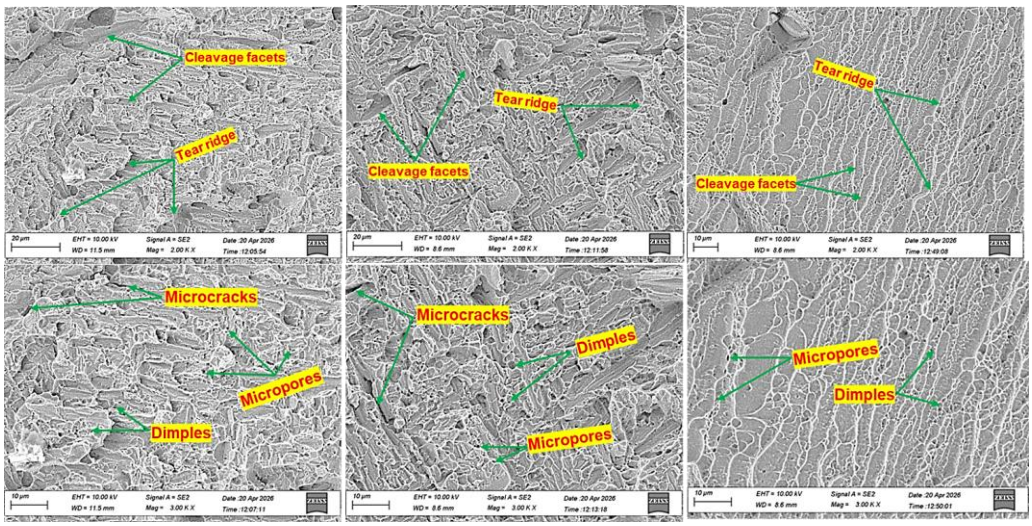


Fig 4.7: *Engineering stress and engineering strain graphs for μ-PPAM developed Ti-9Mo-7Nb-2Cu alloy, Ti-9Mo-7Nb-4Cu, and Ti-9Mo-7Nb-6Cu*



(a) **(b)** **(c)**

Fig 4.8: *SEM images showing the fractography of tensile samples of the developed: (a)Ti-9Mo-7Nb-2Cu alloy, (b) Ti-9Mo-7Nb-4Cu, and (c) Ti-9Mo-7Nb-6Cu alloy*

Table 4.3: *Tensile yield strength, Ultimate tensile strength (UTS) and % elongation for Ti-9Mo-7Nb-2Cu alloy, Ti-9Mo-7Nb-4Cu, and Ti-9Mo-7Nb-6Cu alloys obtained from their tensile tests.*

Alloy type	Tensile yield strength (MPa)	Ultimate tensile strength (MPa)	Elongation (%)
Ti-9Mo-7Nb-2Cu	368.5 ± 7.2	445.8 ± 8.6	5.2 ± 0.5
Ti-9Mo-7Nb-4Cu	462.4 ± 6.8	542.7 ± 7.9	6.5 ± 0.6
Ti-9Mo-7Nb-6Cu	645.3 ± 8.1	738.6 ± 9.4	7.1 ± 0.4

It can be observed from Fig. 4.7 and Table 4.3 that the Ti-9Mo-7Nb-2Cu alloy exhibits a minimum value of its tensile yield strength, UTS, and % elongation of 368.5 MPa, 445.8 MPa, and 5.2 %, and the Ti-9Mo-7Nb-6Cu alloy consists of a maximum value of tensile yield strength, UTS, and % elongation of 645.3 MPa, 738.6 MPa, and 7.1 % and the Ti-9Mo-7Nb-4Cu alloy has a value of 462.4 MPa of tensile yield strength, 542.7 MPa of UTS, and 6.5 % of %elongation. These observations were due to: (i) an increase in the Cu content from 2 to 6 wt.% promotes the formation of hard Ti_2Cu intermetallic precipitates and fine α-phase lamellae within the α+β titanium matrix, which strengthens the alloy by hindering dislocation movement.

Presence of high amount of hard intermetallic precipitates and improved distribution of the β-phase act as strong obstacles to dislocation motion, thereby restricting plastic deformation and enhancing the tensile yield strength, UTS and % elongation of the developed Ti-9Mo-7Nb-6Cu alloy and (ii) increase in the Cu content from 2 to 6 wt.% exhibit improved densification with reduced porosity, which leads to a more compact deposited structure with fewer internal voids and lack-of-fusion defects. This reduction in porosity minimises stress concentration sites that can initiate crack formation during tensile loading. Consequently, the applied load is distributed more uniformly throughout the material, improving the load-bearing capability and enhancing the overall tensile yield strength, UTS and % elongation of the developed Ti-9Mo-7Nb-6Cu alloy. Fig. 4.8a shows the fractography of the Ti-9Mo-7Nb-2Cu alloy, which exhibits a comparatively larger number of cleavage facets, microcracks, and micropores on the fractured surface. The presence of prominent cleavage facets indicates brittle fracture behaviour, while the observed micropores and microcracks may be associated with higher internal porosity and lack-of-fusion defects. A low number of dimples suggests comparatively lower plastic deformation before fracture, which corresponds to the lower tensile strength and % elongation during the tensile test. It can be observed from Fig. 4.8b that the Ti-9Mo-7Nb-4Cu alloy shows a comparatively reduced amount of cleavage facets and microcracks, along with an increased presence of dimples and tear ridges. The appearance of dimples indicates enhanced plastic deformation capability and improved ductile fracture behaviour. The reduction in micropores confirms improved densification and better metallurgical bonding due to increasing Cu content. Consequently, the alloy exhibits improved tensile yield strength, UTS and % elongation compared to the Ti-9Mo-7Nb-2Cu alloy. From Fig. 4.8c, the fracture morphology of the Ti-9Mo-7Nb-6Cu alloy suggests a denser fractured surface with fewer micropores and microcracks, along with well-developed dimples and tear ridges. The increased number of dimples indicates enhanced high-energy absorption capability and improved ductility during the tensile test. This reduced its porosity and improved interlayer fusion, contributing to better load transfer and delaying crack initiation during tensile loading. Furthermore, the refined α+β microstructure and increased formation of Ti_2Cu intermetallic precipitates enhance the tensile yield strength, UTS and % elongation of the alloy by restricting dislocation movement. As a result, the Ti-9Mo-7Nb-6Cu alloy.

4.8 Compressive test results

Fig. 4.9 shows engineering compressive stress-strain curves of Ti-9Mo-7Nb-2Cu alloy, Ti-9Mo-7Nb-4Cu, and Ti-9Mo-7Nb-6Cu alloy obtained from their compressive tests. Table 4.4 presents values of their yield compressive strength, ultimate compressive strength (UCS), and % increase in the cross-sectional area.

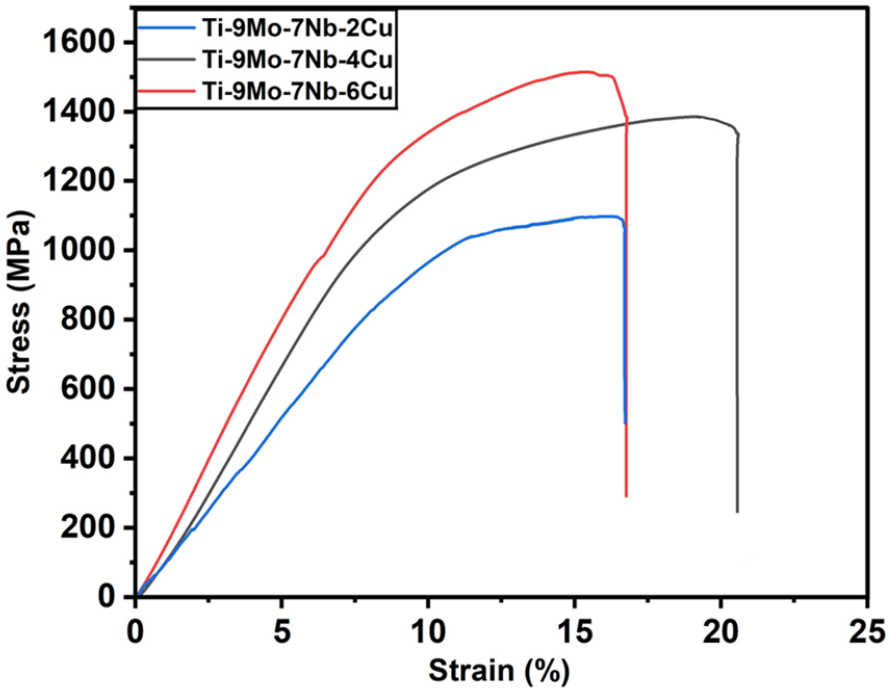


Fig 4.9: *Compressive stress–strain curve for μ-PPAM developed Ti-9Mo-7Nb-2Cu alloy, Ti-9Mo-7Nb-4Cu, and Ti-9Mo-7Nb-6Cu alloys*

Table 4.4: *Compressive yield strength, Ultimate compressive strength (UCS) and % increase in the cross-section area for Ti-9Mo-7Nb-2Cu alloy, Ti-9Mo-7Nb-4Cu, and Ti-9Mo-7Nb-6Cu alloys*

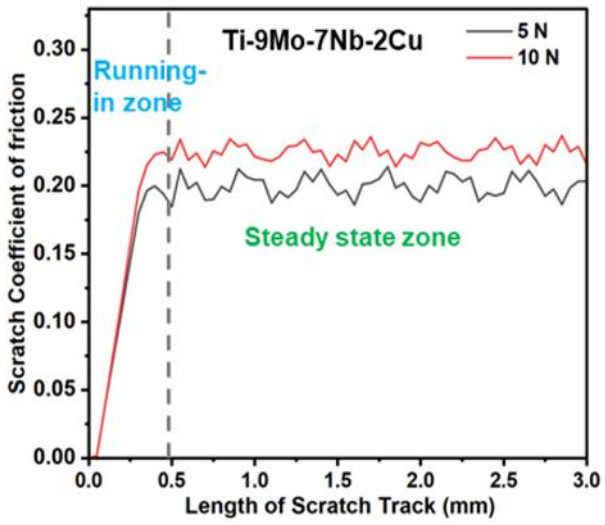
Alloy type	Compressive yield strength (MPa)	Ultimate compressive strength (MPa)	% Increase in cross-sectional area (%)
Ti-9Mo-7Nb-2Cu	401.3 ± 8.2	1098.6 ± 11.4	17.2 ± 0.6
Ti-9Mo-7Nb-4Cu	612.7 ± 7.9	1384.2 ± 10.1	20.5 ± 0.5
Ti-9Mo-7Nb-6Cu	798.4 ± 9.1	1512.8 ± 12.3	16.8 ± 0.4

It can be observed from Fig. 4.9 and Table 4.4 that the Ti-9Mo-7Nb-2Cu alloy exhibits a minimum value of compressive yield strength and UCS, and % increase in the cross-section area of 401.3MPa, 1098.6 MPa, and 17.2 %, and the Ti-9Mo-7Nb-6Cu alloy consists of a maximum value of compressive yield strength and UCS of 798.4 MPa and 1512.8 MPa, and a minimum 7.1 % of % increase in the cross-section area, and Ti-9Mo-7Nb-4Cu alloy has a value of 798.4 MPa compressive yield strength, 1512.8 MPa of UCS, and a maximum value of % increase in the cross-section area i.e., 16.8 %. These explanations are due to the following explanation: (i) Ti-9Mo-7Nb-6Cu alloy possesses a comparatively finer and denser microstructure with refined α-phase lamellae, and more uniformly distributed β-phase (shown in Fig. 4.5a). So, according to the Hall-Petch effect, refinement of grain size and reduction in lamellar spacing increase the grain boundary area, and these grain boundaries act as effective barriers to dislocation motion during compressive deformation. Consequently, higher resistance to plastic deformation is achieved, resulting in increased compressive yield strength and UCS, but excessive formation of hard Ti_2Cu intermetallic precipitates restricts dislocation motion, thereby reducing the plastic deformation and therefore reducing its % increase in the cross-section area, and (ii) an increase in the Cu content is also associated with the increased β-Ti phase stabilization. Mo and Nb are strong β-phase stabilizers, while Cu additionally assists in retaining the β-phase during solidification. The retained β-Ti phase possesses comparatively higher deformability and work-hardening capability, which enhances resistance against compressive deformation. Furthermore, the combined presence of refined α-phase lamellae and stable β-phase matrix contributes to improved load distribution and suppression of crack propagation during compression loading, thereby increasing its compressive yield strength and UCS.

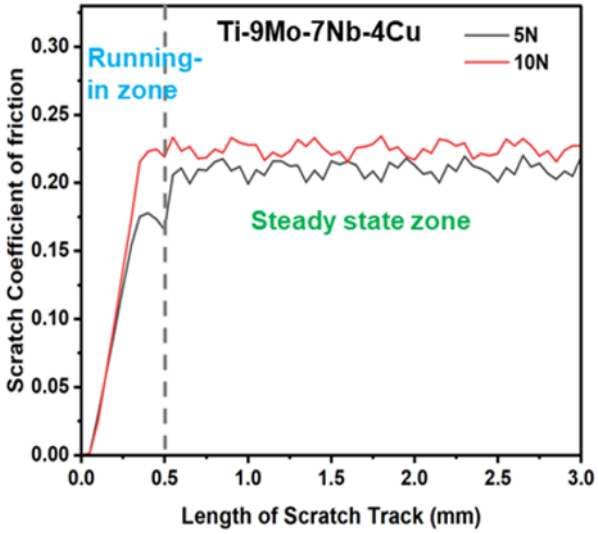
4.9 Fracture toughness and abrasion resistance results

Figs. 4.10 and 4.11 illustrate the variation of the coefficient of friction (COF) along the scratch track length and optical microscopic images of the track length at 5N and 10N applied load: (a) for Ti-9Mo-7Nb-2Cu alloy, (b) for Ti-9Mo-7Nb-4Cu alloy, and (c) for Ti-9Mo-7Nb-6Cu alloy. Fig. 4.12 depicts the effect of applied load at 5N and 10N for Ti-9Mo-7Nb-2Cu alloy, Ti-9Mo-7Nb-4Cu alloy, and Ti-9Mo-7Nb-6Cu alloy, showing: (a) average COF, (b) scratch volume, (c) fracture toughness and (d) scratch hardness. Table 4.5 computed average values of scratch COF (computed from the graphs of Fig. 4.10), measured values of scratch track width

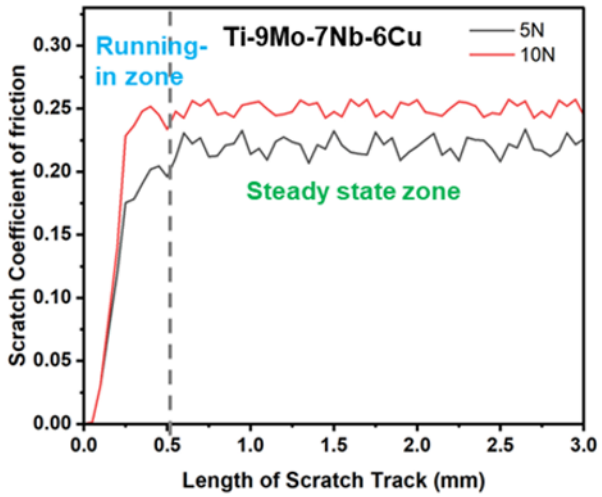
and depth, and computed fracture toughness and scratch hardness number of 5N and 10N applied load.



(a)

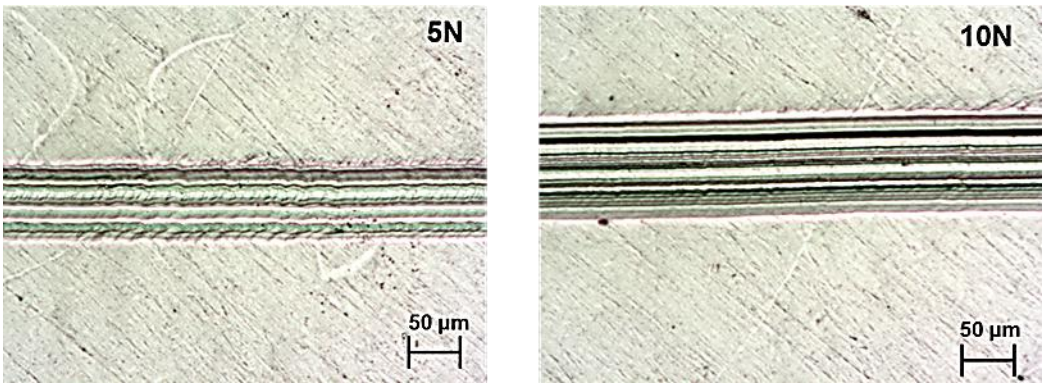


(b)

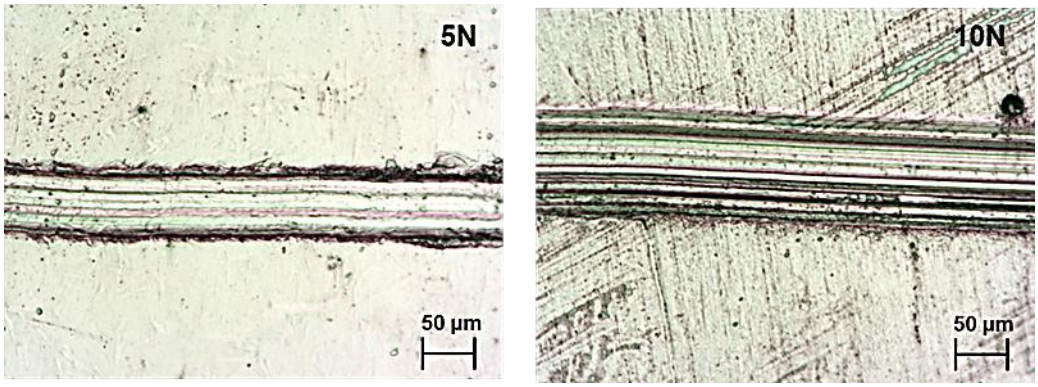


(c)

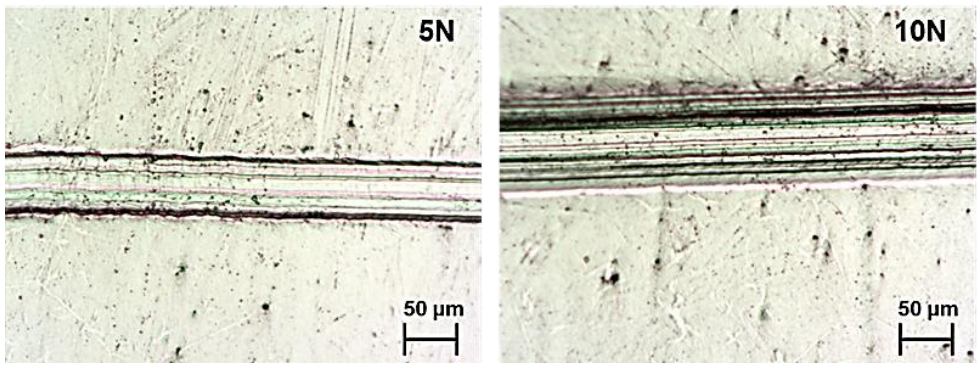
Fig 4.10: *Scratch COF variation along the scratch track length at different 5N and 10N applied loads for: (a)Ti-9Mo-7Nb-2Cu alloy, (b) for Ti-9Mo-7Nb-4Cu alloy, and (c) for Ti-9Mo-7Nb-6Cu alloy.*



(a)



(b)



(c)

Fig 4.11: *Optical microscopic images of the track length at 5N and 10N applied load: (a) for Ti-9Mo-7Nb-2Cu alloy, (b) for Ti-9Mo-7Nb-4Cu alloy, and (c) for Ti-9Mo-7Nb-6Cu alloy*

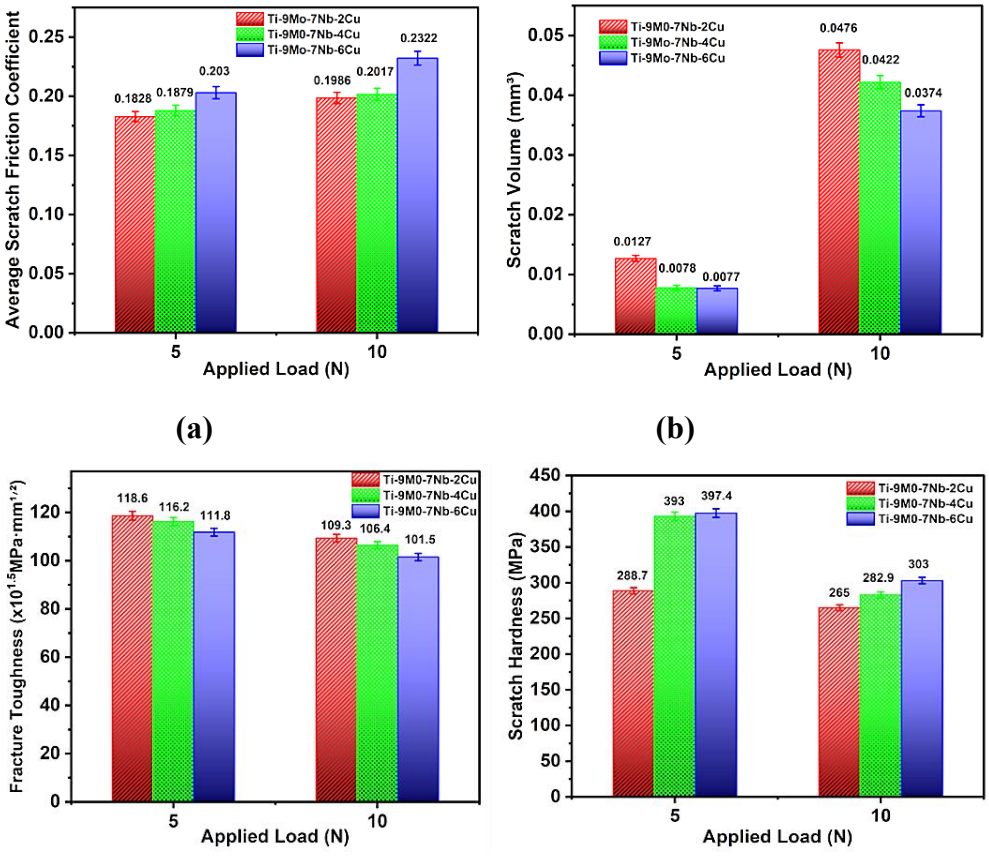


Fig 4.12: *Effect of applied load for Ti-9Mo-7Nb-2Cu alloy, Ti-9Mo-7Nb-4Cu alloy, and Ti-9Mo-7Nb-6Cu alloys on their: (a) average COF, (b) scratch volume, (c) fracture toughness and (d) scratch hardness.*

Table 4.5: *Computed values of average scratch COF, average scratch track width and depth, scratch volume, fracture toughness and scratch hardness number at different values of applied load for Ti-9Mo-7Nb-2Cu, Ti-9Mo-7Nb-4Cu, and Ti-9Mo-7Nb-6Cu alloys.*

Alloy type	**Applied Load (N)**	**Avg. Scratch COF**	**Avg. Depth of Scratch Track (µm)**	**Avg. Width of Scratch Track (µm)**	**Fracture Toughness ($x10^{1.5}$ $MPa \cdot mm^{0.5}$)**	**Scratch Hardness (MPa)**	**Scratch Volume (mm^3)**
Ti-9Mo-7Nb-2Cu	5	0.1828	1.57	210	118.6	288.7	0.0127
	10	0.1986	2.21	310	109.3	265	0.0476
Ti-9Mo-7Nb-4Cu	5	0.1879	1.718	180	116.2	393	0.0078
	10	0.2017	2.266	300	106.4	282.9	0.0422
Ti-9Mo-7Nb-6Cu	5	0.203	1.76	179	111.8	397.4	0.0077
	10	0.2322	2.326	289.9	101.5	303	0.0374

Figs. 4.10 (a, b, and c) and Table 4.5, at an applied load of 5 N, the average scratch COF values for Ti-9Mo-7Nb-2Cu, Ti-9Mo-7Nb-4Cu, and Ti-9Mo-7Nb-6Cu alloys are 0.1896, 0.1879, and 0.203, whereas at 10N the average scratch COF values for Ti-9Mo-7Nb-2Cu, Ti-9Mo-7Nb-4Cu, and Ti-9Mo-7Nb-6Cu alloys are 0.2017, 0.203, and 0.2322. It can be observed from Figs. 4.10 (a, b, and c) and 4.12a, and that the average scratch COF increases with an increase in applied load for all the developed alloys. The scratch COF profile can be divided into two distinct regions, i.e., the running-in zone and the steady-state zone. In the running-in zone, the COF rises rapidly up to nearly 0.5 mm scratch length due to the initial interaction between the indenter and the surface of developed alloys, which offers greater resistance to the movement of the indenter. Beyond this region, the COF reaches a steady-state condition with relatively smaller fluctuations owing to the stabilisation of the contact between the indenter and the scratched surface, respectively. An increase in the Cu content from 2 to 6 wt.% exhibits development of hard Ti_2Cu intermetallic formation, which increases resistance against indenter motion and results in high scratch COF.

Figs. 4.10 (a, b, and c) and 4.12b, Table 4.5, the scratch volume increases significantly with an increase in applied load from 5 N to 10 N for all the alloys. The Ti-9Mo-7Nb-2Cu alloy exhibits the maximum scratch volume at 5N and 10N (i.e., 0.0127 and 0.0476 mm^3), while the Ti-9Mo-7Nb-6Cu alloy shows the minimum scratch volume at 5N and 10N (i.e., 0.0077 and

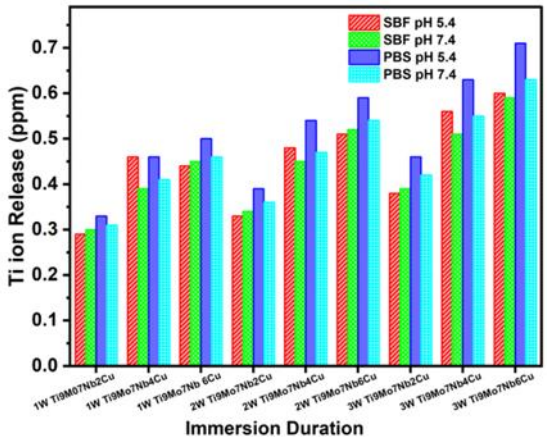
0.0374 mm^3). While the Ti-9Mo-7Nb-4Cu alloy exhibits a scratch volume of 0.0078 and 0.0422 mm^3, both at 5N and 10 N load. This is due to an increase in the Cu content, which decreases the scratch volume and gives the minimum scratch volume in Ti-9Mo-7Nb-6Cu alloy, which attributes to improved load-bearing capacity and enhanced hardness due to the formation of the β-Ti phase and Ti_2Cu intermetallic phase stabilisation. This leads to a smaller scratch track width and depth (shown in Fig. 4.11c), thereby enhancing its scratch volume.

Fig. 4.12c and Table 4.5 show that fracture toughness decreases with an increase in applied load. Ti-9Mo-7Nb-2Cu alloy exhibits the maximum fracture toughness at 5N and 10N (i.e., 118.6 and 109.3 ($\times 10^{1.5}$ MPa-$mm^{0.5}$)), while the Ti-9Mo-7Nb-6Cu alloy has the minimum fracture toughness at 5N and 10N (i.e., 111.8 and 101.5 ($\times 10^{1.5}$ MPa-$mm^{0.5}$)), While, the Ti-9Mo-7Nb-4Cu alloy exhibits a fracture toughness of 116.2 and 106. ($\times 10^{1.5}$ MPa-$mm^{0.5}$), both at 5N and 10 N load. At 10N applied load. the fracture toughness decreases due to the increase in scratch depth. This is due to the fact that scratch depth is inversely proportional to the 1.5 power (from Eq.7); an increase in penetration depth reduces the fracture toughness.

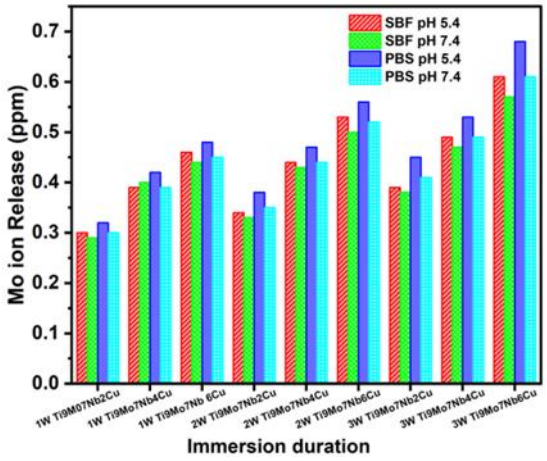
Fig. 22d and Table 6, the variation of scratch hardness with applied load of 5N and 10N. Ti-9Mo-7Nb-6Cu alloy exhibits the maximum scratch hardness both at 5N and 10N load (i.e., 397.4 MPa and 303 MPa), followed by Ti-9Mo-7Nb-4Cu alloy and minimum scratch hardness in Ti-9Mo-7Nb-2Cu alloy. This is due to the formation of Ti_2Cu intermetallic at higher Cu content (i.e., 6 wt.%), which increases its scratch hardness, and scratch hardness decreases at higher applied load due to an increase in its scratch width with applied load as scratch hardness is inversely proportional to the square of scratch track width (from Eq.5).

4.10 Results of metallic ion release

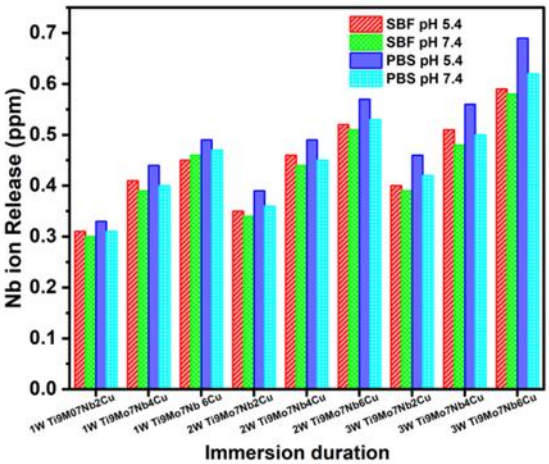
Fig. 4.13 represents a bar graph showing the amount of metallic ion release from the multilayer deposition of Ti-9Mo-7Nb-2Cu, Ti-9Mo-7Nb-4Cu, and Ti-9Mo-7Nb-6Cu alloys at pH 5.4 and 7.4 in SBF and PBS solution for immersion durations of 1, 2, and 3 weeks: (a) Ti, (b) Mo, (c) Nb, and (d) Cu.


SBF pH 5.4
SBF pH 7.4
PBS pH 5.4
PBS pH 7.4
Ti ion Release (ppm)
0.0
0.1
0.2
0.3
0.4
0.5
0.6
0.7
1W Ti9M07Nb2Cu
1W Ti9Mo7Nb4Cu
1W Ti9Mo7Nb 6Cu
2W Ti9Mo7Nb2Cu
2W Ti9Mo7Nb4Cu
2W Ti9Mo7Nb6Cu
3W Ti9Mo7Nb2Cu
3W Ti9Mo7Nb4Cu
3W Ti9Mo7Nb6Cu
Immersion Duration

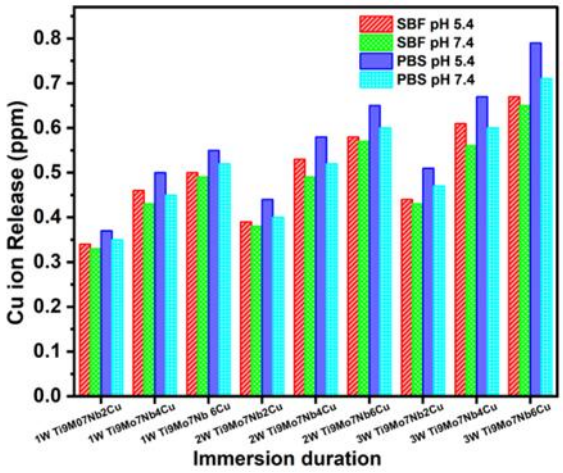
(a)


SBF pH 5.4
SBF pH 7.4
PBS pH 5.4
PBS pH 7.4
Mo ion Release (ppm)
0.0
0.1
0.2
0.3
0.4
0.5
0.6
0.7
1W Ti9M07Nb2Cu
1W Ti9Mo7Nb4Cu
1W Ti9Mo7Nb 6Cu
2W Ti9Mo7Nb2Cu
2W Ti9Mo7Nb4Cu
2W Ti9Mo7Nb6Cu
3W Ti9Mo7Nb2Cu
3W Ti9Mo7Nb4Cu
3W Ti9Mo7Nb6Cu
Immersion duration

(b)


SBF pH 5.4
SBF pH 7.4
PBS pH 5.4
PBS pH 7.4
Nb ion Release (ppm)
0.0
0.1
0.2
0.3
0.4
0.5
0.6
0.7
1W Ti9M07Nb2Cu
1W Ti9Mo7Nb4Cu
1W Ti9Mo7Nb 6Cu
2W Ti9Mo7Nb2Cu
2W Ti9Mo7Nb4Cu
2W Ti9Mo7Nb6Cu
3W Ti9Mo7Nb2Cu
3W Ti9Mo7Nb4Cu
3W Ti9Mo7Nb6Cu
Immersion duration

(c)



(d)

Fig 4.13: *Released amounts of metallic ions of constituent elements (a) Ti, (b) Mo, (c) Nb, and (d) Cu at pH 5.4 and 7.4 in SBF and PBS solution for immersion durations of 1, 2, and 3 weeks.*

Table 4.6: *presents the released amounts of metallic ions Ti, Mo, Nb, and Cu at pH 5.4 and 7.4 in SBF and PBS solutions with immersion duration, i.e., 1 to 3 weeks for Ti-9Mo-7Nb-2Cu, Ti-9Mo-7Nb-4Cu, and Ti-9Mo-7Nb-6Cu alloys*

Alloy type	**Medium**	**Time (weeks)**	**Ti (ppm)**	**Mo (ppm)**	**Nb (ppm)**	**Cu (ppm)**
Ti-9Mo-7Nb-2Cu	SBF 5.4	1	0.29	0.3	0.31	0.34
		2	0.33	0.34	0.35	0.39
		3	0.38	0.39	0.4	0.44
	SBF 7.4	1	0.3	0.29	0.3	0.33
		2	0.34	0.33	0.34	0.38
		3	0.39	0.38	0.39	0.43
	PBS 5.4	1	0.33	0.32	0.33	0.37
		2	0.39	0.38	0.39	0.44
		3	0.46	0.45	0.46	0.51
	PBS 7.4	1	0.31	0.3	0.31	0.35
		2	0.36	0.35	0.36	0.4
		3	0.42	0.41	0.42	0.47

Ti-9Mo-7Nb-4Cu	SBF 5.4	1	0.46	0.39	0.41	0.46
		2	0.48	0.44	0.46	0.53
		3	0.56	0.49	0.51	0.61
	SBF 7.4	1	0.39	0.4	0.39	0.43
		2	0.45	0.43	0.44	0.49
		3	0.51	0.47	0.48	0.56
	PBS 5.4	1	0.46	0.42	0.44	0.5
		2	0.54	0.47	0.49	0.58
		3	0.63	0.53	0.56	0.67
	PBS 7.4	1	0.41	0.39	0.4	0.45
		2	0.47	0.44	0.45	0.52
		3	0.55	0.49	0.5	0.6
Ti-9Mo-7Nb-6Cu	SBF 5.4	1	0.44	0.46	0.45	0.5
		2	0.51	0.53	0.52	0.58
		3	0.6	0.61	0.59	0.67
	SBF 7.4	1	0.45	0.44	0.46	0.49
		2	0.52	0.5	0.51	0.57
		3	0.59	0.57	0.58	0.65
	PBS 5.4	1	0.5	0.48	0.49	0.55
		2	0.59	0.56	0.57	0.65
		3	0.71	0.68	0.69	0.79
	PBS 7.4	1	0.46	0.45	0.47	0.52
		2	0.54	0.52	0.53	0.6
		3	0.63	0.61	0.62	0.71

From Fig. 4.13 (a-d), the released amounts of metallic ions (i.e., Ti, Mo, Nb, and Cu) increase gradually at pH 5.4 and 7.4 in SBF and PBS solution with immersion duration, i.e., 1 to 3 weeks for Ti-9Mo-7Nb-2Cu, Ti-9Mo-7Nb-4Cu, and Ti-9Mo-7Nb-6Cu alloys. The above explanation arises due to the effective interaction of the metal surface and the biofluids (i.e., SBF and PBS). Additionally, the release of metallic ions is comparatively higher in 5.4 pH than in 7.4 pH.

It can be observed from Fig. 4.13a and Table 4.6 that the Ti-9Mo-7Nb-6Cu alloy exhibits the maximum release of metallic ions. The maximum amount of Ti ion release is observed after 3 weeks of immersion in pH 7.4 PBS, which is 0.71 ppm, whereas the minimum amount of Ti ion release is obtained for Ti-9Mo-7Nb-2Cu alloy after 1 week of immersion in pH 5.4 SBF, which is nearly 0.28 ppm.

Fig. 4.13b and Table 4.6 show that the minimum amount of release of Mo ions is 0.29 ppm in the Ti-9Mo-7Nb-4Cu alloy at 7.4pH SBF for a 1-week duration, and the maximum amount of release of Mo ions is 0.68 ppm in the Ti-9Mo-7Nb-6Cu alloy at 5.4pH PBS for a 3-week duration. It can be observed that the controlled release of Mo ions indicates good chemical stability of the β-phase stabilised in both PBS and SBF at pH 5.4 and 7.4 in SBF and PBS solution for all durations.

Fig. 4.13c and Table 4.6, show that the minimum amount of release of Nb ions is 0.3 ppm in the Ti-9Mo-7Nb-2Cu alloy at 7.4pH SBF for a 1-week duration, and the maximum amount of release is 0.69 ppm in the Ti-9Mo-7Nb-6Cu alloy at 5.4pH PBS for a 3-week duration. The lower release of Nb ions indicates good β-phase stability in both PBS and SBF at pH 5.4 and 7.4 in SBF and PBS solution for all durations.

Fig. 4.13d and Table 4.6, show that the minimum amount of release of Cu ions is 0.3 ppm in the Ti-9Mo-7Nb-2Cu alloy at 7.4pH SBF for a 1-week duration, and the maximum amount of release is 0.79 ppm in the Ti-9Mo-7Nb-6Cu alloy at 5.4pH PBS for a 3-week duration. The lower release of Cu ions indicates good β-phase stability in both PBS and SBF at pH 5.4 and 7.4 in SBF and PBS solution for all durations. An increase in the amount of Cu ions released is due to the partial dissolution of Ti_2Cu intermetallic compounds during prolonged immersion. However, the obtained Cu ion release values remain within acceptable limits for biomedical applications and may contribute beneficial antibacterial activity.

4.11 Results of cell viability and cell adhesion

Fig. 4.14 presents the cell viability using the L929 fibroblast cell line for incubation durations of 2,4, and 6 days in developed Ti-9Mo-7Nb-2Cu, Ti-9Mo-7Nb-4Cu, and Ti-9Mo-7Nb-6Cu alloys.

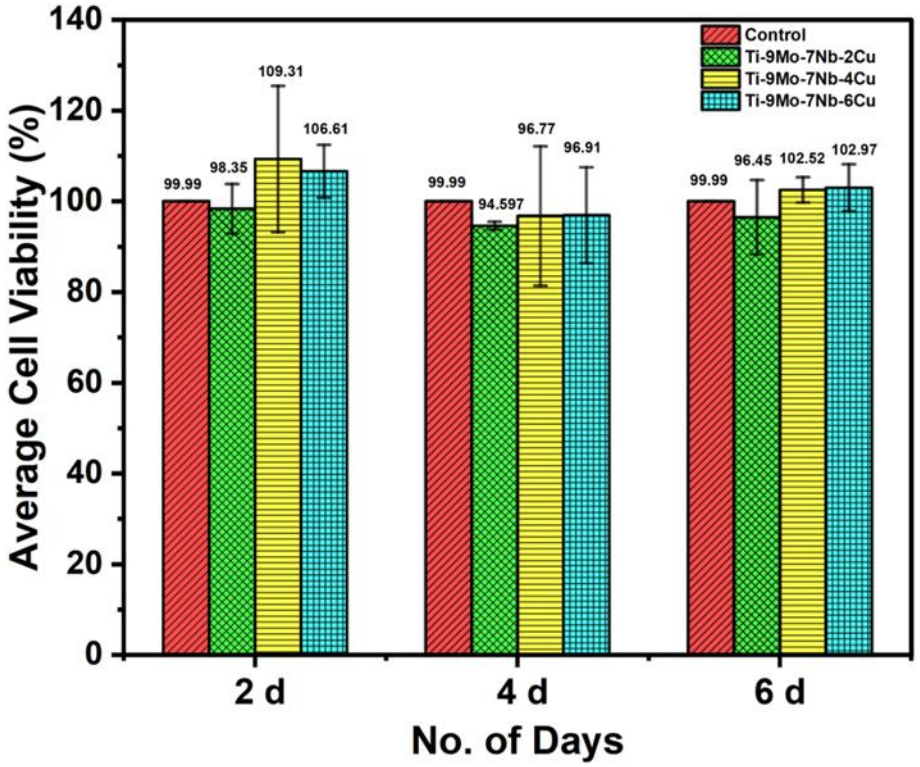


Fig 4.14: *Viability of L929 fibroblast cells at different incubation durations of 2,4, and 6 days in the developed Ti-9Mo-7Nb-2Cu, Ti-9Mo-7Nb-4Cu, and Ti-9Mo-7Nb-6Cu alloys*

From Fig. 4.14, the average cell viability of the control for all durations is 99.99%. For 2 days, the Ti-9Mo-7Nb-2Cu alloy shows an average cell viability of 98.35%, whereas higher cell viability was observed in the Ti-9Mo-7Nb-4Cu alloy (i.e., 109.31%) and 106.61% in the Ti-9Mo-7Nb-6Cu alloy with respect to the control. The increased cell viability observed for the Ti-9Mo-7Nb-4Cu and Ti-9Mo-7Nb-4Cu alloys indicates enhanced cell viability and metabolic activity in the Ti-9Mo-7Nb-4Cu and Ti-9Mo-7Nb-6Cu alloys. The higher cell viability in Ti-9Mo-7Nb-4Cu and Ti-9Mo-7Nb-6Cu alloys observed after 2 days may be attributed to the sufficient availability of nutrients, growth factors, and serum components present in the culture medium supplied to the cells during the initial incubation stage. During this period, the cells remain metabolically active and receive adequate nourishment for growth and proliferation, resulting in high mitochondrial activity measured through the MTT assay. Furthermore, the developed alloy extracts did not produce any toxic effect that could inhibit nutrient uptake or cellular metabolism, thereby maintaining excellent cell viability.

For the 4-day incubation period, the Ti-9Mo-7Nb-2Cu alloy exhibited the minimum average cell viability of 94.59%, whereas the Ti-9Mo-7Nb-4Cu and Ti-9Mo-7Nb-6Cu alloys showed comparatively higher cell viability values of 96.77% and 96.91%, respectively. Although a slight reduction in cell viability was observed compared to the 2-day incubation period, average cell viability values were well above the acceptable limit, confirming their non-cytotoxic nature and good biocompatibility.

After 6 days of incubation, the average cell viability increased again for Ti-9Mo-7Nb-4Cu and Ti-9Mo-7Nb-6Cu alloys, which is 102.52% and 102.97% as compared to 96.45% in Ti-9Mo-7Nb-2Cu alloy. This contributes to the increase in the Cu content, which improves densification and reduces porosity and prevents the release of harmful degradation products, thereby promoting better cellular response and enhanced surface bioactivity. In addition, the formation of a stable passive TiO_2 oxide layer in the developed alloy surface, which minimises the excessive release of metallic ions into the surrounding medium.

4.12 Cell adhesion and its morphology analysis

Fig. 4.15 shows images of cell adhesion using Calcein AM dye for the live cells (shown in green colour) and Propidium Iodide dye for dead cells (shown in red colour) in developed Ti-9Mo-7Nb-2Cu, Ti-9Mo-7Nb-4Cu, and Ti-9Mo-7Nb-6Cu alloys using fluorescence microscopy. Fig 4.16 shows cell morphology using L929 fibroblast cell lines on the surface of developed Ti-9Mo-7Nb-2Cu, Ti-9Mo-7Nb-4Cu, and Ti-9Mo-7Nb-6Cu alloys at different magnifications.

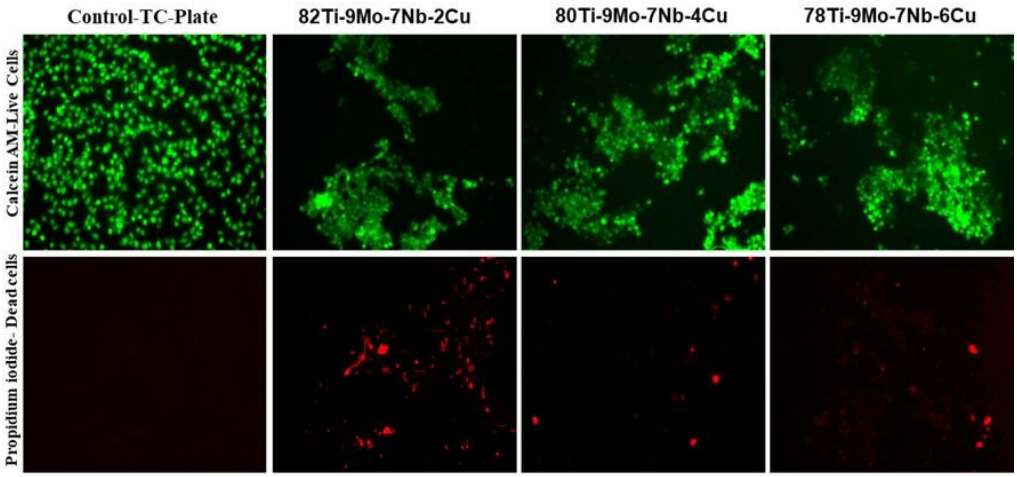


Fig 4.15: *Fluorescence microscopic images depicting cell adhesion to the samples of Ti-9Mo-7Nb-2Cu, Ti-9Mo-7Nb-4Cu, and Ti-9Mo-7Nb-6Cu and the control using Calcein AM dye for the live cells (shown green colour) and Propidium Iodide dye for dead cells (shown red colour).*

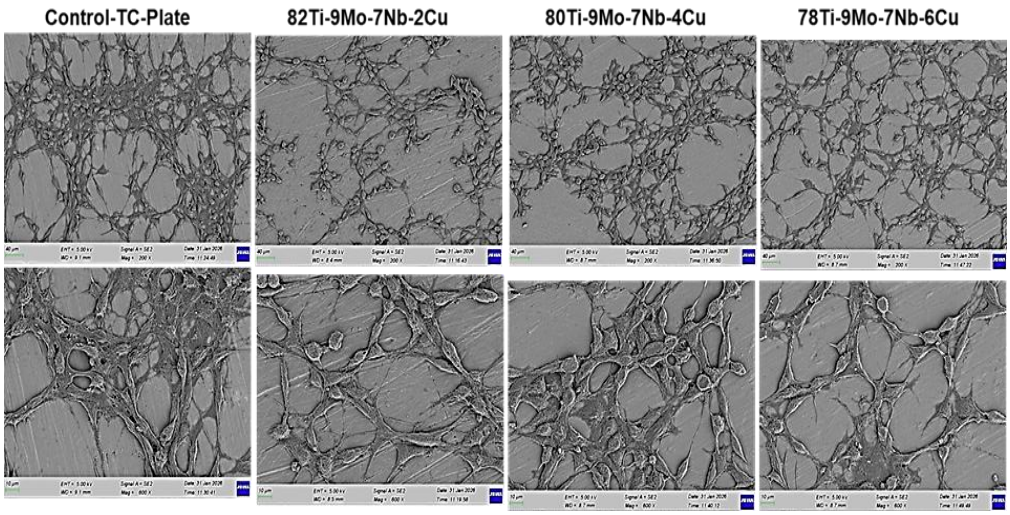


Fig 4.16: *SEM images showing adhesion and morphology of L929 fibroblast cells on Ti-9Mo-7Nb-2Cu, Ti-9Mo-7Nb-4Cu, and Ti-9Mo-7Nb-6Cu and the control surfaces at different magnifications.*

From Figs. 4.15, it can be observed that the control TC plate exhibits the highest density of green fluorescence with negligible red fluorescence, indicating excellent fibroblast cell viability. Ti-9Mo-7Nb-4Cu and Ti-9Mo-7Nb-6Cu alloys exhibited comparatively higher live cell density and lower dead cell population compared to the Ti-9Mo-7Nb-2Cu alloy (shown in Fig. 4.16). This behaviour indicates improved cell–material interaction and enhanced cellular activity for the higher Cu-containing alloys. The improved cellular response may be attributed to the denser microstructure, reduced porosity, improved surface homogeneity, and enhanced surface characteristics observed in the higher Cu-containing alloys. Furthermore, the limited red fluorescence observed for the Ti-9Mo-7Nb-4Cu and Ti-9Mo-7Nb-6Cu alloys suggests that Cu addition favours the growth of cells, confirming excellent biocompatibility and cell viability. Ti-9Mo-7Nb-2Cu alloy exhibited comparatively more red fluorescent spots, indicating a slightly higher dead cell population (shown in Fig. 4.16), which may be associated with its comparatively higher porosity and less homogeneous surface morphology. However, the overall dead cell population remained very low, confirming that the non-cytotoxic nature of the Ti-9Mo-7Nb-2Cu alloy.

4.13 Results of bacterial inhibitory test

Figs. 4.17 and 4.18 present the morphologies of *E. coli* bacteria incubated for a duration of 24 hours and their bar graphs showing the antibacterial rate in the developed Ti-9Mo-7Nb-2Cu, Ti-9Mo-7Nb-4Cu, and Ti-9Mo-7Nb-6Cu alloys.

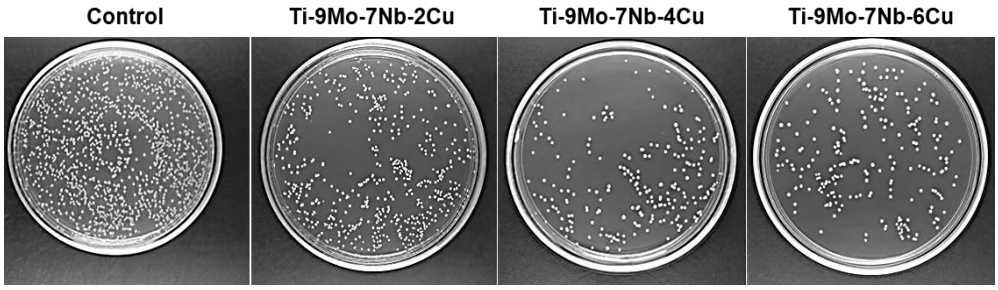


Fig 4.17: *Morphologies of E. coli bacteria correspond to Ti-9Mo-7Nb-2Cu, Ti-9Mo-7Nb-4Cu, and Ti-9Mo-7Nb-6Cu alloys*

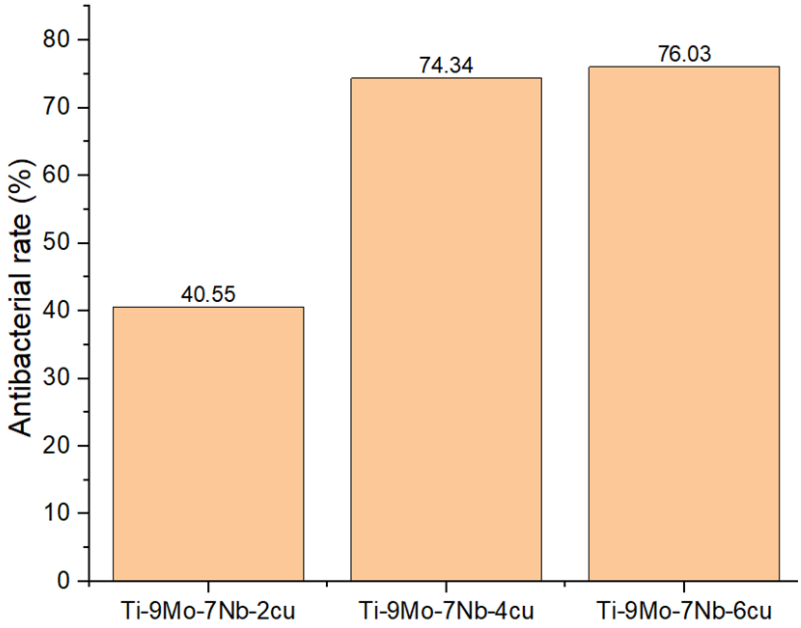


Fig 4.18: *Bar graph representing the antibacterial rate against E. coli of the developed Ti–9Mo–7Nb–2Cu, Ti–9Mo–7Nb–4Cu, and Ti–9Mo–7Nb–6Cu alloys.*

It can be observed that from Fig. 4.18, the Ti-9Mo-7Nb-6Cu alloy exhibited a maximum antibacterial rate of 76.03%, and the Ti-9Mo-7Nb-2Cu alloy showed a minimum antibacterial rate of 40.55 %, whereas the moderate antibacterial rate of 74.34% is evident in the Ti-9Mo-7Nb-2Cu alloy.

An increase in the Cu content from 2 to 6 wt.% enhanced its antibacterial performance, evident from its morphologies in Fig. 4.17. This is due to the antibacterial properties of Cu, which interact with the bacterial cell membrane, causing membrane disruption, oxidative stress, protein denaturation, and damage to intracellular components, ultimately leading to bacterial cell death. Therefore, Ti-9Mo-7Nb-6Cu alloy suggests its strong potential for biomedical implant applications where prevention of bacterial infection is critically important.

Chapter 5

Conclusion

This thesis presents the design and studies the effects of adding Cu (i.e., 2, 4, and 6 wt.%) in Ti-9Mo-7Nb alloy developed by μ-PPAM process on phase diagram and Scheil solidification, density, porosity, microstructure, evolution of phases, microhardness, tensile strength and its fractography, compressive strength, fracture toughness and abrasion resistance, and its *in-vitro* biocompatibility on Cell viability and cell adhesion, release of metallic ions, and bacteria inhibitory properties. The following are the major findings of this work:

- Porosity of the alloys decreases in the order: Ti-9Mo-7Nb-2Cu > Ti-9Mo-7Nb-4Cu > Ti-9Mo-7Nb-6Cu. This reduction is attributed to improved filling of interlayer gaps by Cu, which enhances densification and minimizes pore formation and lack-of-fusion defects.
- XRD analysis confirms the presence of α-Ti (HCP), β-Ti (BCC), TiO_2, and Ti_2Cu phases in all alloys. With increasing Cu content, Ti_2Cu peak intensity increases due to limited Cu solubility and intermetallic precipitation, while α-phase intensity decreases, indicating enhanced β-phase stabilization at higher Cu levels.
- Microstructural analysis reveals a β-Ti matrix with α-Ti, TiO_2, and Ti_2Cu phases in all alloys. Increasing Cu content enhances Ti_2Cu formation, improves β-phase stability, and reduces porosity, resulting in a denser and more refined microstructure in Ti-9Mo-7Nb-6Cu alloy.
- Microhardness increases with Cu content, reaching a maximum in Ti-9Mo-7Nb-6Cu alloy. This is attributed to increased Ti_2Cu intermetallic formation, microstructural refinement, solid solution strengthening, and reduced porosity.
- Tensile properties improve with increasing Cu content, with Ti-9Mo-7Nb-6Cu alloy showing the highest strength and elongation. This is due to increased Ti_2Cu precipitation, microstructural refinement, and reduced porosity, which enhance load-bearing capacity and delay crack initiation.
- Compressive strength increases with Cu content, with Ti-9Mo-7Nb-6Cu alloy showing the highest strength but reduced deformation. This is due to microstructural refinement,

increased Ti_2Cu precipitation, and β-phase stabilization, which enhance resistance to deformation while limiting plasticity.

- Scratch behavior shows that COF increases with load and Cu content, while scratch volume decreases with increasing Cu, indicating improved wear resistance. Ti-9Mo-7Nb-6Cu alloy exhibits the highest scratch hardness but lowest fracture toughness due to increased Ti_2Cu intermetallic formation and higher resistance to deformation.
- Metallic ion release increases with immersion time and is higher at pH 5.4, with Ti-9Mo-7Nb-6Cu alloy showing the maximum release. This is attributed to partial dissolution of Ti_2Cu phases; however, ion release remains within acceptable limits, indicating good chemical stability and potential antibacterial benefits.
- All alloys exhibit excellent biocompatibility with high cell viability (>94%), with Ti-9Mo-7Nb-4Cu and Ti-9Mo-7Nb-6Cu showing comparatively higher viability due to improved densification, reduced porosity, and stable TiO_2 layer formation that enhances cellular response.
- Antibacterial activity increases with Cu content, with Ti-9Mo-7Nb-6Cu alloy showing the highest antibacterial rate. This is attributed to the antibacterial nature of Cu, which disrupts bacterial cells, indicating strong potential for biomedical implant applications.

  Increasing Cu content in Ti-9Mo-7Nb alloys reduces porosity and improves densification, leading to a more refined β-Ti matrix with enhanced Ti_2Cu intermetallic formation and β-phase stability. This results in higher microhardness, improved tensile and compressive strength, and better wear resistance, although ductility and fracture toughness decrease at higher Cu levels. XRD confirms the presence of α-Ti, β-Ti, TiO_2, and Ti_2Cu phases, with Ti_2Cu intensity increasing as Cu content rises. Ion release is slightly higher with more Cu, especially in acidic conditions, but remains within acceptable limits. All alloys exhibit excellent biocompatibility, while antibacterial activity significantly improves with increasing Cu, making Ti-9Mo-7Nb-6Cu the most promising composition for biomedical applications.

Chapter 6

REFERENCES

[1] "ISO/ASTM 52900:2021(en), Additive manufacturing — General principles — Fundamentals and vocabulary." Accessed: May 27, 2026. [Online]. Available: https://www.iso.org/obp/ui/#iso:std:iso-astm:52900:ed-2:v1:en

[2] M. Koltsaki and M. Mavri, "A Comprehensive Overview of Additive Manufacturing Processes Through a Time-Based Classification Model," *3D Print. Addit. Manuf.*, vol. 11, no. 1, pp. 363–382, Feb. 2024, doi: 10.1089/3DP.2022.0167;WGROUP:STRING:PUBLICATION.

[3] R. Banerjee, P. C. Collins, D. Bhattacharyya, S. Banerjee, and H. L. Fraser, "Microstructural evolution in laser deposited compositionally graded α/β titanium-vanadium alloys," *Acta Mater.*, vol. 51, no. 11, pp. 3277–3292, Jan. 2003, doi: 10.1016/S1359-6454(03)00158-7.

[4] F. Calignano *et al.*, "Overview on additive manufacturing technologies," *Proceedings of the IEEE*, vol. 105, no. 4, pp. 593–612, 2017, doi: 10.1109/JPROC.2016.2625098.

[5] T. DebRoy *et al.*, "Additive manufacturing of metallic components – Process, structure and properties," *Prog. Mater. Sci.*, vol. 92, pp. 112–224, Mar. 2018, doi: 10.1016/J.PMATSCI.2017.10.001.

[6] H. Geng, J. Li, J. Xiong, and X. Lin, "Optimisation of interpass temperature and heat input for wire and arc additive manufacturing 5A06 aluminium alloy," *Science and Technology of Welding and Joining*, vol. 22, no. 6, pp. 472–483, Aug. 2017, doi: 10.1080/13621718.2016.1259031;PAGE:STRING:ARTICLE/CHAPTER.

[7] J. D. Spencer, P. M. Dickens, and C. M. Wykes, "Rapid prototyping of metal parts by three-dimensional welding," *Proc. Inst. Mech. Eng. B J. Eng. Manuf.*, vol. 212, no. 3, pp. 175–182, 1998, doi: 10.1243/0954405981515590;ISSUE:ISSUE:DOI.

[8] Y. M. Zhang, Y. Chen, P. Li, and A. T. Male, "Weld deposition-based rapid prototyping: a preliminary study," *J. Mater. Process. Technol.*, vol. 135, no. 2–3, pp. 347–357, Apr. 2003, doi: 10.1016/S0924-0136(02)00867-1.

[9] M. S. Sawant and N. K. Jain, "Investigations on additive manufacturing of Ti-6Al-4V by microplasma transferred arc powder deposition process," *Journal of Manufacturing*

Science and Engineering, Transactions of the ASME, vol. 140, no. 8, Aug. 2018, doi: 10.1115/1.4040324/377641.

[10] M. S. Sawant and N. K. Jain, "Characteristics of Single-Track and Multi-track Depositions of Stellite by Micro-plasma Transferred Arc Powder Deposition Process," *Journal of Materials Engineering and Performance 2017 26:8*, vol. 26, no. 8, pp. 4029–4039, Jul. 2017, doi: 10.1007/S11665-017-2828-Y.

[11] S. Jhavar, N. K. Jain, and C. P. Paul, "Development of micro-plasma transferred arc (μ-PTA) wire deposition process for additive layer manufacturing applications," *J. Mater. Process. Technol.*, vol. 214, no. 5, pp. 1102–1110, May 2014, doi: 10.1016/J.JMATPROTEC.2013.12.016.

[12] M. Terakubo, J. Oh, S. Kirihara, Y. Miyamoto, K. Matsuura, and M. Kudoh, "Freeform fabrication of titanium metal by 3D micro welding," *Materials Science and Engineering: A*, vol. 402, no. 1–2, pp. 84–91, Aug. 2005, doi: 10.1016/J.MSEA.2005.04.025.

[13] J. L. Cann *et al.*, "Sustainability through alloy design: Challenges and opportunities," *Prog. Mater. Sci.*, vol. 117, p. 100722, Apr. 2021, doi: 10.1016/J.PMATSCI.2020.100722.

[14] A. Moridi *et al.*, "Solid-state additive manufacturing of porous Ti-6Al-4V by supersonic impact," *Appl. Mater. Today*, vol. 21, p. 100865, Dec. 2020, doi: 10.1016/J.APMT.2020.100865.

[15] S. A. Salihu, Y. I. Suleiman, A. I. Eyinavi, and A. Usman, "Classification, Properties and Applications of titanium and its alloys used in aerospace, automotive, biomedical and marine industry-A Review," *International Journal of Precious Engineering Research and Applications (IJPERA) www.ijpera.com*, vol. 4, no. 3, pp. 23–36, Accessed: May 27, 2026. [Online]. Available: www.ijpera.com

[16] P. K. Arya, P. M. Pandey, N. K. Jain, D. Sathiaraj, M. S. Sawant, and A. Srivastava, "Recent advances in strengthening titanium alloys through alloying elements," *Advanced Composites and Hybrid Materials 2026 9:3*, vol. 9, no. 3, pp. 225-, Apr. 2026, doi: 10.1007/S42114-025-01577-7.

[17] K. U. Yazar, S. Mishra, A. Karmakar, A. Bhattacharjee, and S. Suwas, "On the Temperature Sensitivity of Dwell Fatigue of a Near Alpha Titanium Alloy: Role of Strain Hardening and Strain Rate Sensitivity," *Metallurgical and Materials Transactions A*

2020 51:10, vol. 51, no. 10, pp. 5036–5042, Aug. 2020, doi: 10.1007/S11661-020-05914-X.

[18] W. Jia, W. Zeng, and H. Yu, "Effect of aging on the tensile properties and microstructures of a near-alpha titanium alloy," *Mater. Des.*, vol. 58, pp. 108–115, Jun. 2014, doi: 10.1016/J.MATDES.2014.01.063.

[19] Y. Zhang *et al.*, "Improved rotating bending fatigue performance of laser directed energy deposited Ti6Al4V alloys by laser shock peening," *J. Alloys Compd.*, vol. 980, p. 173664, Apr. 2024, doi: 10.1016/J.JALLCOM.2024.173664.

[20] J. C. Williams and R. R. Boyer, "Opportunities and Issues in the Application of Titanium Alloys for Aerospace Components," *Metals 2020, Vol. 10, Page 705*, vol. 10, no. 6, p. 705, May 2020, doi: 10.3390/MET10060705.

[21] P. Barriobero-Vila, G. Requena, T. Buslaps, M. Alfeld, and U. Boesenberg, "Role of element partitioning on the α–β phase transformation kinetics of a bi-modal Ti–6Al–6V–2Sn alloy during continuous heating," *J. Alloys Compd.*, vol. 626, pp. 330–339, Mar. 2015, doi: 10.1016/J.JALLCOM.2014.11.176.

[22] R. Naseri *et al.*, "An Investigation into the Microstructural Response to Flexural Stresses of a Metastable β-Phase Ti Alloy produced by Blended Elemental Powder Metallurgy," *Adv. Eng. Mater.*, vol. 26, no. 4, p. 2300350, Feb. 2024, doi: 10.1002/ADEM.202300350;REQUESTEDJOURNAL:JOURNAL:15272648;CSUBTYPE:STRING:SPECIAL;PAGE:STRING:ARTICLE/CHAPTER.

[23] A. C. Arohi, S. Shekhar, and I. Sen, "Effect of thermomechanical processing on microstructure evolution and mechanical properties of metastable β Ti–5Al–5V–5Mo–3Cr alloy," *Mater. Chem. Phys.*, vol. 314, p. 128809, Feb. 2024, doi: 10.1016/J.MATCHEMPHYS.2023.128809.

[24] C. J. Bettles, D. Tomus, and M. A. Gibson, "The role of microstructure in the mechanical behaviour of Ti–1.6 wt.%Fe alloys containing O and N," *Materials Science and Engineering: A*, vol. 528, no. 15, pp. 4899–4909, Jun. 2011, doi: 10.1016/J.MSEA.2011.03.030.

[25] R. P. Kolli and A. Devaraj, "A Review of Metastable Beta Titanium Alloys," *Metals 2018, Vol. 8, Page 506*, vol. 8, no. 7, p. 506, Jun. 2018, doi: 10.3390/MET8070506.

[26] A. Kaouka, K. Benarous, A. Daas, and S. A. Tsipas, “The Effects of Nb and Mo Addition on Microstructure and Mechanical Behaviour of Ti-6Al-4V Alloy”, doi: 10.18311/jsst/2017/11026.

[27] P. Pesode and S. Barve, “A review—metastable β titanium alloy for biomedical applications,” *Journal of Engineering and Applied Science 2023 70:1*, vol. 70, no. 1, pp. 25-, Apr. 2023, doi: 10.1186/S44147-023-00196-7.

[28] A. Carman, L. C. Zhang, O. M. Ivasishin, D. G. Savvakin, M. V. Matviychuk, and E. V. Pereloma, “Role of alloying elements in microstructure evolution and alloying elements behaviour during sintering of a near-β titanium alloy,” *Materials Science and Engineering: A*, vol. 528, no. 3, pp. 1686–1693, Jan. 2011, doi: 10.1016/J.MSEA.2010.11.004.

[29] S. Sui, Y. Chew, F. Weng, C. Tan, Z. Du, and G. Bi, “Achieving grain refinement and ultrahigh yield strength in laser aided additive manufacturing of Ti−6Al−4V alloy by trace Ni addition,” *Virtual Phys. Prototyp.*, vol. 16, no. 4, pp. 417–427, Jul. 2021, doi: 10.1080/17452759.2021.1949091.

[30] Y. Zhuo, C. Yang, C. Fan, and S. Lin, “Effects of trace Sn and Cr addition on microstructure and mechanical properties of TC17 titanium alloy repaired by wire arc additive manufacturing,” *J. Alloys Compd.*, vol. 888, p. 161473, Dec. 2021, doi: 10.1016/J.JALLCOM.2021.161473.

[31] C. Xia *et al.*, “Effect of zirconium content on the microstructure and corrosion behavior of Ti-6Al-4V-xZr alloys,” *Corros. Sci.*, vol. 112, pp. 687–695, Nov. 2016, doi: 10.1016/J.CORSCI.2016.09.012.

[32] J. Xu *et al.*, “Surface Modification of Biomedical Ti and Ti Alloys: A Review on Current Advances,” *Materials 2022, Vol. 15, Page 1749*, vol. 15, no. 5, p. 1749, Feb. 2022, doi: 10.3390/MA15051749.

[33] L. C. Zhang, L. Y. Chen, and L. Wang, “Surface Modification of Titanium and Titanium Alloys: Technologies, Developments, and Future Interests,” *Adv. Eng. Mater.*, vol. 22, no. 5, p. 1901258, May 2020, doi: 10.1002/ADEM.201901258;WGROUP:STRING:PUBLICATION.

[34] Y. Liu *et al.*, “Dynamic compressive properties and underlying failure mechanisms of selective laser melted Ti-6Al-4V alloy under high temperature and strain rate

conditions," *Addit. Manuf.*, vol. 54, p. 102772, Jun. 2022, doi: 10.1016/J.ADDMA.2022.102772.

[35] Y. Meng *et al.*, "Thermochemical surface hardening of Ti-6Al-4V: On the role of temperature and treatment media," *Surf. Coat. Technol.*, vol. 422, p. 127505, Sep. 2021, doi: 10.1016/J.SURFCOAT.2021.127505.

[36] L. C. Zhang and L. Y. Chen, "A Review on Biomedical Titanium Alloys: Recent Progress and Prospect," *Adv. Eng. Mater.*, vol. 21, no. 4, p. 1801215, Apr. 2019, doi: 10.1002/ADEM.201801215;REQUESTEDJOURNAL:JOURNAL:15272648;PAGE:STRING:ARTICLE/CHAPTER.

[37] C. Zhang and M. C. Gao, "CALPHAD modeling of high-entropy alloys," *High-Entropy Alloys: Fundamentals and Applications*, pp. 399–444, Jan. 2016, doi: 10.1007/978-3-319-27013-5_12/SAVE-RESEARCH.

[38] D. B. Miracle, J. D. Miller, O. N. Senkov, C. Woodward, M. D. Uchic, and J. Tiley, "Exploration and Development of High Entropy Alloys for Structural Applications," *Entropy 2014, Vol. 16, Pages 494-525*, vol. 16, no. 1, pp. 494–525, Jan. 2014, doi: 10.3390/E16010494.

[39] O. N. Senkov, S. V. Senkova, C. Woodward, and D. B. Miracle, "Low-density, refractory multi-principal element alloys of the Cr-Nb-Ti-V-Zr system: Microstructure and phase analysis," *Acta Mater.*, vol. 61, no. 5, pp. 1545–1557, Mar. 2013, doi: 10.1016/J.ACTAMAT.2012.11.032.

[40] Z. Liu, B. He, T. Lyu, and Y. Zou, "A Review on Additive Manufacturing of Titanium Alloys for Aerospace Applications: Directed Energy Deposition and Beyond Ti-6Al-4V," *JOM 2021 73:6*, vol. 73, no. 6, pp. 1804–1818, Apr. 2021, doi: 10.1007/S11837-021-04670-6.

[41] E. Fereiduni, A. Ghasemi, and M. Elbestawi, "Selective Laser Melting of Aluminum and Titanium Matrix Composites: Recent Progress and Potential Applications in the Aerospace Industry," *Aerospace 2020, Vol. 7, Page 77*, vol. 7, no. 6, p. 77, Jun. 2020, doi: 10.3390/AEROSPACE7060077.

[42] Y. Li, C. Yang, H. Zhao, S. Qu, X. Li, and Y. Li, "New Developments of Ti-Based Alloys for Biomedical Applications," *Materials 2014, Vol. 7, Pages 1709-1800*, vol. 7, no. 3, pp. 1709–1800, Mar. 2014, doi: 10.3390/MA7031709.

[43] D. Rugg, M. Dixon, and J. Burrows, “High-temperature application of titanium alloys in gas turbines. Material life cycle opportunities and threats – an industrial perspective,” *Materials at High Temperatures*, vol. 33, no. 4–5, pp. 536–541, Jun. 2016, doi: 10.1080/09603409.2016.1184423.

[44] A. S. Oryshchenko, I. V. Gorynin, V. P. Leonov, A. S. Kudryavtsev, V. I. Mikhailov, and E. V. Chudakov, “Marine titanium alloys: Present and future,” *Inorganic Materials: Applied Research*, vol. 6, no. 6, pp. 571–579, Nov. 2015, doi: 10.1134/S2075113315060106/METRICS.

[45] Y. Li *et al.*, “Investigation on Wear Behavior of Cryogenically Treated Ti-6Al-4V Titanium Alloy under Dry and Wet Conditions,” *Materials 2019, Vol. 12, Page 2850*, vol. 12, no. 18, p. 2850, Sep. 2019, doi: 10.3390/MA12182850.

[46] I. Gibson, D. Rosen, B. Stucker, and M. Khorasani, “Additive manufacturing technologies,” *Additive Manufacturing Technologies*, pp. 1–675, Nov. 2020, doi: 10.1007/978-3-030-56127-7/SAVE-RESEARCH.

[47] W. E. Frazier, “Metal Additive Manufacturing: A Review,” *Journal of Materials Engineering and Performance 2014 23:6*, vol. 23, no. 6, pp. 1917–1928, Apr. 2014, doi: 10.1007/S11665-014-0958-Z.

[48] S. W. Williams, F. Martina, A. C. Addison, J. Ding, G. Pardal, and P. Colegrove, “Wire + Arc Additive Manufacturing,” *Materials Science and Technology*, vol. 32, no. 7, pp. 641–647, Jun. 2016, doi: 10.1179/1743284715Y.0000000073.

[49] E. Damri, E. Tiferet, D. Braun, Y. I. Ganor, M. Chonin, and I. Orion, “Effects of Gas Pressure during Electron Beam Energy Deposition in the EBM Additive Manufacturing Process,” *Metals 2021, Vol. 11, Page 601*, vol. 11, no. 4, p. 601, Apr. 2021, doi: 10.3390/MET11040601.

[50] V. Osterman, “Vacuum Heat Treating Additively Manufactured Parts,” *Additive Manufacturing Processes*, pp. 324–330, Aug. 2020, doi: 10.31399/ASM.HB.V24.A0006561.

[51] N. Cooper *et al.*, “Additively manufactured ultra-high vacuum chamber below 10^{-10} mbar,” *Addit.Manuf.*, vol. 40, Apr. 2021, doi: 10.1016/J.ADDMA.2021.101898.

[52] X. Wang, C. H. Zhang, X. Cui, S. Zhang, J. Chen, and J. B. Zhang, "Microstructure and mechanical behavior of additive manufactured Cr–Ni–V low alloy steel in different heat treatment," *Vacuum*, vol. 175, May 2020, doi: 10.1016/J.VACUUM.2020.109216.

[53] M. Kühn-Kauffeldt, M. Kühn, N. Perrin, and W. Saur, "Fused filament fabrication of thermoplastics in high vacuum without convective heat transfer," *Sci. Rep.*, vol. 15, no. 1, Dec. 2025, doi: 10.1038/S41598-025-13181-2.

[54] Z. Li *et al.*, "High deposition rate powder- and wire-based laser directed energy deposition of metallic materials: A review," *Int. J. Mach. Tools Manuf.*, vol. 181, Oct. 2022, doi: 10.1016/J.IJMACHTOOLS.2022.103942.

[55] D. Svetlizky *et al.*, "Directed energy deposition (DED) additive manufacturing: Physical characteristics, defects, challenges and applications," *Materials Today*, vol. 49, pp. 271–295, Oct. 2021, doi: 10.1016/j.mattod.2021.03.020.

[56] X. Wang, X. He, T. Wang, and Y. Li, "Internal pores in DED Ti-6.5Al-2Zr-Mo-V alloy and their influence on crack initiation and fatigue life in the mid-life regime," *Addit. Manuf.*, vol. 28, pp. 373–393, Aug. 2019, doi: 10.1016/J.ADDMA.2019.05.007.

[57] A. T. Akono, N. X. Randall, and F. J. Ulm, "Experimental determination of the fracture toughness via microscratch tests: Application to polymers, ceramics, and metals," *J. Mater. Res.*, vol. 27, no. 2, pp. 485–493, Jan. 2012, doi: 10.1557/JMR.2011.402.

[58] L. Wang, J. Yao, Y. Hu, and S. Song, "Suppression effect of a steady magnetic field on molten pool during laser remelting," *Appl. Surf. Sci.*, vol. 351, pp. 794–802, Oct. 2015, doi: 10.1016/J.APSUSC.2015.05.179.

[59] X. M. Zhou *et al.*, "Numerical Simulation and Experimental Investigation of Arc Based Additive Manufacturing Assisted with External Longitudinal Static Magnetic Field," 2015, *University of Texas at Austin*. Accessed: May 28, 2026. [Online]. Available: https://hdl.handle.net/2152/89315

[60] Y. Liu, Q. Sun, J. Liu, S. Wang, and J. Feng, "Effect of axial external magnetic field on cold metal transfer welds of aluminum alloy and stainless steel," *Mater. Lett.*, vol. 152, pp. 29–31, Aug. 2015, doi: 10.1016/j.matlet.2015.03.077.

[61] C. Tan *et al.*, "Review on field assisted metal additive manufacturing," *Int. J. Mach. Tools Manuf.*, vol. 189, Jun. 2023, doi: 10.1016/J.IJMACHTOOLS.2023.104032.

[62] Y. Wang *et al.*, "Effect of magnetic Field on the microstructure and mechanical properties of inconel 625 superalloy fabricated by wire arc additive manufacturing," *J. Manuf. Process.*, vol. 64, pp. 10–19, Apr. 2021, doi: 10.1016/J.JMAPRO.2021.01.008.

[63] R. Zhao *et al.*, "Enhanced mechanical properties of Ti6Al4V alloy fabricated by laser additive manufacturing under static magnetic field," *Mater. Res. Lett.*, vol. 10, no. 8, pp. 530–538, Aug. 2022, doi: 10.1080/21663831.2022.2064195.

[64] H. Zhou *et al.*, "The microstructure and properties evolution of SS316L fabricated by magnetic field-assisted laser powder bed fusion," *Materials Science and Engineering: A*, vol. 845, p. 143216, Jun. 2022, doi: 10.1016/J.MSEA.2022.143216.

[65] Z. Q. Guan, H. X. Zhang, X. G. Liu, A. Babkin, and Y. L. Chang, "Effect of magnetic field frequency on the shape of GMAW welding arc and weld microstructure properties," *Mater. Res. Express*, vol. 6, no. 8, Jun. 2019, doi: 10.1088/2053-1591/AB2572.

[66] J. Wang, Y. Wang, J. Shi, and Y. Su, "Effect of External Magnetic Field on the Microstructure of 316L Stainless Steel Fabricated by Directed Energy Deposition," *ASME International Mechanical Engineering Congress and Exposition, Proceedings (IMECE)*, vol. 2B-2019, Jan. 2020, doi: 10.1115/IMECE2019-12122.

[67] D. Du *et al.*, "Influence of Static Magnetic Field on the Microstructure of Nickel-Based Superalloy by Laser-Directed Energy Deposition," *Metall. Mater. Trans. A Phys. Metall. Mater. Sci.*, vol. 51, no. 7, pp. 3354–3359, Jul. 2020, doi: 10.1007/S11661-020-05783-4/FIGURES/4.

[68] P. Y. Wu, M. Hirtler, M. Bambach, and H. Yamaguchi, "Effects of build- and scan-directions on magnetic field-assisted finishing of 316L stainless steel disks produced with selective laser melting," *CIRP J. Manuf. Sci. Technol.*, vol. 31, pp. 583–594, Nov. 2020, doi: 10.1016/J.CIRPJ.2020.08.010.

[69] W. Zhao, Y. Wei, X. Zhang, J. Chen, and W. Ou, "Comparative investigation of wire arc additive manufacturing of Al-5%Mg alloy with and without external alternating magnetic field," *The International Journal of Advanced Manufacturing Technology 2021 119:3*, vol. 119, no. 3, pp. 2571–2587, Jan. 2022, doi: 10.1007/S00170-021-08466-5.

[70] M. Y. Khan, P. S. Rao, and B. S. Pabla, "An experimental study on magnetic field-assisted-EDM process for Inconel-625," *Advances in Materials and Processing*

Technologies, vol. 8, no. sup4, pp. 2204–2230, Nov. 2022, doi: 10.1080/2374068X.2022.2036450.

[71] G. Li, Z. Wang, L. Yao, D. Xie, and G. Chen, "Concentration mixing and melt pool solidification behavior during the magnetic field assisted laser cladding of Fe-Cr-based alloy on 45 steel surface," *Surf. Coat. Technol.*, vol. 445, p. 128732, Sep. 2022, doi: 10.1016/J.SURFCOAT.2022.128732.

[72] L. J. Xu, Y. Y. Chen, Z. G. Liu, and F. T. Kong, "The microstructure and properties of Ti–Mo–Nb alloys for biomedical application," *J. Alloys Compd.*, vol. 453, no. 1–2, pp. 320–324, Apr. 2008, doi: 10.1016/J.JALLCOM.2006.11.144.

[73] A. N. Laskovski, "Biomedical Engineering, Trends in Materials Science," *Biomedical Engineering, Trends in Materials Science*, Jan. 2011, doi: 10.5772/992.

[74] S. Kurtz, K. Ong, E. Lau, F. Mowat, and M. Halpern, "Projections of primary and revision hip and knee arthroplasty in the United States from 2005 to 2030," *Journal of Bone and Joint Surgery*, vol. 89, no. 4, pp. 780–785, 2007, doi: 10.2106/JBJS.F.00222.

[75] M. Tanaka *et al.*, "Bone bonding ability of a chemically and thermally treated low elastic modulus Ti alloy: gum metal," *Journal of Materials Science: Materials in Medicine 2013 25:3*, vol. 25, no. 3, pp. 635–643, Nov. 2013, doi: 10.1007/S10856-013-5101-4.

[76] M. Niinomi, "Mechanical biocompatibilities of titanium alloys for biomedical applications," *J. Mech. Behav. Biomed. Mater.*, vol. 1, no. 1, pp. 30–42, Jan. 2008, doi: 10.1016/J.JMBBM.2007.07.001.

[77] M. Niinomi, "Recent research and development in titanium alloys for biomedical applications and healthcare goods," *Sci. Technol. Adv. Mater.*, vol. 4, no. 5, pp. 445–454, Sep. 2003, doi: 10.1016/J.STAM.2003.09.002.

[78] H. M. Silva, S. G. Schneider, and C. M. Neto, "Study of nontoxic aluminum and vanadium-free titanium alloys for biomedical applications," *Materials Science and Engineering C*, vol. 24, no. 5, pp. 679–682, Nov. 2004, doi: 10.1016/J.MSEC.2004.08.051.

[79] J. M. Chaves, O. Florêncio, P. S. Silva, P. W. B. Marques, and C. R. M. Afonso, "Influence of phase transformations on dynamical elastic modulus and anelasticity of beta Ti-Nb-Fe alloys for biomedical applications," *J. Mech. Behav. Biomed. Mater.*, vol. 46, pp. 184–196, Jun. 2015, doi: 10.1016/j.jmbbm.2015.02.030.

[80] K. Miura, N. Yamada, S. Hanada, T. K. Jung, and E. Itoi, “The bone tissue compatibility of a new Ti-Nb-Sn alloy with a low Young’s modulus,” *Acta Biomater.*, vol. 7, no. 5, pp. 2320–2326, 2011, doi: 10.1016/J.ACTBIO.2011.02.008.

[81] X. Zhao, M. Niinomi, M. Nakai, and J. Hieda, “Beta type Ti–Mo alloys with changeable Young’s modulus for spinal fixation applications,” *Acta Biomater.*, vol. 8, no. 5, pp. 1990–1997, May 2012, doi: 10.1016/J.ACTBIO.2012.02.004.

[82] E. Eisenbarth, D. Velten, M. Müller, R. Thull, and J. Breme, “Biocompatibility of β-stabilizing elements of titanium alloys,” *Biomaterials*, vol. 25, no. 26, pp. 5705–5713, Nov. 2004, doi: 10.1016/J.BIOMATERIALS.2004.01.021.

[83] P. S. Nnamchi, C. S. Obayi, I. Todd, and M. W. Rainforth, “Mechanical and electrochemical characterisation of new Ti–Mo–Nb–Zr alloys for biomedical applications,” *J. Mech. Behav. Biomed. Mater.*, vol. 60, pp. 68–77, Jul. 2016, doi: 10.1016/J.JMBBM.2015.12.023.

[84] M. Wang and T. Tang, “Surface treatment strategies to combat implant-related infection from the beginning,” *J. Orthop. Translat.*, vol. 17, pp. 42–54, Apr. 2019, doi: 10.1016/J.JOT.2018.09.001.

[85] R. O. Darouiche, “Treatment of Infections Associated with Surgical Implants,” *New England Journal of Medicine*, vol. 350, no. 14, pp. 1422–1429, Apr. 2004, doi: 10.1056/NEJMRA035415;PAGEGROUP:STRING:PUBLICATION.

[86] W. Xu *et al.*, “Characteristics of novel Ti–10Mo-xCu alloy by powder metallurgy for potential biomedical implant applications,” *Bioact. Mater.*, vol. 5, no. 3, pp. 659–666, Sep. 2020, doi: 10.1016/J.BIOACTMAT.2020.04.012.

[87] P. Anguita-Alonso, A. D. Hanssen, D. R. Osmon, A. Trampuz, J. M. Steckelberg, and R. Patel, “High rate of aminoglycoside resistance among staphylococci causing prosthetic joint infection,” *Clin. Orthop. Relat. Res.*, vol. 439, pp. 43–47, 2005, doi: 10.1097/01.BLO.0000182394.39601.9D.

[88] E. M. Hetrick and M. H. Schoenfisch, “Reducing implant-related infections: active release strategies,” *Chem. Soc. Rev.*, vol. 35, no. 9, pp. 780–789, Aug. 2006, doi: 10.1039/B515219B.

[89] I. F. Scheiber, J. F. B. Mercer, and R. Dringen, “Metabolism and functions of copper in brain,” *Prog. Neurobiol.*, vol. 116, pp. 33–57, May 2014, doi: 10.1016/J.PNEUROBIO.2014.01.002.

[90] Y. He, Y. Zhang, Y. Jiang, and R. Zhou, “Fabrication and characterization of superelastic Ti–Nb alloy enhanced with antimicrobial Cu via spark plasma sintering for biomedical applications,” *J. Mater. Res.*, vol. 32, no. 13, pp. 2510–2520, Jul. 2017, doi: 10.1557/JMR.2017.191.

[91] E. Zhang, X. Wang, M. Chen, and B. Hou, “Effect of the existing form of Cu element on the mechanical properties, bio-corrosion and antibacterial properties of Ti-Cu alloys for biomedical application,” *Materials Science and Engineering C*, vol. 69, pp. 1210–1221, Dec. 2016, doi: 10.1016/j.msec.2016.08.033.

[92] A. T. Akono and F. J. Ulm, “An improved technique for characterizing the fracture toughness via scratch test experiments,” *Wear*, vol. 313, no. 1–2, pp. 117–124, May 2014, doi: 10.1016/J.WEAR.2014.02.015.